Vascular Modelling in Non-traumatic Spinal Cord Injury

Elizabeth Dutson Young

Submitted in accordance with the requirements for the degree of

PhD in Medical and Biological Engineering

The University of Leeds

Institute of Medical and Biological Engineering

School of Mechanical Engineering

May, 2023

The candidate confirms that the work submitted is his/her own and that appropriate credit has been given where reference has been made to the work of others.

Acknowledgements

First and foremost, thanks go to my primary supervisor Richard Hall who has been inexpressibly patient and supportive but always able to push/pull when required. Thanks also goes to Mark Wilson who has been beyond helpful in breaking down concepts and assisting in the details that are so easily overlooked.

The faculty members and experiences attributed to the CDT, iMBE and its extensions have been so appreciated and worthwhile.

There are so many people who have been a part of this journey outside the academic practice. From Leeds, all the CDT cohort that have been endless cheerleaders for each other during and afterward, of which some have now become truly treasured, lifelong friends. Shout outs must be given to my old housemates during this process, namely 21SMC, 29ET and Poplars. I'd like to thank the LUUHC who took me up high when things very much felt low.

I am ever and always thankful for my support network in Scotland, mostly my wonderful family whose mantra of "what's for ye won't go by ye" rings truer every day. To my core friendship network from Hamilton, UoG and beyond - you are my rock(s).

Lastly, to thank Dan, who has been my eternal soundboard and joy.

Abstract

Non-traumatic spinal cord injuries (NT-SCI) represent a number of pathologies which vary in progression and symptom presentation. Chronic mechanical compression is known to alter cord biomechanics and disrupt cord blood supply. Understanding of the mechanics that trigger ischemia and therefore the cascade of hypoxia and neurological dysfunction remains unknown. This thesis investigates the changes in blood and oxygen supply to the thoracic spinal cord under mild non-traumatic compression.

The effects of injury severity, location and profile on the white and grey matter and its vasculature are explored. A fluid-structure interaction model is developed to represent the effect of compression on spinal tissue and its arteries. In order to model microvascular flow, a porous-continuum model is coupled to the arteries to distribute blood though the tissue. Oxygen transport and its consumption was coupled to the blood flow models. Compressions are considered at increasing intervals of 2.5% strain up to 10% strain, with all deformations repeated at anterior, posterior and anteroposterior locations with focal and diffused injury profiles.

Results show that focal injuries do not elicit significant changes to vascular response under mild injury. However, larger diffused injuries are effectual. Anterior injury is shown to cause a decrease in blood flow from 2.5% strain and decrease in oxygen consumption at strains of 7.5%, across both matter types. Anteroposterior injury is found to produce a compensatory response in white matter with adverse effect in grey matter seen at 10% strain. Posterior

injury had detrimental effect on white matter, followed by grey matter response at 7.5% strain.

The work indicates that disruption of the vascular network in NT-SCI takes place at strains well below reported symptomatic thresholds. Patients presenting with diffused anterior injuries are at the highest risk. Further elaboration of vascular response in sub-clinical strains could bring greater understanding to clinical intervention thresholds.

Table of Contents

List of Tables

List of Figures

List of Abbreviations

ALE: arbitrary Lagrangian-Eulerian method
ASA: anterior spinal artery

CSM: cervical spondylitic myelopathy

CNS: central nervous system

CSF: cerebrospinal fluid
FEA: finite element analysis

GM: grey matter

MSCC: malignant spinal cord compression
NT-SCI: non-traumatic spinal cord injury

PDE: partial differential equation

PSA: posterior spinal artery

PSV: posterior spinal vein

SCBF: spinal cord blood flow
SCI: spinal cord injury

WM: white matter

3-D: three-dimensional

Chapter 1

Introduction and literature review

Non-traumatic spinal cord injury (NT-SCI) is known to have a variety of presentations and is understood as influenced by a combination of factors, namely mechanical forces, patient vulnerability, vascular behaviour and timescale [1]. A recent meta-analysis reported that NT-SCI manifests asymptomatically in approximately 20% of patients and 80% of patients do experience progressive myelopathy, paresis and malfunction of the innervated viscera at and below the injured level [2]. There are 18,000 new cases of NT-SCI per year (as of 2022) and this is expected to continually increase due to aging global populations [3]. The progressive nature of NT-SCI is primarily influenced by varying development rates and complexities of underlying aetiologies [4]–[7]. Therefore, understanding the pathophysiology of non-traumatic cord compression will be crucial in aiding better diagnosis and treatment frameworks for patients.

Positive patient prognosis decreases with increased duration of injury but asymptomatic manifestation makes diagnosis difficult and is worsened by NT-SCI being commonly overlooked as a secondary symptom of co-morbidities [8]. The high mortality rates associated with NT-SCI correlate to high incidence but low prevalence; many people diagnosed with cord compression have shortened life expectancy, mainly attributed to co-presentation alongside severe aetiologies (e.g. cancer and cardiovascular diseases) or injury at an elderly age [9]. Low prevalence coupled to a lack of pathological

characterisation causes a gap in clinical understanding, which has knock-on effects in the clinic and on patient quality of life. Despite the estimation that ~70% of spinal cord injuries are suspected to be non-traumatic [10], patients are usually reported as sub-sections of traumatic injury rehabilitation units, or are not admitted to specialist units at all [11].

Patient prognosis and functional outcome weakly correlates with strain experienced by the cord, therefore severity of compression is not sufficient as a sole diagnostic measure [1]. It is understood that NT-SCI becomes symptomatic at a presumed >29% reduction in spinal canal diameter as axonal disruption has been reported at this strain [12]. It is understood that vascular response to NT-SCI is an essential process in injury development as chronic mechanical compression of the spinal cord causes disruption of cord microvasculature and the blood-spinal cord barrier. This is believed to trigger ischemia which exacerbates the pathophysiological process [13]. Ischemia is defined as a reduction in blood supply to a part of the body. As a result, an inadequate supply of oxygen is delivered to the tissue, which is known as hypoxia [14]. It is currently assumed that microvascular changes to the spinal cord, which result in ischemia, take place at the later stages of injury development and it is known that the degree of ischemia is proportional to the degree of neurological dysfunction [15], [16]. In investigating the pathophysiology of progressive compression, the mechanics should be considered for both neural and vascular components of the spinal cord. Disruption to perfusion has been reported in both clinical and post-mortem models and has been hypothesised as driven by occlusion of the sulcal arteries and transversely-coursing arterioles of the grey matter in anterior

injury [17]. Occlusion of the intramedullary grey matter branches has been hypothesised as causative of NT-SCI in posterior injury scenarios [17]. With that, the location of injury is an essential factor to consider in understanding what effects occlusion of different underlying vasculature may have. A recent 2019 study found that a decrease in spinal cord diameter in cervical spondylitic myelopathy (CSM) patients strongly correlated with decreased spinal cord blood volume, but the pathophysiology underlying these phenomena remained misunderstood. Hypoxia of the spinal cord was not statistically correlated to severity of cord compression, unlike cord ischemia, but the degree of oxygen extraction rate was significantly correlated – assumed as driven by compensatory mechanisms to prevent hypoxia in the absence of perfusion [18]. Only one computational study has been done that couples the spinal-vasculature behaviour as current experimental methodologies remain limited, but microvasculature was excluded from the model [19]. Quantification of vascular changes to spinal microvascular networks experiencing NT-SCI should therefore be investigated to better understand the response of tissue in scenarios of compression and ischemia.

Various studies have employed balloon occlusion studies to determine what indentation profiles are effectual on the spinal cord and its vasculature [4], [12], [20]–[22]. One study found that balloon size had a stronger correlation to functional outcome than injury timescale [12]. Previous finite element models have highlighted the relationship between injury profile, rate of injury and mechanical stress. Namely, focal and lateral injuries reach maximum compression faster but diffused injury ultimately reaches von Mises stresses 50% higher than other injury types [23]. Therefore, in order to understand early

injury progression at sub-clinical strains, injury profiles representative of different aetiologies should be considered alongside location when investigating the mechanical thresholds that drive vascular disruption in NT-SCI.

This thesis investigates the vascular response of spinal tissue under chronic compression by developing a computational model that addresses the effects of compression severity, location and profile. This chapter reviews the current knowledge base around NT-SCI in the literature, discusses the motivations for the research and outlines the structure of the remainder of the thesis.

1.1 Aetiology

The most prevalent NT-SCI aetiologies in developed countries are metastatic cancerous compressions and degenerative conditions such as cervical spondylitic myelopathy [8]. The spinal cord anatomy is split into the cervical (top section of the spine in the neck), thoracic (upper and middle part of the back), lumbar (lower back) and sacral (bottom section above the coccyx) regions. Different aetiologies are known to affect different regions of the spine. Degenerative conditions, such as CSM, commonly manifest alongside arthritis and ankylosing spondylitis in elderly, Western-based populations [11]. Of the global elderly population (above 60 years old), 87% has been estimated to present at least one severely degenerated cervical level [24]. Low cervical and low lumbar injuries generally arise from common degenerative conditions, whereas thoracic spinal injury most commonly derives from neoplastic, vascular or infectious conditions [8]. Aetiologies of NT-SCI can have onset

periods of minutes (e.g. cord infarction), hours (e.g. transverse myelitis), days (e.g. spinal abscess) or weeks to months (e.g. spinal canal stenosis) [8]. The global incidence rates of the aetiologies resultant in NT-SCI are summarised below (Table 1).

Table 1: Summary of non-traumatic spinal cord injury aetiologies [8]**.** Data was collated based on global epidemiology reports, spanning across various developed and developing countries. For this reason, incidence derivations are likely reflective of economic state. Western European data is composed of preliminary survey studies from the 1990s and primarily focusses on spinal tumours and not metastasis.

Aetiology	**Clinical manifestations**	**Incidence (%)**
Neoplastic cancer	Malignant spinal cord compression	25
Vascular	Haematomas, arterial spinal artery syndrome, arteriovenous malformations	14
Infections	Spinal abscesses, tuberculosis, Pott's lung, granuloma, HIV	21
Autoimmune/ congenital disease	Transverse myelitis, multiple sclerosis, amyotrophic lateral sclerosis, Guillan-Barre syndrome, spinabifida	18
Degenerative conditions	Spinal stenosis, prolapsed disc, cervical spondylitic myelopathy, osteoporosis, arthritis, ligament ossification, bone fractures	22

Generally, symptom progression begins as radicular pain down the nerve root, hindering lower limb movement *via* depression of tendon reflexes and sensory myelopathy at the toes. Continued compression surpasses local and radicular effects to cause wider spread neurological dysfunction, affecting gait and coordination which can ultimately result in paralysis [25]. Injury at higher spinal segments is associated with myelopathy, hyperreflexia, hypertonia of the arms

and loss of fine motor function in the hands. At the later stages of NT-SCI where paresis symptoms are visible, 60% of patients suffer from autonomic and sensory dysfunction. Evidence of Horner's syndrome – bladder and bowel incontinence – is indicative of severe injury and a worse prognosis [25]. The current standardised treatment for NT-SCI is decompression [3].

Variations in pathology manifestation can be attributed to variations in mechanical stresses, timescale and patient vulnerability [1]. The profile of compression inherently controls the mechanical stresses experienced by the underlying spinal tissue and vasculature that is being compressed, therefore the profile of injury is an important consideration in understanding the stress mechanics of different aetiologies [26]. NT-SCI aetiologies and their respective injury profiles are as below (Table 2).

Table 2: Spinal cord injury profiles and the respective aetiologies [23].

.**Location of compression**	**Examples of injury pathology**
Diffuse (spanning across multiple spinal segments)	Herniated disc, metastatic compression or osteophyte development on the edge of the vertebral body
Focal (localised at the injury site)	Local osteophyte development
Lateral	One-sided and asymmetric metastasis
Circumferential	Combines diffuse with additional compression on the opposite side of cord, usually caused by hypertrophy or ossification of ligamentum flavum

It is already known that profile is effectual on prognosis (e.g. small, sharp dislocation fragment compared to a large, blunt disc bulge) and that injuries diffused across multiple segments have shown worse functional outcomes

than that of focal, single segment injuries [23]. This, coupled to the location of injury is assumed as essential in understanding NT-SCI development, due to the complexity and difference of underlying vascular anatomy relative to different regions and tissues in the spinal cord. Therefore, with regards to inclusion criteria for the model, the contributing vessels and anatomy of the spinal cord were important to consider (section 1.2).

1.2 Anatomy

1.2.1 Spinal cord and its matter types

The spinal cord nervous tissue comprises of white and grey matter, which enables the sensory and motor function of the body (Figure 1). The cord exits from the foramen magnum below the brainstem into the vertebral foramen, travelling down to the conus medullaris at the second lumbar vertebrae, where it meets the fibrous filum terminale anchored to the coccyx. In humans, the spinal cord is approximately 45cm in length [27] and 1.5cm in diameter [28] and the adult rat spinal cord is approximately 12cm long and 3mm in diameter [29]. In investigating spinal cord pathology, rat models are commonly used as rats are understood to develop symptoms similar to those seen in humans. Relative to the parameters available in the literature for analysis of early development of NT-SCI, the rat model is the focus of the thesis as an initial step toward better understanding the human pathology. In humans, dorsal sensory and ventral motor nerve roots bi-laterally emerge from segments through the intervertebral foramen to form the 31 pairs of spinal nerves which innervate the body *via* dermatomes [30]. Visceral organs are innervated by

axons from the lateral grey horn, functioning *via* sympathetic ganglia. Sympathetic ganglia in upper and middle thoracic segments control the head and thorax, whereas lower and upper lumbar segments control the abdominal and pelvic organs.

Dorsal roots behave as afferent bundles of axons to relay sensory information to the central nervous system (CNS) before terminating in the cell body dense dorsal root ganglia. Ventral roots behave as efferent axons that arise from motor neuron cell bodies in the anterior horn to innervate locomotion [30]. The cord stems from the medulla at the atlas and axis (C1 and C2) and connects 5 further cervical segments. The cervical enlargement is based at C5-T1, where neural innervation of the arms is controlled. Next, 12 thoracic segments control the trunk and 5 lumbar and 5 sacral segments form the lumbar enlargement (L1-S3) to control lower limb function [30].

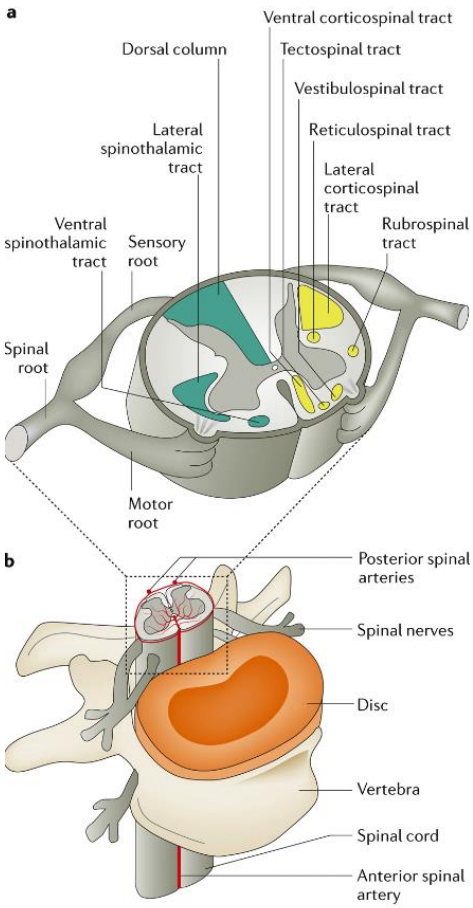

Figure 1: Neural and structural components of the spinal cord anatomy, Ahuja *et al*., 2017 [31]**.** *(Reproduced with permission from* Springer Nature).

White matter contains connective, myelinated nerve axons that conduct nerve impulses in ascending and descending tracts, transmitting sensory and motor information, respectively. Grey matter resides in the inner section of the cord, where the grey commissure encompasses the central spinal canal containing cerebrospinal fluid [30]. The grey matter is the butterfly shaped anatomy which is split into the dorsal, intermediate, lateral and ventral horn columns that consist of glia, cell bodies, dendrites and unmyelinated axons of motor and inter-neurons [30]. Higher spinal levels have a greater grey matter volume, due to greater numbers of ascending and descending neural tracts to connect

and innervate finer motor dexterity. Hence, injury to higher spinal levels has a more pronounced effect on motor function for patients, due to the downstream effect on all innervations beneath the injury level [30].

The spinal cord has 3 layers of protective meninges: the outer dura, arachnoid and inner pia. These protect the white matter, which is situated circumferentially around the grey matter. Beneath the vertebrae and above the dura mater lies the epidural space, where the spinal lymphatic system, nerve roots, connective and fatty tissues reside. Beneath the arachnoid and pia mater is the sub-arachnoid space, where cerebrospinal fluid (CSF)maintains pressure, stability and nutrient diffusion in the cord, governed by the cord central canal. Cerebrospinal fluid flows from the sub-arachnoid space through perivascular cell junctions into the fluid-containing central canal for pressure maintenance and transport of nutrients to the CNS [32].

1.2.2 Spinal vasculature anatomy

The arterial vasculature of the spine derives from anterior (ventral), posterolateral and posterior (dorsal) systems that span the length of the cord. Cervical to upper thoracic (T3) regions are supplied by the anterior segmental medullary arteries and ascending cervical artery. T3-T7 are supplied by posterior intercostal arteries (Figure 2) and T8-conus are supplied by the artery of Adamkiewicz and cone artery [33].

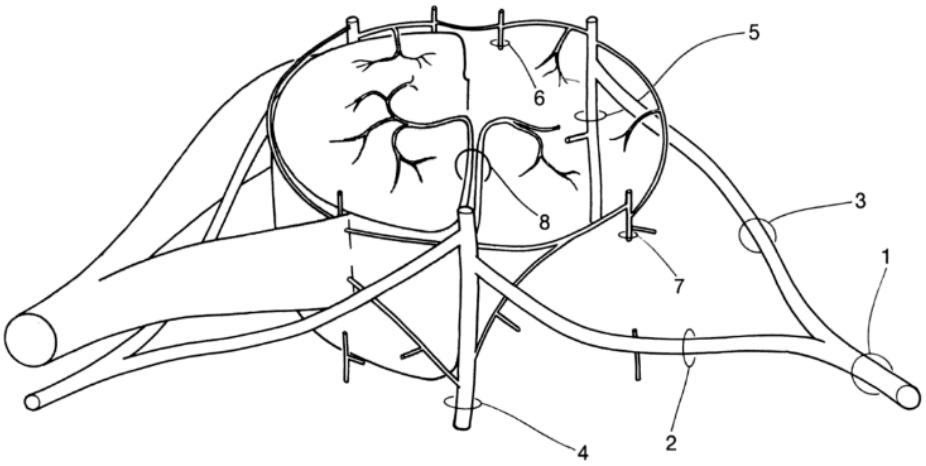

1 nervomedullar artery, *2* anterior radicular artery, *3* posterior radicular artery, *4* anterior spinal artery, *5* posterolateral spinal artery, *6* posterior spinal artery, *7* transverse and longitudinal interconnections between the main longitudinal trunks (pial network) giving origin to the perforating branches of the vasocorona, *8* sulcal (central) arteries

Figure 2: Arterial organisation at the thoracic segmental level. Adapted from Thron, 1988 [34]**.** (*Reproduced with permission from* Springer Nature*).*

The anterior spinal artery (ASA) arises from two vertebral arteries, anastomosing at the foramen magnum at the medulla oblongata. The ASA lies within the anterior fissure, protected underneath the pia mater. It is reported to provide up to two-thirds of blood flow to the thoracic region of the cord, namely the grey matter and funiculi, so is almost solely responsible for the supply of this region due to a dearth of other collateral arteries. Therefore, compression of thoracic anterior arteries makes the cord more susceptible to damage when compared to regions of the cord [35]. The posterior spinal arteries (PSA)derive from two vertebral arteries and run down the posterolateral region to provide for the posterior grey column and posterior funiculus. These three key arteries (ASA and two PSAs) are connected by a lateral anastomoses network, known as the vasocorona. The vasocorona circumferentially travels through the pia mater to enter and supply the lateral columns *via* transversely-coursing arterioles [33].

The radicular-associated feeder arteries span all segmental levels and the surface of the spinal cord *via* vascular branches of varying size and location. The predominant segmental artery is the artery of Adamkiewicz, which arises from the radiculomedullary branch at T9-12 of the posterior intercostal artery to anastomose with the ASA and provide blood supply for the lower segments [33]. The central sulcal arteries and peripheral radial arteries constitute the intrinsic spinal supply; they have various entry points into the spinal cord and join with others to form a network which supplies the anterior-residing grey matter and inner half of the white columns [36]. Average microvessel density in thoracic ventral grey matter is 571mm^{-2} and in dorsal grey matter is 484mm^{-2} ; white matter has markedly lower microvessel densities at 90mm^{-2} in ventral white matter and 88mm^{-2} in dorsal white matter [37]. The ASA resides on the midline below the pia, where it joins the posterior artery to create an arterial arch with many sulcal and lateral artery offshoots [33]. Peripheral radial arteries derived from the posterior spinal arteries and pial plexus supply the posterior-residing grey matter and outer half of the white column [36]. The pial network acts as an extrinsic arterial supply which receives blood from the middle radiculomedullary and radiculopial branches [33].

The spinal cord venous system generally aligns with the anatomy of the arterial system, but veins have a more tortuous design unlike the straight, longitudinal anatomy of the arteries (Figure 3). The core venous structure in the thoracic cord is the posterior spinal vein (PSV) [33].

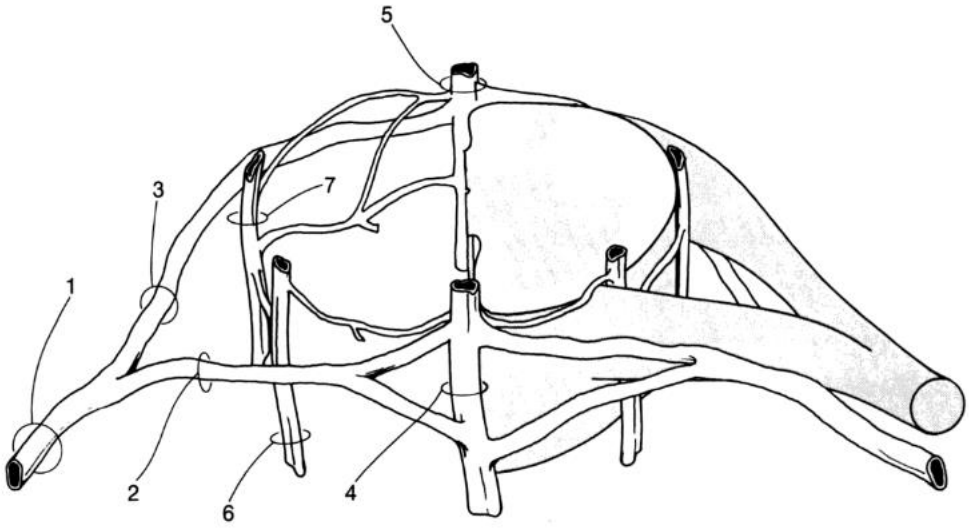

1 radicular vein, *2* anterior radicular vein, *3* posterior radicular vein, *4* anterior median vein, *5* posterior median vein, *6, 7* additional discontinuous longitudinal systems in antero- or posterolateral position

Figure 3: Venous organisation at the thoracic segmental level. Adapted from Thron (1988) [34]**.** (*Reproduced with permission from* Springer Nature*).*

The intrinsic system includes radial veins which span the whole cord and connect to a pial surface network. The anterior and posterior sulcal veins drain into the great radicular vein and anterior and posterior spinal veins, which reside sub-pially at the midline of the ventral and dorsal sections, respectively. The extrinsic system consists of these spinal veins and the aforementioned pial venous plexus, which resides on the surface of the spinal cord as a longitudinally and axially anastomosed arranged network [33]. Extrinsic veins feed into radiculomedullary veins, but not *via* nerve roots as seen in the arteries. The radicular-associated veins join the epidural veins, where the internal plexus communicates with the external plexus. The external plexus joins the innominate, azygos or ascending lumbar veins at cervical, thoracic and lumbar levels, respectively [33].

Understanding the stringency of the anatomy is linked to the differences in outcome based on injury location (anterior, posterior, anteroposterior); there are few collateral vessels for compensatory re-routing of blood flow under thoracic injury, so equilibrium of the system is tightly regulated [35].

The ability of blood to regulate communicative molecules, nutrients and gases is crucial for optimal function of neurons: neuronal function and vessel diameter are coupled to regulate the metabolic availability of nutrients and oxygen [38]. The size and location of vasculature being occluded affects the overall neural deficit [19], [39], [40] as blood vessel density is relative to the metabolic needs of the tissue. Neuron-dense grey matter has four to five times more capillaries than the connective white matter as the balance of energy, solutes and gases required for optimal synaptic transmission and plasticity of its neural tracts is more demanding [33]. Capillary distribution is presumed to emulate grey matter neural fibre organisation, by co-locating beside nerve cell clusters and presenting as a homogenous spread throughout the ventral and dorsal horns. The white matter predominantly consists of transversely-coursing arterioles and has a less dense microvascular network [33]. These aspects are assumed to contribute to the variations of NT-SCI pathophysiology.

1.3 NT-SCI pathology

Non-traumatic injury is most often defined as an incomplete lesion of the spinal cord and is most commonly associated with paraplegia. In common indications

such as cervical spondylitic myelopathy, the threshold at which myelopathy is defined is at a 30% reduction of the spinal canal diameter, based on MRI measurements from patients [23]. NT-SCI compressions are known to have effect on the vasculature, primarily affecting larger feeder vessels which transmit affect through to the microvascular-dense tissue [35], [42–44]. A reduction in blood flow decreases the number of microvessels, which cyclically results in progressive neuronal atrophy and reduced fibre tract density [44]. This has been deemed as the point of irreversible damage - one study notes this outcome after 9 weeks of compression [45].

In NT-SCI, a decrease in cord anterior-posterior diameter and worsened functional outcome linearly correlate to tissue ischemia and an increased consumption of oxygen [18]. It is expected that, similar to the brain injury response, when perfusion pressure falls below a critical level, compensatory excess consumption of oxygen takes place which creates a hypoxic environment. The low perfusion gradients disallow convective bulk transport, therefore oxygen transport is limited to diffusion, which is an insufficient oxygen transport source for vascular-dense tissue like the spinal cord [46]. In humans, oxygen within the spinal cord is at the same level as the brain (35-39mmHg), but its oxygen is derived from 40-60% less blood flow due to a lower vascular density [47]. A decrease in microvasculature, or narrowing of vessels, becomes problematic when intravascular distances surpass the maximum diffusion threshold, or skew pressure gradients to create watershed areas of opposing flows, exaggerating diffusion gradients and competition amongst vessels for oxygen uptake [48].

Hypoxia is defined as the level of oxygen at which tissue homeostasis can no longer take place, caused by either not enough oxygen in the blood or by a reduction in blood flow to the tissue [35]. Therefore, there is no set concentration threshold at which hypoxia takes place as it is anatomy dependent and is known as the state between normoxia (normal physiological levels) and anoxia (complete lack of oxygen). General clinical guidance infers that a 15-20% decrease in patient arterial oxygen partial pressure (95-100mmHg to below 80mmHg) is considered abnormal [49]. It is understood that hypoxia alone is not significantly detrimental to tissue functionality when it is accompanied by network re-routing from collateral vessels, but hypoxia is detrimental when caused by ischemia and a reduction to blood flow. This is believed to be a core pathophysiological aspect of thoracic spinal cord injury due to its watershed anatomy, wherein few opposing vessels are the sole suppliers to the region [35].

1.3.1 Vascular pathology

In aiming to better understand the pathophysiology of NT-SCI, vascular response must be studied. Clinicopathological studies state that mild anteroposterior compression affects the white matter through vascular occlusion of the vasocorona-derived arterioles, meanwhile severe compression (>40%) diffuses stress through to the grey matter which affects the deeper vessels and microvascular networks [50]. Due to this, white matter is destroyed first as the connector of the vascular-dense grey matter network. Then, the dorsal horns degrade, which follows clinical symptom progression

of sensory dysfunction manifestation before ventral horn degradation and motor dysfunction manifestation [25], [51]. Other post-mortem studies have indicated that anterior occlusion of the transverse, penetrating sulcal vessels is known to significantly affect neural outcomes due to a reduction in vessel density in the grey matter ventral horns and corticospinal tracts [36]. Posterior compression occludes the transversely-coursing arterioles which disrupts the adjacent lateral columns. However, the posterior spinal arteries have a crossing pattern, which make them more resistant to occlusion under local stresses [33].

Ischemia is a known contributor to NT-SCI; chronic mechanical stresses decrease blood vessel capacity and therefore decrease perfusion rates [42]. The luminal diameter of blood vessels decrease when under compression from external forces; this change in vasculature results in remodelling, such as thickening and hyalinisation of the vessel walls, alongside stretching, flattening and loss of smaller branch vessels which increases tortuosity and length of the fluid path [52]–[54]. Blood vessel walls, namely the endothelial layer, exist under constant levels of shear stress due to fluid flow. In normal physiology, endothelial cells are elongated and align in the direction of flow, producing factors for modulation of smooth muscle layer vascular tone [55]. Chronic compression is believed to cause misalignment and degradation of endothelial cells. The cytoskeleton usually forms stress fibres in the direction of laminar shear stress, but under conditions of low shear stress, endothelial cell adhesion decreases, which is assumed to cause vessel regression and apoptosis of the microvasculature which disrupts the blood-spinal cord barrier [56]. This apoptotic process cyclically drives inflammatory molecules to the

injury zone, which has been linked to localised ischemia and hypoxia. Studies have evidenced that disruption of the blood-spinal cord barriers' endothelial cell architecture is linked to decreased presence of tight junction proteins and increased tissue permeability to imaging markers and inflammatory molecules [57].

These phenomena would likely be emulated in NT-SCI as increased permeability, localised tissue swelling and therefore increased pressure gradients have been reported [58]. It is hypothesised these responses would aim to create faster velocities and compensatory transport of oxygen and nutrients. These processes are exacerbated by the rise in inflammatory factors, resulting in increased vascular permeability for leukocyte infiltration into the parenchyma [36] - the decrease of pericyte populations distresses neurons, who signal to instigate vessel constriction and cell death [59]. These signals create a cyclic feedback loop wherein the local region is in constant inflammatory distress. As compression continues, myelin is destroyed alongside grey matter neurons and white matter oligodendrocytes. An imbalance of carbon dioxide and oxygen partial gas pressures exacerbate the local region into a state of hypoxia, which is known to be preceded by an increase in compensatory oxygen extraction from surrounding spinal tissues [18]. This change in vascular tone correlates with a loss in vessel wall stringency and architecture, vessel autoregulation and systemic hypotension.

Recent studies support this theory in stating that pericyte populations swell and surround the damaged area, with increased presence of vacuolae and cavuolae, attributing to the influx of inflammatory molecules. An increase in

permeability increases diffusive potential, enabling enhanced influx of interstitial molecules - calcium, potassium and sodium – all regulators of synapse activity [60]. The imbalance of the synaptic microenvironment leads to recruitment of damaging inflammatory neurotransmitters and excitotoxic proteins, increasing cell death rates. Venous hypertension fuels white matter oedema and vacuolisation to decrease surrounding blood flow, with almost complete ceasing of circulation in deep white matter [61]. Late-stage oedema links to increased arteriole pressure and leakage into grey and white matter, damaging the mitochondria and decreasing cell energy supply. Similar phenomena have been reported in syringomyelia, where increased CSF pressure is indicative of injury severity through secondary injury response of cytoskeletal disruption, increased permeability and capillary leakage which recruits inflammatory and apoptotic factors. The intricacies of the vascular-CSF coupling are likely an essential part of the NT-SCI pathway as CSF is responsible for clearance of metabolic waste from perivascular spaces [62], [63], but for the purpose of focusing on vascular behaviour, it was neglected from this work.

1.3.2 Neural pathology

Compression from bony fragments, disc herniations and neoplasms predominantly arise in the anterior region of the cord, disrupting the corticospinal tracts to cause myelopathy, paresis and gait deficits [30]. Higher degrees of compression increase through to deeper tissues, such as the

lateral grey horns, which further disrupts motor and autonomic organ function – this is linked to lower survival rates [64].

Symptomatic progression is associated with anterior horn atrophy of the grey matter and degeneration of ascending and descending white matter pyramidal tracts [42]. On a macrostructural level, however, compression appears to flatten and force neural fibres together to reduce the extracellular space, decrease fractional anisotropy and to increase diffusivity potential with particular effect in the dorsal and lateral columns. This decreased fractional anisotropy in humans correlated with a decrease in clinical, functional output scores [51]. Cell populations in the anterior horn have been reported to decrease when the cross-sectional area of the cord decreases by 30%; the decrease in cell population plateaus above 50% compression [65].

Post-mortem studies have identified that demyelination and axonal loss usually begin in the lateral corticospinal tracts, which when coupled to expression of neurofilament and damage response proteins, results symptomatically as spastic gait. Continued compression leads to degeneration of the dorsal column and central grey matter: at the early stages of NT-SCI, sensory defects precede lower motor dysfunction [66]. Initial loss of the sensory dorsal horn correlates with a loss in microvasculature under chronic compression; the ventral horn controls motor function so is assumed to be preserved [67]. Loss of protective myelin is attributed to oligodendrocyte pathology and axon degradation, however, myelin can be well preserved until severe stages of compression [42].

Identifying the thresholds and pathophysiology of NT-SCI has been difficult to achieve in the clinic, as the main diagnostic methodology aside from functional testing examines the extent of compression by MRI visualisation, which does not account for other factors such as vascular behaviour. NT-SCI is difficult to model elsewhere but pathophysiological investigations have been undertaken *in vivo*.

1.4 *In vivo* studies

Pre-clinical studies rely heavily on *in vivo* animal models for realistic research and intervention development, but their expense and difficult reproducibility is limiting. Analysis of vascular pathological changes at the micro-scale is extremely hard to do both *in vivo* and clinically. This is due to difficulty in maintaining tissue integrity after instrumental intrusion or manipulation *ex vivo*, coupled to difficulty in obtaining pure measurement conditions not influenced by surrounding anatomy. Rat spinal cord injury models, particularly in the traumatic setting, have a similar pathological response to humans through an influx of inflammatory molecules across the three protective meninges and development of a cystic fibrotic core with little regeneration [68]. Other model organisms, such as mice, show different responses, namely regenerative capability [9].

The prime focus of modelling NT-SCI is to emulate its slow progression and expansion into the spinal space: limitations with current studies are the lack of appropriate compression timescales *in vivo* and difficulty in eliciting

compressive injury without causing excess, trauma-like damage to the cord. Non-traumatic compression models primarily utilise expanding materials in the cervical spine to represent a spondylitic myelopathy bone spur [45], [69]–[71]. However, these material properties may not produce the relevant *in situ* forces. Methods utilising force-inducing clips [72], forceps [73] and impactors [74] are suited for traumatic SCI, but compression using these approaches is difficult to graduate in severity, especially due to high stresses produced at instrument contact edges and focal apex [75]. Balloon compression is often used in NT-SCI scenarios due to unilateral inflation and direct compression on vasculature, but it is difficult to ensure the correct positioning due to tissue flexibility, and thus to record the resultant biomechanical parameters [20], [76], [77].

The majority of human SCIs take place in the cervical region, whereas 81% of experimental SCIs are performed at the thoracic level [78]. Many *in vivo* studies use a dorsal surgical approach, meaning the corticospinal pyramidal tracts are also affected during dorsal compression due to the small anatomical scale of the rat [21]. This is a limiting factor of modelling the variation in severity and location of NT-SCI in the rat *in vivo*, as well as clinical injuries most commonly manifesting ventrally.

In aiming to build a computational model representative of the vascular effects in NT-SCI, strain and functional output data from *in vivo* models are commonly used as comparators for validation. Quantitative strain data of NT-SCI *in vivo* is not readily available in the literature, particularly in terms of vessel occlusions. Current work presents vascular alterations through changes to

vessel thickness, density and number of bifurcations present (representative of collateral re-routing) [67], [79], [80]. Previous histological studies have indicated a reduction in local microvasculature by 33% [42] and that occlusion of the ASA affects a third of the ventral spinal cord and does not affect the pyramidal tracts [81]. Chronic compression has been reported *in vivo* to flatten, stretch and cause loss of microvessels in the spinal cord [42], [67], [82].

Balloon occlusion models have indicated that the rate of injury and lesion size are essential determinants of functional outcome [4]. Relative to injury profile, a study in dogs found that balloons of 2-mm produced 12.5-20% reduction in spinal canal diameter, whilst 4mm caused 28-56% decrease and 7mm caused 62-82% [12]. A balloon occlusion study in monkeys found that compressions deeper than 2mm occluded the sulcal arteries [20]. Longer timescales for occlusion worsened functional outcome but not by a significant amount. No symptoms were observed at occlusions less than 30%, which correlates with data from a rat compression study [65]. Other compression studies have found that the collapse rate of tissue at 30% and 50% strain does not differ significantly, but grey matter is more susceptible to injury and is affected first [64].

In terms of vascular response, a rat model of CSM showed animals had decreased SCBF and oxygen saturation at the compression site 4-weeks post-injury; this was significantly correlated with a decrease in dynamic motor evoked potentials and increased vascular re-distribution and angiogenesis [83]. Thoracic chronic compression models agree with this, a decrease in neurovascular functionality has been reported after 4 weeks and continues to

decrease over a period of 6 months [67]. Another study indicated a decrease in motor neurons was seen from 6-9 weeks after compression; loss of neurotropic factors was also seen and decompression was ineffective after 9-12 weeks of injury [45]. Minor compressions have triggered complete ischemia of lower thoracic segments of the rat spinal cord when maintained over long time periods [84] and irreversible damage has been seen at injury rates of 6m/s but this is of a more traumatic nature [6]. Early decompression of NT-SCI showed better functional outcomes compared to those who did not receive intervention [85]. Therefore, temporal longevity of compression is understood as a key contributor in pathological presentation, but this is difficult to model *in vivo* due to the timescales required. Therefore, a growing facet in medical research is the evaluation of pathologies *via* computational means.

1.5 *In silico* studies

In silico modelling employs parameters from *in vivo* or clinical settings in order to mathematically solve a real-world problem. The required parameters to validate the real-world scenario include geometry, material properties and the physics governing the problem. A benefit to *in silico* modelling is the ability to run parametric analysis from the same baseline conditions, which enables consistency and reliability of the output data which is difficult to achieve *in vivo*. However, there are limitations as to what extent the input assumptions can fulfil model requirements to report truly representative outcomes. Therefore, verification and validation of *in silico* models is a required and standardised

part of model development. It is acknowledged that there are inherent assumptions in the employed parameters, but these assumptions are required to balance physiological complexity and computational capacity. These assumptions can be difficult to validate in novel research areas such as NT-SCI, as few data points are available with the granularity required for implementation.

The majority of *in silico* models comprise of finite element methodologies, wherein systems are split into a mesh of elements and nodes for spatial discretisation on a 3-Dcoordinate system. Elements are small parts of the system that are discretised spatially and connected to each other by nodes that together create a finite number of points that represent a system of algebraic equations [86]. The elements represent shape functions determined by the position of its nodes (red dots). Nodes are shared between adjacent boundaries, allowing a whole model to be solved simultaneously, due to its interconnected element mesh (Figure 4).

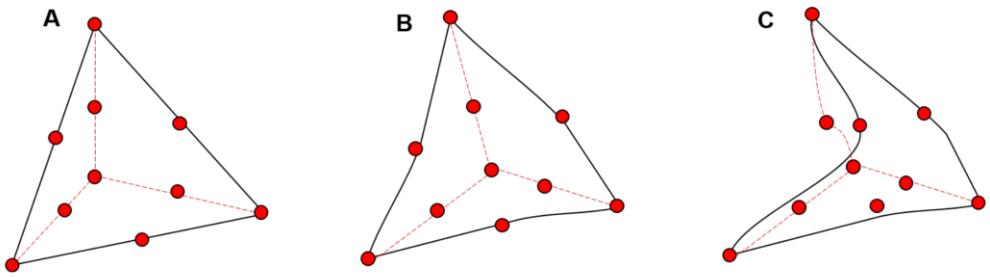

Figure 4: Ten-node tetrahedral elements in undeformed (a), deformed (b) and inverted (c) states.

When subject to external force, nodes move position relative to the spatial frame of a fixed coordinate axis (figure 4b) – this change in node position alters

the shape function and solves for the new geometry. This becomes problematic when elements are deformed so much they overlap neighbouring nodes or collapse within its own element shape to form inverted elements (figure 4c). Changes to element and node positions in space are continually solved and updated in a set of simultaneous equations, relative to the initial base parameters. Finite element models have been deployed for spinal cord injury simulations previously, predominantly for traumatic scenarios such as burst fractures [76], compressions [7], [23], [87], [90]–[92] and surgical interventions [93], [94]. With regards to spinal fluid mechanics models, research thus far has primarily focused on syringomyelia and the associated cerebrospinal fluid [95]–[97]. One paper has investigated spinal arterial and branch flow under compression [19]. The model consisted of the anterior spinal artery with three sulcal artery branches represented within the white matter. The sulcal branches extended through to the posterior end of the cord. The cord was modelled to have linear elastic material properties and did not differentiate between grey and white matter. It did, however, include the protective dura mater. The spinal cord and its anterior arterial system were represented through FSI for compression up to 10% strain at anterior, posterior and anteroposterior locations. The tissue stress response and change in blood flow through vessels was measured. The study found that 9.65% anteroposterior compression was most detrimental to the system and elicited a 50% decrease in arterial blood flow rate. Posterior injury decreased blood flow in the branch vessels but did not affect the ASA. Anterior compression was effectual on the ASA but not branch vessels – a 6.5% occlusion caused a 33% reduction in blood flow rate. The model did not

account for microvasculature in the system, which may allude to the severity of anteroposterior compression if the branches were occluded directly with no other source of blood. Therefore, the presence of microvasculature was an inclusion criterion for the model presented in the thesis, alongside the inclusion of oxygen modelling to better understand responses to ischemia development which has not previously been modelled in a spinal cord scenario. Blood flow modelling in the spinal cord has not been common, namely due to a lack of parameters and accurate data. At present, most vascular data is derived from recent advances in imaging and measurement techniques in mapping the vasculature [53], [82], [98], generating qualitative biochemical data from immunohistochemistry [39], [99]–[101] and quantifying changes (density, thickness, branching) to vessel architecture [73], [102]–[104]. Other vascular data points are derived from advanced imaging methods to examine perfusion, pressure and oxygen [18]. Generally, this is limited to only understanding these data relative to the change in spinal canal diameter, which is known not to be the only contributory factor. Granularity of data, such as the mechanical forces experienced by tissue, have not been available thus far except when represented by *in silico* models.

1.5.1 Geometry modelling

A challenge in modelling physiology is determining how much anatomical detail is required to output a valid representation. Many studies that extrapolate geometry from *in vivo* data commonly extrude 2-D microCT and histology images into a 3-D reconstructed stack of the geometry [105]. These

images require appropriate post-processing, scaling and segmentation for compatibility in the simulation software. Computed tomography (CT) and magnetic resonance imaging (MRI) of clinical cord sections give high geometric accuracy for anatomical segmentation and material property assignment through the ability to segment the inherent image greyscales and weighting intensities [106]. However, simplified, user-built geometries are often employed in early-stage models to account for computational cost [95], [105].

An added complexity in spinal cord anatomy are the cord associate structures, the spinal meninges and surrounding musculoskeletal architecture. Nerve roots and denticulate ligaments are commonly excluded from studies but have been represented as boundary conditions. Inclusion of the spinal meninges greatly affects compression mechanics by increasing tissue stiffness due to mechano-protection during stress transfer between the layers [107]. The arachnoid layer is extremely thin and shows no alignment in structure, so is assumed to have little protective effect or influence on *in silico* outputs [107]. Inclusion of the hyperelastic dura and pia maters influence compliant of the spinal tissue under compression [91]. However, most studies choose to only include dura mater, which under tension, has stiffness twice as great than the spinal cord [108]. Previously, on addition of spinal meninges, the site of impact and spinal meninges have experienced high stress but the cord itself showed lower stress, thus the anterior column structure was preserved [109]. Models commonly represent vertebral bodies as rigid because their deformation is suspected to be minor in comparison to the cord under NT-SCI conditions [6], [110].

With regards to current fluid-structure spinal geometries, cerebrospinal fluid is commonly modelled as a water-like fluid with viscous properties and a pure slip condition, therefore gradual contact behaves elastically and deformation is relative to contact pressure [111], [112]. Traumatic transfer of pressure through the cerebrospinal fluid acts protectively, by spreading stress and strains longitudinally within the cord [95]. Syrinx (pseudocyst) formation, commonly presented under the non-traumatic spinal cord compression umbrella as syringomyelia, has been shown to disrupt the protective cerebrospinal fluid pressure mechanics in the subarachnoid space by increasing fluid pressure closer to the syrinx and affecting the downstream fluid stress patterns which in turn disrupts transport mechanics [113]. However, the CSF layer is extremely thin (0.025-0.135mm), so requires further mesh complexity and computational expense [95] and is therefore neglected from this work.

1.5.2 Neural material properties

When assigning computational material properties, considering the conditions the parameters were derived from is important, as different sample testing methods can result in great variability. Such considerations should include strain rate, preconditioning, time postmortem, sample orientation, subject age and loading direction. Difficulties that influence the accuracy of experimental-derived soft material properties include the isolation, maintenance and preparation of the tissue [114]. Sectioning of the cord itself, especially from the *in vivo* rodent, is particularly difficult due to the dexterity and specificity

required to complete a full laminectomy, dissection and decalcification of vertebrae. Ensuring no damage to the spinal cord meninges – particularly the dura – is technically demanding. Tensile testing is common in spinal cord characterisation, despite indentation testing providing outputs of greater relevance. This is because indentation is extremely difficult to perform at such low mechanical thresholds on delicate tissues [115].

The spinal cord has previously been computationally modelled using linear elastic [19], [112], poroelastic [116] and poro-viscoelastic [117] properties. Simplistic, linear elastic studies [88] use spinal cord parameters approximated from the Bilston [118] study. Other models have implemented complex incompressible, hyper-viscoelastic properties, which are comparable to the loading-relaxation behaviour of the cord at all strain rates [91], [105], [117], [119]. However, experimental results in the literature vary in reported stiffness on increasing strain rates: this phenomenon is common in similar collagenous soft tissues and could be attributed to experimental variation, as described above.

Fundamental computational models in the research field have implemented linear properties with smaller displacements to minimise the constitutive behaviour of the cord [111]. These models are generally limited to coarser meshes and have not been fully assessed in terms of bio-fidelity and validation against the clinical scenario. Other non-linear models that employ large strains implement geometric non-linearity for inertial loading, however, these models generally use very small mesh sizes. The spinal cord is understood to have both hyperelastic and viscoelastic behaviour under deformation [108]. Results of cord simulation have shown that white matter has viscoelastic behaviour

under compression, assumed due to transverse isotropic alignment of the material [120]. Compressive behaviour of white matter is markedly less stiff than the tensile properties and is highly sensitive to loading – the viscoelastic properties are most important at low loading rates [112]. White matter is estimated to be 2-3 times stiffer than grey matter [121] and grey matter has been proven to be more mechanically rigid and fragile due to its higher tangent modulus and lower elongation ability [109]. Both white and grey matter stress-strain curves follow a non-linear to linear (>15% strain) to plateau failure pattern under tensile testing in the transverse direction. Non-linear behaviour is not markedly different between matters, but Young's modulus and stress are significantly higher in the grey matter linear region – which is linked to rupturing at lower strains [109]. As outcome predictors, maximum principal strain has been shown to best correlate with grey matter injury severity, whereas von Mises strain best with white matter injury [122], [123].

Models generally model the matter types via a continuum model, as the small element sizes required to model the boundary between the two. Previous studies separating the tissue matter had nominal effect on tissue deformation under transverse impact loads [95] – the individual injury thresholds for the different matters remains unknown. However, it is understood that isotropy of white matter material behaviour will not overestimate stiffness to produce incorrect force distributions, particularly in the toe region, under high strains or preloading but viscoelastic constitutive models claim to accurately represent rate-dependent behaviour of white matter [117]. It is debated whether quasilinear viscoelastic and four-element linear viscoelastic models are not compliant enough to represent the physiological stress-strain relationships

[119], converse to findings that human cervical spinal cord behaviours fit a quasilinear viscoelastic model [118]. Hyper-viscoelastic models absorb strains with greater ease than viscoelastic models; the lower strains and stresses are attributed to the wavy nature of hyperelastic fibre tracts [124]. Hence, the application of constitutive hyper-viscoelastic properties is deemed as the ideal material representation, as hyperelastic models alone are inappropriate for representation of the characteristic increased cord stiffness under strain.

Ideally, spinal cord and dura mater hyperelastic-viscoelastic constitutive properties are fit to an Ogden strain energy density function with Prony series decay of varying time constants; the Ogden function assumes hyperelastic material behaviour can be described by strain energy density function, from which stress-strain relationships can be derived and Prony series decay equations assume the shear and bulk moduli are represented by a decaying function of time [125]. A recent study implemented hyper-viscoelastic material parameters that fit its concurrent ex vivo experimental data of dynamic loading at three strain rates up to 60% deformation of the spinal-pia complex. The material properties were derived from unconfined compress of non-human primate of white matter, which were fit to an isotropic hyperelastic model using an Ogden constitutive model. Viscoelasticity was included using a quasi-linear viscoelastic formulation with normalised Prony series shear moduli and relaxation times [126].

The model will therefore be developed to basic linear elastic properties to reduce computational expense but will account for different properties between the grey and white matter.

1.5.3 Vascular modelling

Computational modelling of vasculature is well established in the field, but not as established in the spinal setting as it is in the brain [102], [127]–[129]. However, the brain and spinal cord are similar in vessel properties, flow and oxygen behaviours, so it is commonly assumed parameters are cross-compatible. Complexities arise in validating vascular networks and the assumptions applied between vessel sizes and scales. Blood flow can be modelled through hierarchical systems of tubes but the detail of capillaries at the microscale is usually too complex, therefore regional parameter averages are commonly implemented [130]. Material parameters are usually derived from axial testing data - these are only representative of a section of the strain model - fitting constitutive models to uniaxial data leads to slow convergence, inaccurate equations and unreliability [131]. The majority of arterial wall models assume material hyperelasticity, despite also having viscoelastic behaviour in the loading range, such as when influenced by small changes in blood pressure [132]. Modelling compliant vessels is physiologically accurate, but reduces shear stresses at peak flow relative to the pressure-distension relationship [130]. For ease in computational fluid dynamics, blood is commonly modelled as a Newtonian, water-like fluid with laminar flow at the spinal level, producing zero motion at the vessel walls [133]. This assumption is commonly implemented as the change of pressure in the vascular networks is assumed to not alter by over an order of magnitude, meaning viscosity changes are not significant enough to be modelled.

As mentioned previously, spinal cord vasculature ranges down to the micron-level, governed by complex perivascular structures and pressure and diffusion gradients. Combining these parameters is extremely complex, therefore modelling microvasculature as a porous medium has become a more common method. The key limitations in this are that large vessel models are commonly presented as one-dimensional network models, but these do not offer a full microcirculatory understanding. Network models are not as dependent on spatial discretisation so can avoid the need for geometry complexities by automatically altering outputs relative to those of neighbouring nodes, but this is very computationally expensive [134]. Therefore, newer models strive to develop porous systems representative of capillaries that link to the larger, penetrating feeder vessels. However, these models are still uncommon as the computational power required to couple free-porous flows is expensive [135]–[137]. In order to employ multi-scale and porous compartment variations, anisotropic permeabilities are required to represent the spatial variation: in non-continuum models, anisotropy is usually neglected for model simplicity [136]. Brain capillary networks have been reported as isotropic, meanwhile larger vessel regions are anisotropic. However, it has been reported that isotropic permeability redistributes blood to compensate within the model when under strain, but anisotropic and isotropic conditions show less variation in the healthy setting [136]. Limitations in current vascular models are the lack of outlet impedance boundaries or energy loss pathways [133]: simple models that apply zero pressure outlet conditions, or sink functions, do not consider the relationship of downstream vessels, or conservation of energy but these again require added computational expense.

Many vascular studies do not model fluid-structure interaction (FSI) due to the requirement of Eulerian-Lagrangian (flow field at a given space or time) methods over just Lagrangian (fluid flow through a field), which adds a huge level of computational complexity. FSI requires extra solid parameterisation which may not always be essential if enough data is known about the blood flow and oxygen behaviour for only modelling the relative pressure changes, however, as aforementioned, NT-SCI response is concurrently affected by solid compression and ischemia.

Few have studied spinal vasculature dynamics *in silico*: key papers have produced basic linear elastic models. Results indicated the thoracic region of the cord relies heavily on the anterior spinal artery: on a mild anterior 6.5% vessel occlusion, a 67% decrease in blood flow has been reported. Conversely, deformation of the posterior cord vessels greatly affected smaller branches [19].

1.5.4 Oxygen transport models

In modelling oxygen transport, the core mechanisms to consider are molecular diffusion, convection, blood saturation and hematocrit, reaction kinetics and tissue consumption of oxygen. The Krogh cylinder model is the simplest mathematical model that represents oxygen concentration inside a tissue by simulating a single capillary supplying oxygen to a surrounding concentric cylinder of tissue. Axial diffusion and convection are neglected from this model. Extensions have been added, namely the change in oxygen from artery to vein as a linear function of axial length, accounting for intracapillary and axial diffusion in brain models and in representing a number of parallel capillaries in

a network [138]. Oxygen concentration should account for changes down vessel radial and longitudinal axes, as well as the dissociation of oxygen relative to saturation.

Many non-stationary cerebral models now assume blood and tissue as a bi-fractional homogenised material, where convection, diffusion, consumption of oxygen in blood and tissue are the key drivers. Namely, the non-linear Hill equation represents the relationship between oxygen concentration in plasma and blood and enables penetration from plasma to tissue through capillary walls to be built in as a core assumption. Another core model uses the Michaelis-Menten equation, which prescribes a sink term for consumption of oxygen in tissue [139]. Both these theories together are computationally expensive. Green's functions have previously been applied to calculate oxygen consumption relative to the spatial distribution of tissue oxygenation, by assuming consumption is uniform and dissociates non-linearly using Hill's theorem of haemoglobin binding [127] – which, again, is computationally expensive to implement [140]. For this reason, a simpler no-flux model is preferred, portraying diffusive capability as a porous medium in the extravascular space. However, no-flux boundary conditions influence microvasculature oxygen transport gradients to overestimate hypoxia levels. Other simplified methods assume oxygen concentration is driven by convection, where the diffusion rate is proportional to the difference in oxygen concentrations between plasma and tissue [141]. Some models neglect the non-stationary and non-linear aspects of the blood-plasma relationship, or assume outflows do not depend on the surrounding tissue concentration,

impose independence of metabolic rate from tissue oxygen concentration or impose non-uniform consumption rates to simplify the oxygen model [142].

Recent trends utilise continuum models which spatially homogenise variables between blood and tissue fractions but this averages oxygen concentrations and smooths gradients to enable convergence [139]. This makes continuum models less useful in determining individual capillary behaviour but is useful for larger anatomy models where vessel distribution is dense and flows can be coupled to known fluid models such as Darcy's law [142]. The inclusion of an effective anisotropic diffusion coefficient means the rate of diffusion is dependent on the concentration gradient, if a local permeability tensor is defined relative to its local geometry and concentration or pressure gradient, then oxygen transport can be solved for. In continuum models, lumped systems are commonly deployed in oxygen transport models where advection, flux and diffusion are defined on axial vessel nodes, axial vessel/surface nodes and axial surface/tissue nodes. These equations are then assembled into a lumped system by assigning a global index for the nodes in the three regions [143]. Lumped parameter models are often employed in modelling closed-loop, organ-scale circulatory systems [144]. Therefore, inclusion of oxygen transport and a consumption model is important to consider in development of the NT-SCI model. The use of a porous continuum model will be applied and appropriate permeability parameters investigated for accurate representation of blood and oxygen distribution in tissue.

1.6 Summary and research objectives

The current understanding behind NT-SCI is mostly biological: *in vivo* studies have identified pathways of dysfunction linking the disruption of vasculature, resultant ischemia and neural tissue injury. Relative to current quantitative data available for use in model parameterisation, the model presented here will emulate the rat system as means of correlating *in silico* data to recent experimental understanding, particularly whilst NT-SCI pathophysiology characterisation is still in its infancy. Quantitative datasets for accurate representation of human NT-SCI are still sparse, but it is assumed that elucidating the fundamentals required to model the pathophysiology in the rat would have some correlation to representation of the human system. It is known that chronic compression decreases microvessel density, causing ischemia, hypoxia and therefore neurological dysfunction. Compression also directly affects the spinal cord neurons by causing demyelination, apoptosis of neurons and oligodendrocytes [145]. These, together, are believed to trigger an ongoing inflammatory response which worsens over time and continues to exacerbate the vascular and neural cell dysregulation. However, the biomechanics resultant in these biological behaviours remain misunderstood in the literature. It is known that NT-SCI manifests symptomatically at strains of approximately 30% but variations in injury profile and location report differing outcomes across aetiologies. Few studies have investigated the development of NT-SCI at mild, pre-symptomatic strains [26]. Therefore, the aim of this body of work was to investigate the vascular response of the rat

spinal cord to subclinical, non-traumatic injury scenarios ranging in severity, location and injury profile.

This was to be achieved across three key objectives:

1) Method development of a porous fluid-structure interaction model that represents the spinal cord vasculature (chapter 3).
    a. Develop appropriate displacement methodologies relevant to non-traumatic injury within a fluid-structure interaction model.
    b. Investigation of porous model physics scenarios and material properties as representations of the vascular network in spinal cord tissue.
    c. Develop an appropriate oxygen transport model with consideration for oxygen consumption rate behaviour.

2) Identify the contributing parameters that are assumed to affect the prognosis of non-traumatic spinal cord injury (chapter 4).
    a. Verification of the mathematical model presented in chapter three.
    b. Validation of the base model against known literature *ex vivo* models.
    c. Derive hypotheses for parametric analysis of injury severity, location and profile from published *in vivo* and *in silico* data.

3) Elucidate the mechanical thresholds at which non-traumatic injury has effect on the vascular networks of the spinal cord (chapter 5).

a. Assess the effect of strain severity, quantified as changes in the base vascular dynamics.
b. Assess the effect of displacement location, quantified as changes in the base vascular dynamics.
c. Assess the effect of displacement profile, quantified as changes in the base vascular dynamics.

Chapter 2

Mathematical modelling

Relative to the aims of the thesis, this chapter discusses the core science and engineering principles that underpin the fundamentals of the computational model. The iterative developments that comprise the finalised model are presented in chapters three alongside the development processes undertaken and in chapter four as the verification and validation of model parameters. The model aim is to simulate non-traumatic deformation of the spinal cord and the resultant effects on blood flow and oxygen transport. Therefore, the key components for inclusion in the model are appropriate assumptions around: representation of the material, the behaviour of blood flow through arteries and spinal cord tissue and the resultant transport of oxygen, plus the coupling to external deformation that accurately represents non-traumatic compression. These components of the mathematical model will be discussed in detail in sections 2.2-2.6 of the thesis, followed by description of the numerical implementation in sections 3.2-3.6.

There are a multiplicity of models, as discussed in chapter 1, that focus on solid deformation of the spinal cord [91], [92], [111], [122], [146]–[148] and fluid-structure interaction of the cerebrospinal fluid [95]–[97], [149]–[153], but only one has been coupled to spinal blood flow [19] and none examine the effects on oxygen transport in the cord. There are models of blood flow and oxygen transport in the brain [127], [129], [134], [154]–[157] but none of these are actively coupled to solid deformation and instead simulate ischemia by reducing source fluid pressures. This assumption is not applicable to the

model presented, as the inclusion of solid deformation stresses is a core focus of the work - data around downstream stress effects and therefore reduction in arterial and tissue blood vessel pressures in the spinal cord does not exist.

The chapter details the selection and composition of the geometry, the governing physics and mathematical models and boundary conditions employed in the model.

2.1 Geometric representation of the spinal cord system

The minimum level of anatomical detail required to accurately represent the injury scenario will act as inclusion criteria for the model. For the spinal cord, grey and white matter will be represented separately. The spinal vascular system will include four key vessels in the thoracic spinal cord.

2.1.1 Spinal cord matter

Dimensions of the spinal cord geometry were taken from literature (3.75mm transverse x 3mm sagittal), based on the average of *ex vivo* measurements of the thoracolumbar canal of the rat [158]. The coronal dimension is extruded to represent the T8-T12 segments of the rat cord (14mm) [82]. The grey matter is modelled to take up 20% of the total cord cross-section, relative to known volumes of white and grey matter of the spinal cord [159].

Extraspinal anatomies - namely the dura, pia and arachnoid mater, meninges and vertebrae – will be neglected in the model to reduce computational expense. It has been reported that the dura mater is significant in absorbing external loading stress onto the cord and, in turn, does have downstream

preservative effect on CSF flow patterns [95], but this compensatory effect is primarily relevant in traumatic injury.

2.1.2 Spinal vasculature

The spinal arterial system is understood to be relatively inefficient in that it has no capacity for collateral circulation [48], thus downstream effects are pronounced. As reviewed in chapter 1, extraspinal, radicular arteries branch from the aorta to feed the tissue-supplying central and peripheral networks. The thoracic region of the cord has markedly fewer infiltrating radicular arteries and has few anastomosing connections, thus is primarily dependent on the anterior spinal artery [160] which increases thoracic tissue susceptibility to damage [48]. The T8-T10 region is prone to ischemia as it is a watershed region, where blood flows of opposing direction meet. These spinal levels are solely provided by retrograde flow derived from the ASA, and anterograde flow from the two posterior arteries [161]. For this reason and to avoid the complexity of a multi-levelled extrinsic system which would require levels of vascular remodelling and compensatory blood flow to be considered, the thoracic levels of T8-T12 are the focus of this work. In terms of NT-SCI incidence at these levels, thoracic myelopathy is rarer than cervical and is commonly caused by ossification of the ligamentum flavum, ossification of the posterior longitudinal ligament, disc herniation or cancer metastasis. A recent systematic review detailed that 61.5% (658 in 1070 patients) that presented with thoracic myelopathy were effected at the lower thoracic levels (T9-L1) [162]. The central anterior system feeds the sulcal arteries, responsible for supplying the grey matter by traversing through the anterior median fissure

[163]-[164]. The anterior and posterior arteries are assumed to anastomose at the capillary level, with distinguishable contact between the systems only at the terminating level of the cauda equina[164]. Therefore, the motor neurons at the end of the posterior horns are particularly susceptible to injury - due to a lower vessel density at the central and peripheral-derived capillary system cusp [47]. The peripheral system feeds the white matter with vessels that perpendicularly extend into the tissue from the pial vasocorona, a vascular structure wrapped around the outside of the cord, connected longitudinally by the two posterior spinal arteries. The model geometry was simplified to only include core feeder vessels identified as key for provision: the core anterior spinal artery, two posterior arteries that represent in-shoots from the vasocorona and the posterior spinal vein (figure 5) [82].

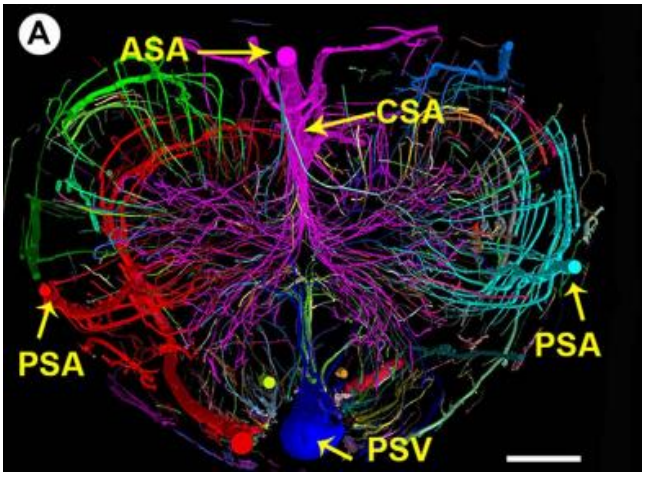

Figure 5: Synchrotron radiation micro-computed tomography of the rat thoracic spinal cord for sizing of core blood vessels. Adapted from Cao *et al* (2015) [82]**, licensed under CC-BY-4.0.** Nutrient vessels and their downstream vessel networks are distinguishable by colour (ASA = anterior spinal artery and its derivative CSA = central sulcal artery (purple), PSV = posterior spinal vein (blue), PSA = posterior spinal arteries (aqua+red)). 3-D pseudo-coloured geometry of the spinal cord microvasculature, based on vessel diameter ranging from small (red) to large (blue). Scale bar= 200µm.

The microvascular density and network complexity of vessels with diameters below 50µm are assumed to be represented by the porous continuum tissue in the model. The arteries and vein were presented as cylindrical geometries positioned within the white matter which allowed for continuity of flow and oxygen transport across from the free-fluid artery into the porous spinal tissue. To model the intrinsic microvasculature, a porous medium interfaced directly with the artery fluid through a defined shared boundary, ensuring continuity and transitional governance between free arterial flow and porous flow. Sketches of the geometries deployed computationally are as below (Figure 6).

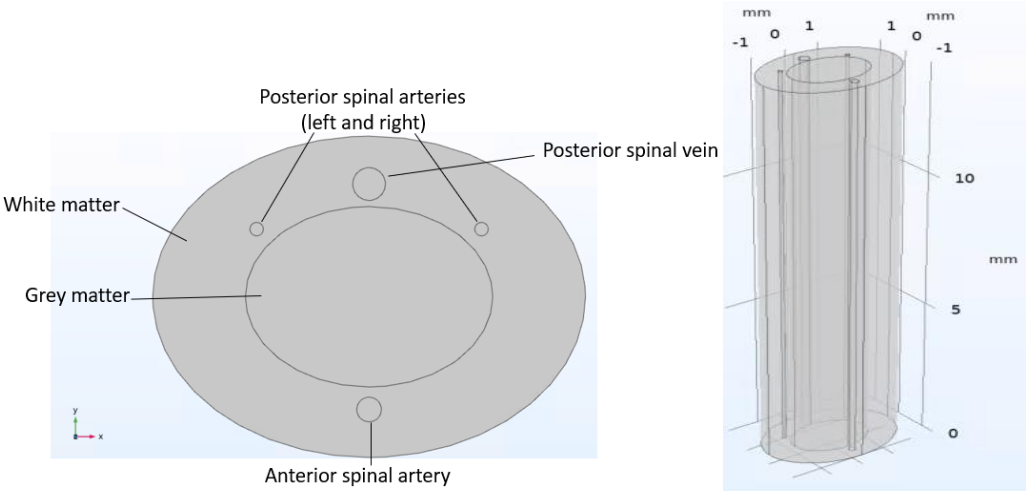

Figure 6: Transverse and sagittal views of the sketched computational model.

It is assumed the two posterior arteries that connect the peripheral network are sufficient to drive flow in the white matter, avoiding the complexity of the extrinsic pial network and its in-shoots. The posterior spinal vein is the main outflow vessel; the anterior radicular vein is not included to prevent skewed pressure gradients at the anterior spinal artery region. The dimensions of the core vasculature represented in the model are as below (Table 3).

Table 3: Diameters of sketched vessels.

Vessel	Diameter (mm)
Anterior spinal artery	0.11 [165]
Posterior arteries	0.062 [165]
Posterior spinal vein	0.146 [166]

All extrinsic vessels ran parallel to the five lower thoracic cord segments and were thus the equivalent length. After construction of the geometry, deformation of the matter anatomies is to be implemented, as in section 2.2.

2.2 Deformable solid mechanics

The model requires inclusion of solid deformation to understand the effect of strain on the feeder vessels and underlying porous spinal vascular tissue. In order to do so, external displacements are deployed onto the surfaces of the spinal cord at anterior, posterior and anteroposterior positions.

To solve for displacement in a solid, deformable body, the Newtonian equation of motion – here presented in summation convention - can be considered, where $\boldsymbol{\sigma_{ij}}$ are internal stresses (i.e. σ_{11} is stress applied in the x-direction to a surface normal to the x-direction, σ_{12} is stress applied in the y-direction to a surface normal to the y-direction, and so on), $F_i^{(e)}$ are external forces on a body, $\boldsymbol{\rho}$ is density and $\boldsymbol{\alpha_i}$ is material acceleration:

$$\frac{\partial \sigma_{ij}}{\partial x_j} + \mathbf{F}_i^{(e)} = \rho \alpha_i \qquad [1]$$

Solving the equations of motion together with a constitutive model for linear elastic solids allows for calculation of displacements, stresses and strains. In order to do so, the relationship between stress-strain and strain-displacement can be defined through the generalised form of Hooke's law (presented in summation convention), where the stress tensor (σ_{ij}) is related to the strain tensor (ε_{kl}) via the fourth order constant elasticity tensor (C_{ijkl}):

$$C_{ijkl} = \frac{\partial \sigma_{ij}}{\partial \varepsilon_{kl}} \quad [2]$$

Due to the presence of isotropic materials, the material planes have elastic symmetry and therefore the stiffness tensor is simplified. C_{ijkl} is determined by the material elastic moduli and Poisson's ratio:

$$C_{ijkl} = \frac{E}{2(1+\nu)}(\delta_{il}\delta_{jk} + \delta_{ik}\delta_{jl}) + \frac{E\nu}{(1+\nu)(1-2\nu)}\delta_{ij}\delta_{kl} \quad [3]$$

Due to the simplicity of the mathematical model for linear elastic properties in deformation, relative to the complexity required for the rest of the model, these models were implemented. The spinal cord is fixed at the top and bottom and at the opposite side of the deformation to prevent free movement in space and to emulate containment of the cord within the spinal cord canal.

2.2.1 Material properties

As discussed in chapter 1, it is generally agreed that spinal cord tissue under load displays hyperelastic-viscoelastic properties; these non-linear laws represent the differentiation between white and grey matter loading-responses which are due to differences in neural fibre structure [7], [107], [118]. However, for low, quasistatic strains, simplification of the tissue response to that of linear elastic behaviour was deemed appropriate, as the slow deformation rates allow for tissue relaxation. Linear elastic properties have previously been employed in spinal cord modelling for simplification in investigative modelling [147], akin to those utilised here (Table 4).

Table 4: Material properties of the solid model domains [153].

Material	**Young's modulus (Pa)**	**Density (kg/m^3)**	**Poisson's ratio**
White matter	5000	1050	0.4
Grey matter	10,000	1050	0.4

Young's modulus (*E*) defines the strain a material undergoes when a specific stress is applied. In a porous model such as that presented here, *E* represents the elasticity of the solid skeleton of the tissue. The modulus was derived from radial compressive and tensile testing on whole cord samples [167]. Radial measurements are useful here as this model looks to understand the strains through the transverse plane of the cord, which will be affected most by the compressions to be applied. The modulus presented was derived from data that did not differentiate between the grey and white material properties and

assumed a general continuum stiffness of the tissues. However, in previous computational models [153], grey matter has been assumed as double the stiffness of the white matter, relative to other studies detailing its tension and compression values as 1.7-2.1x of white matter, respectively [109],[168]. Poisson's ratio (v) is the ratio of how much a material deforms in a known direction when deformed by a load applied from an opposing direction. The ratio employed here was derived from compression studies of bovine spinal cord grey and white matters; ratios closer to 0.5 have been used in poroelastic models but these are near incompressible [169]. Due to the inclusion of microvascular networks in this model, a lower poisson's ratio that was in line with the literature that considers compressibility of the tissue was deemed suitable [109]. Density (ρ) is the mass per unit volume of a material; soft tissue density is primarily composed of water, therefore spinal cord tissue is assumed to have densities similar to that of water and of that known for brain tissue [96],[170]. Relative to previous models that have utilised porous skeletons to represent the spinal cord tissue [96], [153],[171], the values presented in table 4 were employed. On finalisation of the solid mechanics properties, implementation of fluid dynamics that represent the spinal cord arteries and its microvasculature is required, as in section 2.3.

2.3 Arterial blood flow model

Extrinsic, radicular arteries (ASA, PSA) are defined to behave as laminar, free-flowing fluids governed by the Navier-Stokes equations:

$$\rho\left(\frac{\partial \boldsymbol{u}}{\partial t} + \boldsymbol{u}\cdot\nabla\boldsymbol{u}\right) = -\nabla p + \nabla\cdot(\mu(\nabla\boldsymbol{u} + (\nabla\boldsymbol{u})^T) \qquad [4]$$

Blood is a non-Newtonian fluid, but for the purpose of computational simplicity, was modelled as an incompressible, Newtonian fluid which is commonplace is blood models. This meant the fluid viscous stress linearly correlated to local strain rate, related by a constant viscosity tensor independent of stress state and flow velocity. Non-Newtonian fluid viscosity is dependent on shear rate; blood is shear-thinning, wherein viscosity decreases as shear rates increase, namely due to changes in fluid haematocrit - the ratio of red blood cells to total blood volume [172].

At smaller scales, such as that of the rat spinal cord microvasculature, flows have high viscosity due to dominance of advection over inertia - therefore reduction of the Navier-Stokes equation to Stokes flow (equation 6) is appropriate [151].

Reynolds number (Re) is representative of the ratio between inertial and viscous forces at a defined velocity (U) and length (L), where ρ is density and μ is dynamic viscosity:

$$\mathrm{Re} = \frac{\rho U L}{\mu} \qquad [5]$$

As the Reynolds number for the rat-scale ASA was lower than 2300 (Re=2.19), it is assumed laminar flow was sufficient for the arterial blood flow. The continuity equation for incompressible flow is:

$$\nabla \cdot \mathbf{u} = 0 \qquad [6]$$

where **u** is the velocity vector. In- and outflow pressures are prescribed as stress conditions with a vanishing tangential stress condition in flows with low Reynolds numbers, where $\frac{\partial u}{\partial n}$ is the normal derivative of the normal velocity component and *n* is normal to the boundary:

$$-p + 2\mu\frac{\partial u_n}{\partial n} = F_n$$

$$\mu\frac{\partial u_t}{\partial n} = 0 \qquad [7]$$

Stress conditions are employed as pressure gradients assigned to the inlets of the arteries and vein (Table 5) to achieve the respective appropriate velocities of 60mm/s, 6.5mm/s and 0.5mm/s from the literature [172]. Flows are assumed to be fully developed and outlets are assigned prescribed pressures of zero. Fluid walls are modelled as a no-slip condition, wherein fluid velocity relative to the wall velocity is zero.

Table 5: Boundary conditions implemented to simulate blood flow transport through the spinal vascular network.

Tissue	Pressure inlet condition (Pa)
ASA	2000
PSA (L+R)	750
PSV	-200

The vessels are fixed at the top and bottom to prevent free movement in space and to emulate connectivity to upper and lower segments of the cord that were not modelled. Free boundary conditions are employed on the cylindrical walls to enable movement relative to the direction of compression.

2.4 Microvasculature blood flow model

In order to avoid the complexity of microvascular networks, porous media continuum models are commonly utilised in tumour and tissue modelling to ascertain tissue ability to transport molecules [135], [136], [173]. A porous continuum model is employed here to mathematically simplify the vascular network and its response to injury. At low Reynolds numbers up to 10, porous flow is governed by Darcy's law, when pressure gradients are the driving force. The capillary-dense microvasculature of the rat spinal cord is assumed to have a Reynolds number of 0.003, therefore less than 1, meaning Stokes and pressure-driven Darcy flows are sufficient to represent microvascular fluid behaviour. Darcy's law is pertinent in the spinal cord, where dense neural fibre and vascular arrangements result in low system permeability and porosity [97].

Porous models have been employed in other biological systems, namely the brain and liver, to avoid the complexity of the system geometry and the resultant boundary conditions [135], [136], [174]–[177]. Porous systems have been utilised to investigate cerebrospinal fluid behaviour in the parenchyma and perivascular spaces, as well as the poroelastic effects of loading by syrinx formation onto CSF behaviour [96], [97] which have been able to model an increase in fluid pressure under syrinx compression. Other applicable modelling approaches that are commonly deployed for brain vasculature are one-dimensional network models wherein material anatomy-level detail is not prescribed, but spatial changes to conditions are calculated relevant to their neighbouring network nodes [129]. However, the interactivity between the

spinal cord porous skeleton (matter fibres) and pores (blood vessels) are essential to include here.

The intricate geometry and functionalities of the spinal cord microvasculature are difficult to model, therefore modelling these complex flow networks as a porous system reduces computational workload by collating the individual complexities into a continuum. Porous flow variables and intrinsic fluid properties are defined at a point in space, by averaging the variable or property over a certain control volume surrounding that point. This control volume is small compared to the problem dimensions but sized to ably fit pores and solid matrix elements. With this, porosity of a material is defined as the fraction of the control volume occupied by pores. Intrinsic volume averages correspond to a unit volume of the pores, meaning fluid properties such as density and viscosity can be considered as continuous with corresponding free-flow regions. Porous flow velocity is defined by a superficial volume average - the Darcy velocity – which is the volume flow rate per unit cross section of the medium [153]. In Stokes flow, the conservation of momentum and continuity of mass equations are simplified to compute velocity and pressure fields of the fluid. Frictional resistance from the porous matrix hinders pressure-driven fluid momentum between pores – hence, velocity (**u**) is determined by the matrix permeability (κ), pressure gradient (∇p) and fluid viscosity (μ):

$$\mathbf{u} = -\frac{\kappa}{\mu}\nabla p \qquad [8]$$

Interior boundaries require continuity boundary conditions to ensure pressure and mass flux are continuous, where **n** is normal to the boundary:

$$\mathbf{n} \cdot (\rho_1 \mathbf{u}_1 - \rho_2 \mathbf{u}_2) = 0 \quad [9]$$

Dirichlet conditions are applied at inlets, where $p = p_0$ and p_0 is a known pressure from the literature. Internal walls are assigned no slip conditions, as in the free-flow setup. External boundaries are constrained to have no flow, where **n** is the vector normal to the boundary:

$$\mathbf{n} \cdot \rho \frac{\kappa}{\mu} \nabla \mathrm{p} = 0 \quad [10]$$

However, as the model is only representative of the T8-T12 segments of the spinal cord, outlet conditions are employed at the upper and lower boundaries of the porous medium to enable continuity of flow to adjacent spinal segments. No slip wall conditions were applied to the external tissue walls. The condition allowed for outflow perpendicular to the selected boundary, where U_0 is a specified pressure value:

$$-\mathbf{n} \cdot \rho \frac{\kappa}{\mu} \nabla \mathrm{p} = \rho \mathrm{U}_0 \quad [11]$$

Darcy's law may be representative of the intrinsic flows seen within the spinal tissue, but arterial flows behave as free-flowing fluids. Therefore, solving for Navier-Stokes flow adjacent to a region defined to behave under Darcy's law does not account for viscous effects from the free flow. Inclusion of the

Brinkman equations at the free-porous transitional boundary was required to account for the viscous forces and steep pressure gradients between the two regions.

The Brinkman equations (equation 12) govern fast-moving fluids in porous media by extending Darcy's law to include the dissipation of viscous shear energy. For incompressible flow at the free-porous transition region, the continuity and momentum equations – where density (ρ), velocity vector (**u**), porosity (ε_p), time (t), pressure (p), dynamic viscosity (μ), permeability (κ) and mass source/sink (Q_m) - combine to form the Brinkman equations:

$$\rho\nabla\cdot\mathbf{u} = \mathrm{Q_m}$$

$$\frac{\rho}{\varepsilon_\mathrm{p}}\left(\frac{\partial\mathbf{u}}{\partial t}\right) = -\nabla p + \nabla\cdot\left[\frac{1}{\varepsilon_\mathrm{p}}\{\mu(\nabla\mathbf{u} + (\nabla\mathbf{u})^T) - \frac{2}{3}\mu(\nabla\cdot\mathbf{u})\mathbf{I}\}\right] - (\kappa^{-1}\mu + \frac{\mathrm{Q_m}}{\varepsilon_\mathrm{p}^2})\mathbf{u} \quad [12]$$

The variables are solved in both the free and porous fluid regions, enabling continuity of pressure for deduction of velocities. For this to be feasible, a stress discontinuity was present at the free-porous boundary, for absorption by the porous matrix. The Brinkman equations account for fluid drag as proportional to the flow velocity through the porous matrix, as in Darcy's law.

On inclusion of a porous continuum model, appropriate material properties are required for accurate representation of microvascular behaviour.

2.4.1 Microvasculature porous media properties

Grey and white matter are assigned different porous material properties due to their differing solid skeleton structures, composed of neuron cell bodies in

grey matter and myelinated axons in white matter, plus the variance in their underlying vascular anatomy (Table 6).

Table 6: Material properties of the fluid model domains.

Material	Density (kg/m^3)	Viscosity ($Pa \cdot s$)	Porosity (ε)	Permeability (κ)
Blood	1060 [19]	0.0032[178]	-	-
Oxygen	1.331 [179]	-	-	-
White matter	1050 [180]	-	0.4 [180]	4.28×10^{-4} mm^3skg^{-1} [136]
Grey matter	1050 [180]	-	0.25 [181]	$1.234mm^3skg^{-1}$ [136]

Porosity is defined as the fraction of the volume that is occupied by pores; therefore zero porosity would equal pure solid regions and one would equal free flow. Porosities of white and grey matter have recently been found to be 0.396 and 0.456, respectively [153]. These values do not include blood vessels as the vessels are accounted for in the solid skeleton for the purpose of a cerebrospinal fluid model where vessels are neglected. Therefore, it is assumed that as white matter is a fibre-dense tissue that the porosity value is likely correct, meanwhile the grey matter porosity is likely more akin to that of the brain due to its microvessel density. It is understood that porosity is a variable property, in that it is dependent on fluid pressures of blood vessels and cerebrospinal fluid, as well as changes to the solid skeleton structures of vessels and neural fibres. This adaptability is not accounted for here, but the tissues are designated different porosity values. The values employed for the white matter are derived from neurite orientation and dispersion density

imaging (NODDI) of the white matter (ε=0.4) [153] and from extracellular space fraction studies of the rat ventral grey matter (ε =0.2) [181]. The NODDI methodology calculates the volume fraction of the intracellular, extracellular and cerebrospinal fluid compartments via their respective signals derived from diffusion-weighted MRI scans. The orientation of axons and dendrites can be calculated from these signals, which understood white matter to be anisotropic and grey matter to be isotropic in terms of fibre dispersion. The porosity value represents the pore fluid region, i.e., the extracellular fluid compartment. For the grey matter, porosity was derived from microelectrode analysis of concentration-time profiles of the relatively impermeable TMA+ which had been applied onto rat spinal cord grey matter by iontophoresis (electrical stimulation to aid molecules across permeable barriers). The concentration of ions was in inverse proportion to the side of the extracellular space fraction [181].

Permeability is defined as the capacity of the porous medium to transmit flow, which accounts for pore size, orientation and interconnectivity. White matter is reported to have anisotropic permeability in the literature [180] but for simplicity is represented as isotropic here. Capillary permeability is assigned to the white matter as a tensor, as it is primarily connected to the extrinsic feeder arteries (ASA and PSAs) and sparse traversing arterioles. The grey matter is assigned arterial zone permeability as a scalar due to its dense microvascular and sulcal artery network. The values are derived from a multi-scale homogenisation of local-scale blood flow equations. These produced an averaged Darcy's law of microvascular flow in cerebral tissue, which includes a permeability tensor derived from local topology. The model is extrapolated into a network model

to derive local permeability tensors, which converge into an effective permeability with scale [182].

With respect to the structure-function relationship of the physiology, the importance of distinguishing matters of varying porous properties and supplying structures is pertinent. Studies into CSF flow in perivascular spaces identify flow to have parabolic-like velocity profiles that do not behave relative to the Brinkman equations, so CSF models focus on Darcy's flow. It has been found that perivascular pores were not concentric circular annuli corresponding to vessel shape, but were flattened, elliptical structures [151]. These data may be pertinent in regard to this thoracic cord model which has to account for watershed areas with larger spacing between vessels and therefore a correction in permeability, so the model assumed pore shape was accounted for by addition of a default tortuosity correction factor.

2.5 Oxygen transport

In order to understand the effect of compression and blood flow as aspects of tissue response, oxygen modelling is needed to elucidate the thresholds at which ischemia may begin to trigger hypoxic pathways. Oxygen transport is driven by convection-diffusion from the artery to the porous capillary flow, governed by Brinkman's law which account for viscous effects when transitioning in size from arterioles to capillaries. The model assumes that blood and oxygen is derived from the three provisional arteries and assumed progression of blood through the microvascular system and its oxygen consumption as dependent on the pressures that stem from the source artery.

A consumption function is employed throughout the porous medium to compensate for absent venous structures in the tissue.

Oxygen transport is driven by the convection-diffusion equation (equation 13); convective transport is driven by the free and porous fluid pressure gradients (effected upstream by solid deformation). Diffusion parameters are based on data of oxygen transport in the rat brain [183]. In order to calculate the concentration field of a dilute solute in a solvent, transport is represented by Fick's law for diffusion and flow field momentum for convection. Mass conservation for species i, where c is concentration, t is time and **u** is velocity leads to:

$$\frac{\partial \mathrm{c}}{\partial \mathrm{t}} + \mathbf{u} \cdot \nabla \mathrm{c} = \nabla \cdot \mathbf{J}_\mathrm{i} + \mathrm{R} \qquad [13]$$

Mass flux (J_i) defines the diffusive flux tensor as $J_i = -D\nabla c$, where D is the effective diffusivity of oxygen, and R is the consumption rate expression. In the porous medium, Darcy's velocity is the main determinant of oxygen transport through the matrix - average linear fluid velocities ($\mathrm{u_a}$) provide an estimate of porous fluid velocity and therefore carried oxygen within a saturated matrix:

$$\mathrm{u_a} = \frac{\mathbf{u}}{\varepsilon_\mathrm{p}} \qquad [14]$$

In the numerical implementation of the model (chapter 3), the non-conservative form of mass conservation is employed, assuming the fluid is incompressible and divergence free:

$$\frac{\partial}{\partial t}(\varepsilon_p c_i) + \frac{\partial}{\partial t}(\rho c_{P,i}) + \mathbf{u} \cdot \nabla c_i = \nabla \cdot [(D_{D,i} + D_{e,i})\nabla c_i] + \mathbf{R}_i + \mathbf{S}_i \quad [15]$$

The left-hand side of the equation represents liquid concentration (c_i) in the porous matrix (ε_p), the amount of solvent adsorbed to solid particles ($c_{P,i}$) and concentration in the gas phase ($c_{G,i}$). The last term represents convection derived from the velocity field. The right-hand side of the equation represents transport *via* porous media dispersion (D_D) and effective diffusion (D_e), accounting for reactive (R_i) and arbitrary sink/source (S_i) terms. With respect to effective diffusivity, saturated porous media is governed by tortuosity (τ_L) and the diffusion coefficient for solvent dilution in liquid (D_L) is governed by:

$$D_e = \frac{\varepsilon_p}{\tau_L} D_L \quad [16]$$

The inclusion of tortuosity accounted for the reduction of diffusivity as fluid moved through porous channels.

Inflows and outflows of oxygen were defined as pointwise constraints at the same boundaries as the free flow inlets and outlets, where n is normal to the boundary:

$$\mathbf{n} \cdot (-D\nabla c) = 0 \quad [17]$$

Exterior solid walls where there is no mass flux behaved as:

$$-\mathbf{n} \cdot \mathbf{J}_i = 0 \quad [18]$$

The fundamental maths was implemented alongside parameters essential for driving convection and diffusion of oxygen through porous material.

2.5.1 Oxygen transport properties

The conditions applied to model oxygen transport through vascular networks of spinal tissue are as in Table 7.

Table 7: Boundary conditions implemented to simulate oxygen transport through the spinal vascular network.

Tissue	Implementation	Concentration (mol/m^3)
ASA	Pointwise concentration constraint	15
PSA (L+R)	Pointwise concentration constraint	30

Oxygen transport is coupled to the free-porous flow convection-diffusion properties wherein convection is defined as the velocity output from the Brinkman flow model. Diffusive effects are usually negligible in vascular networks but are pertinent here due to the very low microvascular velocities. The model is attributed a diffusion coefficient of $1.5\times10^{-7}m^2/s$ as a scalar value for isotropic diffusion, corrected for by employing a tortuosity model of 0.52, where the default is 1. Tortuosity is the ratio of the length of a streamline in a porous matrix between two set points, as compared to the straight-line streamline length. Dispersion accounts for spreading of the solvent in the direction of flow in porous media, however, due to these small velocities, the dispersivity tensors for longitudinal and transverse directions were accepted as the default. In central nervous system tissue, it has been assumed that diffusive movement is the dominant driver of fluid flow, but bulk flow is

understood to be particularly influential in pathological scenarios [151], plus prior models using diffusive drivers have not accounted for vascular networks as is required here.

2.6 Fluid-structure interaction

As the final consideration for the mathematical model, coupling the solid and model components of the model is required. To couple the physics, shared conditions are required at the communal solid-fluid boundary (artery/tissue wall). Navier-Stokes flow is solved for the conservation of momentum and mass through computed fields of velocity and pressure while the solid interface solves Navier's equations for displacements. An Arbitrary Lagrangian-Eulerian (ALE) formulation is implemented to couple changes to the combined fluid-structure mesh positions, through employment of a Eulerian spatial frame for the fluid component of the model and a Lagrangian material frame for the solid component.

The Eulerian mathematical method represents the spatial frame which is relative to a fixed set of axes with no reference to the physical components of the system. This means the field variables are expressed as functions of the fixed coordinates in the spatial frame. The Lagrangian method represents the material frame, wherein the mathematics have reference to small volumes of material, which move within the object space. Therefore, the material frame coordinate systems would displace with the physical component as the object dimensions alter in the spatial frame. Under low-level strains, the spatial and

material frames essentially coincide because the mechanical displacement is small relative to the whole object. However, under larger deformations, linear approximations are no longer suitable and geometric nonlinearity is required, known as the Green-Lagrange strain. This separates the material and spatial frame via a frame transformation from the computed mechanical displacement. In order to coordinate the two frames, the mesh frame acts a mathematical map between them, wherein both sets of equations are transformed into a mesh to be solved. Under displacement, the ALE method adds more equations to account for positions of mesh elements in neighbouring features to displace in the fluid Eulerian spatial frame. Therefore, deformation effects are shared between solid and fluid features, as defined by the full FSI coupling. At the boundaries between the fluid Eulerian and solid Lagrangian features that have these additional equations, a boundary condition must be employed to displace the spatial frame identically to the material frame displacement. The deformed elements of the fixed spatial frame are smoothed to ensure stable solving of the numerical problem, rather than determining of the exact node positions.

The FSI coupling is defined so the structural velocity of the solid deformation behaves as a load boundary condition for the fluid which displaces the original node positioning to create an overall change in shape. Total fluid force (f) on the solid boundary is the negative of the reaction force on the fluid itself, where n is normal to the boundary, μ is the dynamic viscosity, **I** is the identity matrix and $\mathbf{u}_{\text{fluid}}$ is the fluid velocity field:

$$f = \mathbf{n} \cdot \left\{ -p\mathbf{I} + \left(\mu(\nabla \mathbf{u}_{\text{fluid}} + (\mathbf{u}_{\text{fluid}})^T) - \frac{2}{3}\mu(\nabla \cdot \mathbf{u}_{\text{fluid}})\mathbf{I} \right) \right\} \quad [19]$$

The Navier-Stokes equations are solved in the spatial frame, therefore force derived from the fluid model is transformed and transmuted to the material frame where the solid mechanics are solved. This transformation was defined by solving with dv and dV, mesh element scale factors for the spatial and material frames, respectively:

$$\mathbf{F} = f \cdot \frac{dv}{dV} \quad [20]$$

The rate of change of solid displacement acts as a moving wall for the fluid domain. The spatial frame deforms with a mesh deformation equal to the solid displacement while the fluid domain mesh is free to move, so the fluid mesh node positions are adjusted by the ALE method to account for the moving solid walls. These mechanisms enable the smoothing and coupling of tissue deformation onto the blood for investigation of strain effects on arterial and microvascular flow behaviours.

2.7 Summary

The chapter has outlined the equations, theory and assumptions behind the key aspects of the model which are supported by the literature. In understanding the mathematical models required to couple the deformable tissue mechanics, arterial and microvascular flows plus the oxygen transport capabilities of the spinal cord system, the following chapter implements the numerical methods to solve these mathematical models.

Chapter 3

Development of the computational implementation

This chapter presents the numerical method and development of a computational approach to implement the mathematical model described in chapter 2. A porous-continuum model is to be employed, wherein oxygen from feeder arteries is transported by a free-porous (Brinkman) blood flow model through the spinal cord porous medium where oxygen is taken up by a consumption model applied to the tissue. The model is driven by three arteries whose viscous effects drive blood through the tissue via Brinkman and Darcy flows which allows for both convection and diffusion of oxygen to be represented in the tissue. With regards to co-simulating the fluid and solid dynamics: the free-flowing artery blood sources and the spinal tissue porous microvasculature will both undergo mild tissue deformations which are coupled through a fluid-structure interaction (FSI) interface. This accounts for the effect of external strain on the blood sources, where the resultant arterial pressures feed into the porous tissue fluid pressure and therefore transport and consumption of oxygen in the tissue.

This chapter explores the challenges in developing a practical computational framework and identifies the inclusion criteria and most suitable setup for final analysis; the chapter moves through each of these aspects in turn before validating the finalised model in chapter 4.

3.1 Model development overview and expected outcomes

The iterative method development process requires combining, refining and testing the fundamental solid, fluid, oxygen steps individually, before fully coupling the model (Table 8).

Table 8: Workflow of model iterations for investigation of parameters and setup.

Model iteration	Implementation step
Solid step displacement	Smoothing of mesh inversions at employed displacement boundaries
Fluid governance model	Investigating the required physics to accurate simulate the vascular network
Fluid flow parameters	Deriving the required material properties (porosity and permeability) and boundary conditions to achieve flow rates comparable to literature
Single Krogh cylinder (and coupled to vein)	Oxygen diffusion behaviour in tissue in stationary and time-dependent models
Oxygen consumption	Step function for sink term maximum and minimum limits
Fluid-structure interaction	Coupling of solid-fluid and fluid-oxygen models

This chapter focuses on these developments and presents the rationale and outcomes of model iterations, plus the decisions and actions employed to progress the model based on the evidence. The modelling steps taken within each of these iterations are highlighted below in Table 9.

Table 9: Summary of the modelling work undertaken to implement each aspect of the model iteration.

Model iteration	Steps in implementation	Outcomes
Anatomical representation selection	1: Extrinsic arteries with arterial walls included 2: Transversely coursing or parallel arteries 3: Shape of grey matter 4: Minimum representation of vasculature	1: Artery walls add unnecessary complexity to mesh 2: Parallel arteries to emulate direction of flow in cord 3: Ellipse shape 1/5th the size of white matter 4: Three arteries (ASA, PSA-L+R) and vein (PSV)
Solid step displacement	1: Moving mesh applied for larger deformations 2: Smoothed step functions developed	1: Clashes with moving mesh required for fluid in FSI. Automatic remeshing was viable but computationally expensive. 2: Prevents mesh inversion and enables parametric tests
Fluid governance model	1: Free flow co-located to porous Darcy flow 2: Brinkman's flow to reflect arterioles 3: Poroelastic behaviour of spinal tissue	1: Underestimates microvascular velocity 2: Produces velocities representative of artery→capillary flow 3: Could not be coupled to external deformation
Fluid flow parameters	1: Material properties of porous tissue 2: Boundary conditions for arterial flow	1: White matter defined with known spinal porosity [180]. Both permeabilities and grey porosity defined from rat brain data [136]. 2: Pressure gradients defined from inlets to outlet (Pa=0)
Oxygen consumption	1: Position of source vessel for spread in tissue 2: Consumption of oxygen in tissue	1: Krogh cylinder model was not representative of anatomy 2: Constant consumption is an overestimate. Ramp sink function deployed in spinal tissue. Arterial inlet concentrations defined.
Fluid-structure interaction	1: Coupling fluid to solid model 2: Coupling of FSI structure to oxygen model	1: Fully Coupled interaction required. Solid→fluid overestimates changes to blood flow. 2: Define reacting flow between Brinkman's and oxygen transport

Not all of the steps overviewed in Table 9 are discussed in this chapter as some iterations were discarded quickly due to a clash of the fundamental mathematical models or lack of convergence of the model. Below, Table 10 highlights the expected model outcomes for a healthy rat spinal cord as the baseline model for validation.

Table 10: Expected model outputs under healthy and ischemic/hypoxic conditions.

Geometry	**Flow profile**	**Expected velocity outcomes**
White matter (porous medium)	Flow to move circumferentially from the ASA through the white matter to the PSV. Permeability is lower so would expect slower velocities than grey matter, but anisotropic medium may allow a faster flow path	0.03mm/s
Grey matter (porous medium)	Faster velocities due to less resistance to flow through from the ASA to the grey matter, due to higher vessel density (higher fluid volume ratio as porosity)	0.6mm/s
ASA and PSA (free-fluid)	Unidirectional flow in the direction of high-to-low pressure (top to bottom of spinal cord in z-direction)	60mm/s= ASA[184] 6.5mm/s= PSA[102]
PSV (free-fluid)	Unidirectional flow in the direction of high-to-low pressure (bottom to top of spinal cord in z-direction)	10mm/s[102]

The assumed velocities of spinal tissues were derived from adaptation of known literature values:

- Grey matter in the rat spinal cord has an average flow rate of 62.5ml/100g/min [185-186] and white matter 17.5ml/100g/min [185-186] found by measuring flow rates via ^{14}C-antipyrine autoradiography with a scanning microscope photometer [185].
- The cross-sectional area employed for the rat spinal cord was 8.6mm^2 for white matter and 1.72mm^2 for grey matter (one-fifth of white matter, scaled from human dimensions) [187].
- By knowing the average flow rate and cross-sectional areas of the spinal matters represented by rudimentary ellipse geometries, the assumed velocities could be derived.
- The average velocity of blood through the matter microvasculature was 0.6mm/s and 0.03mm/s for white and grey matter, respectively.

Vessels of less than 5µm diameter present velocities of <1mm/s and it has been reported that the majority of the intrinsic vasculature are of this scale [52]. Arterioles are neglected from the geometry modelled here but are assumed as represented in the porous continuum by the Brinkman equations – the model should produce higher tissue velocities deriving from the feeder arteries of around 1.5mm/s [102]. The expected oxygen outcomes for healthy model scenarios are as below in table 11.

Table 11: Oxygen concentrations under steady-state and hypoxic conditions of the rat spinal model.

Vessel	**Oxygen concentration under normal conditions**
Artery (rat brain)	7.4mol/m^3 [188]
Arteriole (mouse brain) Porous tissue adjacent to arteries, governed by Brinkman flow	3.5mol/m^3 [16]
Venule (mouse brain) Porous tissue adjacent to PSV, governed by Darcy flow	2.08mol/m^3 [16]
Tissue	Rat brain interstitium [188] =0.74mol/m^3 Rat SC grey matter [186] =0.72mol/m^3 Rat SC white matter [186] =0.57mol/m^3

Data was manipulated from mmHg values into molar concentrations for implementation in COMSOL by converting the known literature values according to the ideal gas law. In order to model the varying aspects of the non-traumatic spinal cord injury pathophysiology in the thoracic region, numerical implementation of the mathematical models as means of achieving the expected outcomes presented here is to be done via building a computational finite element model. An introduction to finite element analysis (FEA) theory is below (chapter 3.2).

3.2 Finite element method

The partial differential equations (PDEs) responsible for the governing physics of the solid and fluid laws cannot be solved analytically, so these laws are

discretised into weak, integral formulations to be solved as numerical model equations. The numerical methods approximate the real PDE solutions by solving for the derivative of dependent variables (such as velocity or pressure) with respect to the change independent variables (such as coordinates or time). The finite element method works to convert functions within an infinite dimensional function space to a finite dimensional space, with final numerical solving of vectors within a vector space. When boundary conditions and relationships relative to other boundaries are defined, assumptions can be made about the progression of behaviour through the system.

In order to solve via finite element analysis, the geometry to be solved is split into a mesh comprised of elements and nodes. When two neighbouring elements overlap and share a node, the associated basis function overlaps, creating integrals of non-zero for the system matrix. Conversely, when there is no overlap between elements, the integrals and matrix contribution are zero. Therefore, zero values lessen the accuracy of the algebraic equations - hence why a denser mesh comprised of more elements gives a more accurate approximation. Element shapes include triangular, tetrahedral, quad and linear - the number, curvature and positioning of these elements is a key determinant of solution accuracy (Figure 7). In the 3-D environment, as presented in this work, tetrahedral elements are most commonly employed as they maintain the aspect ratio between elements as close to unity.

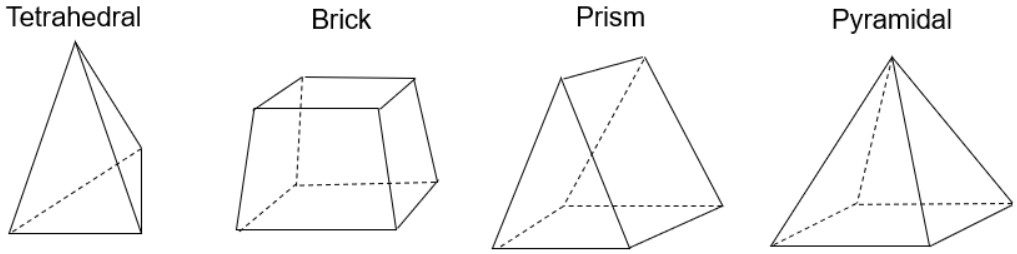

Figure 7: 3-D element types. Tetrahedral is most commonly used, meanwhile bricks can be preferred for solid mechanic problems. Prism and pyramidal elements are generally boundary transition elements.

The mathematical models and parameters reviewed in chapter 2 are to be implemented into the finite element modelling software, COMSOL (version 5.5a). The solver configuration to be used is the COMSOL default relative to the study step, which defines the relative solver configurations based on the variables to solve for, the solvers that are therefore applicable and their storage settings. The study and therefore solver configurations are defined by the employed physics interfaces, geometry and variables to be solved for that are presented in chapter two and in the remainder of this chapter.

This model will be simulated via a stationary study, when the equations solved for do not have time derivatives and the field variables do not change over time. In fluid flow, stationary studies compute the steady flow and pressure fields, which is relevant in NT-SCI relative to the long timeframes at which the injury takes place [86]. Similarly, in solid mechanics, it computes deformations, stresses and strains at static equilibrium. These are computationally easier to solve than time-dependent problems and are therefore to be employed in the

fundamental model of NT-SCI presented in this work; the nature of the multi-physics to be deployed in this model (solid and fluid) mean the matrices solving the physics solutions will be fully coupled as a single large system of equations that solve for all unknowns and couplings between them at once in a single iteration [86]. To compensate for this expense, the default PARADISO (parallel sparse direct solver) solver is to be used, which solves via an unsymmetric sparse matrix to utilise less memory when storing elements during solving, as the majority of elements are zero. However, the linear solver is direct, which is more robust but uses more memory as it scales usage at $N^{1.5}$-N^{2} where N is the number of degrees of freedom in the model – the default memory allocation factor of 1.2 was used. Iterative solvers scale with N so require less computational capacity but are less robust if the mesh quality is low or includes deformation of slender geometries [86], which is employed here when compressing vessel structures so was less applicable for use in the model.

The initial aspect of the model to be built is the deformation of the spinal cord that will represent the chronic compression seen in NT-SCI. Relative to the solid mechanics mathematical models presented in chapter 2, deformable mechanics is built into the numerical application (chapter 3.3).

3.3 Solid deformation

As means of simulating non-traumatic spinal cord injury, deformable mechanics of spinal cord tissue has to be implemented into the finite element model. Non-traumatic injury is understood as chronic, low-level compression and this work aims to understand the development of this injury at a mild, sub-

clinical level. Solid deformations are to be applied externally on the exterior surface of the spinal cord to deform the underlying blood vessels, microvasculature and spinal cord matters.

3.2.1 Displacement

In deforming the spinal tissue, the effect of applying an external load was initially investigated. This initial solid model included the geometries of the arterial vessel walls and the internal artery fluid, which were both defined as solids with linear elastic properties of the white matter (section 1.5.2). Boundary loads were attempted initially at the anteroposterior face of the spinal cord but at loads that caused >10% deformation, the tissue would buckle and the model would fail, due to the inversion of nodes on buckling, causing extreme solver divergence (Table 12).

Table 12: Load-displacement profile of linear elastic spinal cord and artery structures.

Load (N/mm^2)	Vessel displacement (mm)	Cord displacement (mm)
25	0.12	0.02
50	0.14	0.04
250	0.33	0.21

It was assumed this complication arose from the shape profile of the load and the stress-strain threshold of the linear tissue; previous spinal cord mechanics models report that non-linear material models are most suitable for increasing deformation loads. Automatic remeshing was employed here to re-mesh the geometry when the mesh quality fell below 0.5 but this did not aid model

convergence to a reliable solution. To overcome mesh at the deformation boundaries, defined displacement profiles were to be employed instead of loads.

Deformation of the ventral wall where the anterior spinal artery resides was the initial focus; the majority of non-traumatic injuries are effectual here due to protrusions of extrinsic bodies from the spine onto the cord [189]. A range of displacements reported as sub-clinical to clinical (from 0-30%) were investigated (Figure 8) [23], [26], [53], [190]. The displacement was applied across the whole cross-section of the cord using a moving mesh with a hyperelastic correction to replicate the initial hyperelastic tissue response of the spinal cord under load. The moving mesh is required to withstand such high deformations to move the material frame relative to the spatial frame.

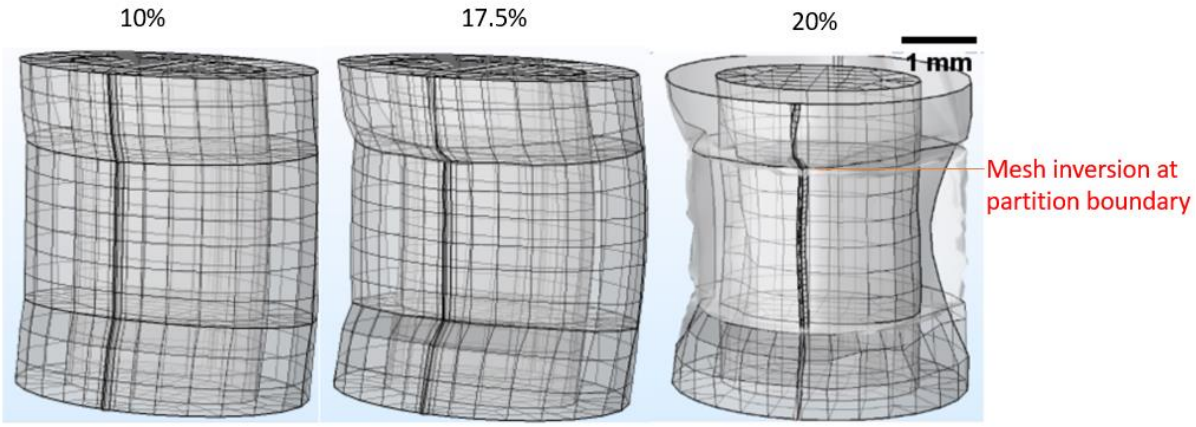

Figure 8: Mesh plots of prescribed displacement outcomes at 10% strain (a), 17.5% (b) and 20% (c) representative of mild, moderate and severe compression.

The mesh remains smooth and able to converge easily at lower strains, but at higher displacements, the mesh quality decreases. The partition and geometry-imposed boundaries resulted in mesh inversion and model failure. Displacement was applied in the y-direction (compressing the anterior face), with no constraints employed in the x-direction. Therefore, mesh inversions were common in the x-direction of the displacement.

In order to apply displacement at the appropriate anatomical location, smoothed functions were employed to define the deformation as a function of maximum displacement over a set of coordinates (Figure 9). A function was built to combine two smoothed step functions that act as smoothed approximations of a step within a controllable slope. This enables the transition from zero displacement up to its maximum displacement at a particular location or coordinate.

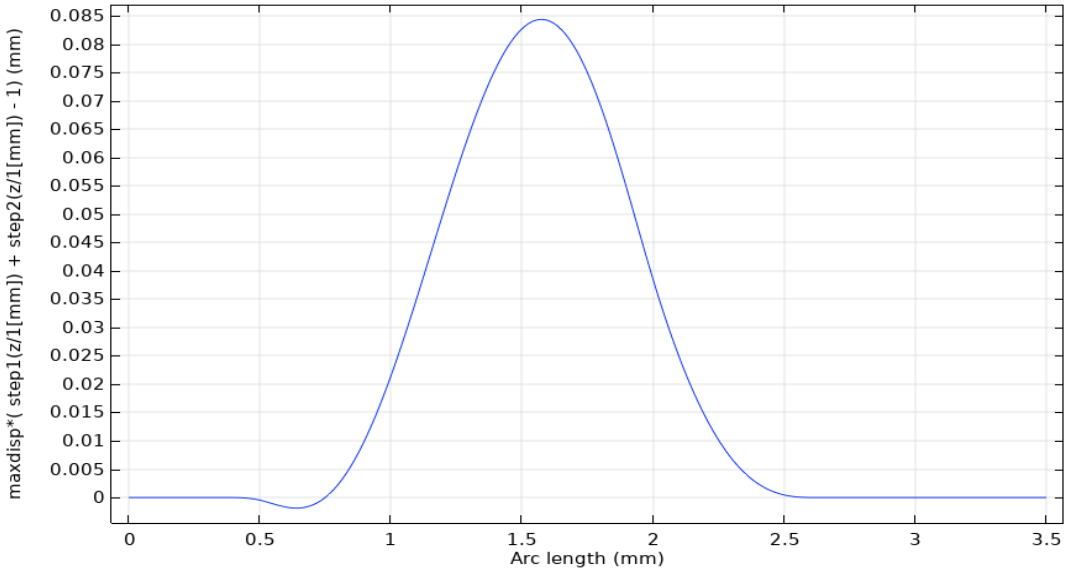

Figure 9: Displacement function utilising smoothed step functions to produce the bell-curve deformation.

The arc length was relative to the height (z-coordinate) of the spinal cord and the maximum displacement was a percentage of the sagittal cross-section deformation (e.g., 0.285mm=10% strain). The creation of a bell-curve deformation step was to be representative of a protrusion deforming the cord with maximum force and velocity at its apex and decreasing further from the peak area of contact. The smoothing of the deformation profile using the step function maintained a higher quality and integrity of the mesh, as defined by a decrease in skewness of the local elements at the boundary regions (Figure 10).

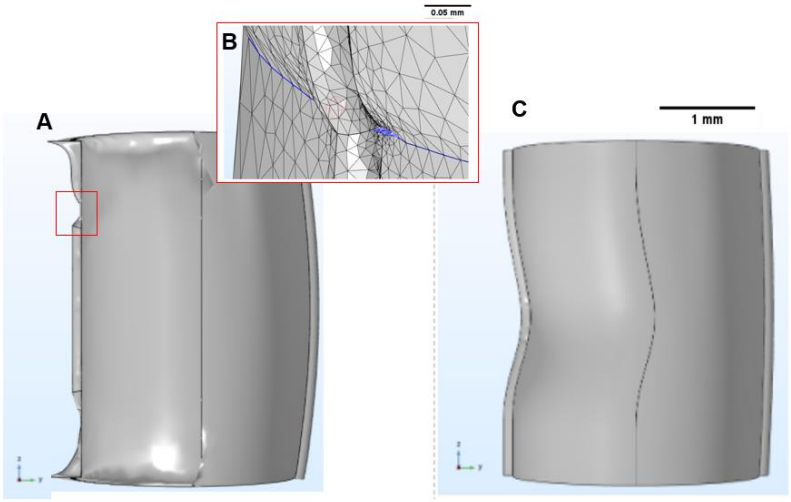

Figure 10: Implementation of the displacement step function. Harsh local deformations are seen prior to the smoothing step function (a), particularly inversion of sharp edge elements (b). The smoothing function prevented mesh inversions (c).

Dependent on the positioning and severity of injury, parameters of the step function were altered to emulate focal and diffuse deformation profiles. Deformation was employed as a boundary condition defined using the following function:

$$maxdisp * (\left(xon\left(\frac{x}{1[mm]}\right) + xoff\left(\frac{x}{1[mm]}\right) - 1\right) * (zon\left(\frac{z}{1[mm]}\right) + zoff\left(\frac{z}{1[mm]}\right) - 1)) \quad [21]$$

For anterior injury simulation, maximum displacement (maxdisp) was the height of the deformation arc from zero to its apex (i.e., defined as 0-30% of the cord sagittal diameter). The x- and z-coordinates allowed for precision of displacement along the coronal and sagittal planes, respectively. The above function was employed in the y-direction to employ displacement on the anterior face of the cord and was altered accordingly for injury at different locations, namely posterior (-y direction) and anteroposterior (x-direction). The smoothing function prevented harsh step zones of displacement and subsequently increased the quality of the mesh (Figure 11).

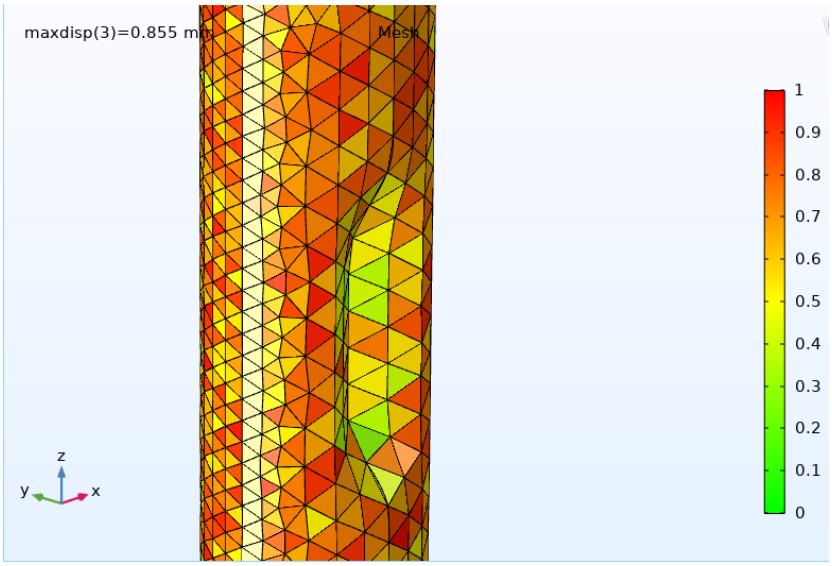

Figure 11: Mesh quality (in terms of skewness) after smoothing of the step. Relative to scale, 0=worst quality and 1=best quality.

Skewness is a measure of mesh quality wherein the equiangular skew of the angles of element edges is compared to the angles in an ideal element – some skewed elements are still visible in the injury epicentre, but the boundary elements were of a high quality.

NT-SCI via chronic compressive means (cervical spondylitic myelopathy, ligament ossification, disc herniation) has generally been defined as becoming symptomatic at a spinal canal diameter reduction of 30%; ideally, the model would simulate up to this strain threshold to elucidate the threshold in which the fluid mechanics assume an ischemic and potentially hypoxic environment, but the model was limited to sub-clinical (<10%) compressions when coupled to fluid and oxygen dynamics via a fluid-structure interaction (chapter 3.4 and 3.5). The moving mesh required for severe deformations of the solid up to 30% caused over-constraint when a second moving mesh was required to map the fluid domain in the FSI setup (section 3.6). Development of injury during the early stages of mild non-traumatic compression was therefore modelled here as incremental increases in strain by 2.5%, ranging from 0% to 10%. On completion of the deformable mechanics implementation, the blood flow models were to be included.

3.4 Coupling arterial and microvasculature flows

A primary focus of this work has been determining the appropriate governing equations and boundary conditions required to simulate the complexity of the vascular network in the spinal cord. As detailed in chapter 2, a porous medium

is to be implemented to represent the complexity of the intrinsic microvasculature as a continuum model coupled to free-flow arteries. This section assesses the sensitivity of model parameters, namely artery geometry positionings (external or internal to the cord, longitudinally parallel to fibres or traversing inwards), porous medium material properties (porosity and permeability) and the physics used to solve the mathematical model (Darcy or Brinkman's flow).

3.4.1 Geometry effects on blood flow

Multiple geometries were investigated to determine the appropriate geometry representation required to accurately reflect NT-SCI, without unnecessary anatomical detail (Table 13). Differences in the shape of the grey matter (ellipse, x-shaped and physiologically shaped) were trialled to understand how the boundary of the geometry shape affected the mesh density and therefore convergence of the model. Positions of the cord vasculature were trialled as extrinsic (physiologically-representative) and intrinsic (simpler model convergence) to determine which was most accurate for representation of blood flow.

Table 13: Geometry implementations and outcomes.

Geometry	Affect	Outcome
X-shaped grey matter to emulate butterfly shape	Model was prone to mesh inversions	Ellipse semi-circle used
Arterioles modelled branch from the ASA into tissue	Mesh was prone to inversions and arterioles did not significantly increase blood flow	Arterioles were neglected from the model
Arteries modelled transversely coursing into tissue like the vasocorona	Only representative of the vasocorona and not the core arteries	Longitudinal arteries representing the ASA and PSA were employed
Posterior spinal vein added	Added to drive microvascular flows through tissue to an outlet	Implemented in the model for use as a model outlet

In the initial x-shaped model, permeability was isotropic throughout the tissue (with no differentiation between white and x-shaped grey matter). Only one central artery was deployed to understand the influence on porous flow. An initial pressure condition of 630Pa was set, relative to the known pressure of cerebrospinal fluid in the T10 segment of a rat (from a sham, unoperated group), assumed as representative of pressures in the perivascular interstitium [191]. No or low (up to 400Pa) initial pressure conditions resulted in negligible flow in the cord tissue, with an erratic flow distribution through the pores (Figure 12). It was assumed the model was under-constrained due to extremely low velocity outputs that were dependent on the imposed initial pressure condition, which should only function as an output approximation for the solver.

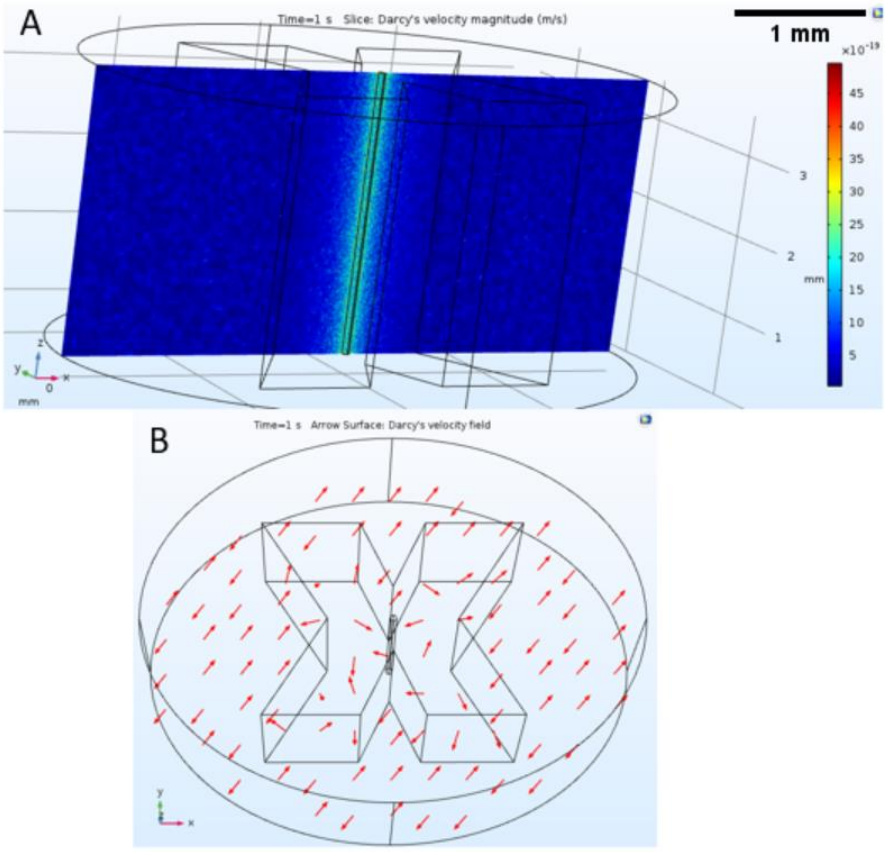

Figure 12: Darcy flow distribution in absence of viscous flow laws. Slice plot is in the centre of the cord (y=0) with a velocity contour range of 0-$\times 10^{-19}$mm/s (a), Darcy velocity distribution is evenly spread throughout tissue (red logarithmic-scaled arrow vectors) (b).

Pressure-driven flow can be seen exiting the central artery into the porous medium, but at extremely slow velocities (~$\times 10^{-19}$ mm/s) and in erratic directions. Presence of a central artery was useful for determining internal flow behaviours but was unrepresentative of the cord vasculature itself.

Therefore, additional free-flowing sources were employed at the posterior end of the cord, plus additional anterior arterioles, to protrude into the spinal medium as additional constraints for the intrinsic porous pressure gradients. It was hypothesized that additional source flows would provide more pressure

output conditions for the porous Darcy pressure gradients, instead of one central artery to feed the whole cord, which is physiologically unrepresentative. Addition of a second source vessel and arteriole at the posterior end of the cord increased the Darcy velocity magnitude by 100-fold. However, when under mild compression (2.5% reduction in sagittal diameter), the 100-fold in velocity magnitude was almost completely reversed. The jump in these outputs seemed refutable and unreliable: despite the addition of anterior and posterior intrinsic arterioles, Darcy velocity was still extremely slow when compared to the expected capillary velocity of 0.56mm/s [172]. It was assumed addition of a posterior vessel was additive due to additional pressure gradients now evenly distributed at both ends of the tissue, compared to sole addition of an arteriole which only affected the surrounding anterior tissue. The almost complete negation of the added PSA velocity when under mild strain was not expected – this would infer complete occlusion and redundancy of the vessel, but again highlights the sensitivity of the model to feeder vessel pressure gradients. Additionally, Darcy velocity vectors lacked consistency or direction through the tissue due to a lack of constraints in the fluid model. An assumption was made that the added geometric complexity of arteriole in-shoots was not required due to the negligible change in flow in their absence. However, the addition of a second artery was influential and assumed representative of the two posterior arteries that feed the thoracic section of the spinal cord, so the two posterior spinal arteries were confirmed as an inclusion criterion.

The posterior spinal vein was added to act as an outlet to direct flow through the tissue aside from the top and bottom of the cord. The anterior and posterior

arteries and posterior vein were positioned to run longitudinally in the z-direction on opposite sides of the cord to direct intrinsic flow behaviours. The resultant velocities were a more appropriate scale (~$\times 10^{-9}$ mm/s) in the artery-vein model but were still very low. The direction of flow was more appropriate but the insufficient flow rates were assumed as due to insufficient pressure constraints and a lack of intrinsic porous flow governance via means of other parameters, such as porous material properties and distinction between the grey and white matter. The geometry was doubled in height to extend the hydrodynamic entry length and ascertain if the vessel-driven gradients were underestimating the average intrinsic Darcy velocities – increased vessel length did not alter the velocity speeds close to the extremities or in the centre. It was therefore assumed the required geometries to create sufficient tissue velocities were implemented, which were in line with the literature. Inclusion criteria comprises of differentiated grey and white matter, the anterior spinal artery, two posterior spinal arteries and the posterior spinal vein. However, microvascular flow behaviour through the spinal tissue still requires optimisation.

3.4.2 Effect of porous material properties

Initial model iterations focused on free flow geometrically positioned within, or next to, a porous medium governed by Darcy's law. By co-locating and not coupling arterial free flow to porous microvascular Darcy flow, only pressure gradients were effectual in determining porous velocities. However, these

models are computationally inexpensive and therefore were used to inform material properties and appropriate physics.

It is well understood that the grey and white matter of the spinal cord have different material properties. During geometry inclusion analysis (section 3.4.1), an isotropic permeability had been employed with no discernment between the spinal tissue matters. Therefore, porous material properties were to be investigated to ascertain the appropriate properties that represent microvascular behaviour.

Porosities and permeabilities of white and grey matter differentiate due to difference in the tissue structures [180]. White matter is known to have an anisotropic permeability due to the structuring of fibre tracts, whereas grey matter has an isotropic permeability due to the strict ordering of cell bodies [180]. Average porosities of 0.4-0.45 for the spinal cord matters have been reported [180], meanwhile *in vivo* rodent models of spinal cord ischemia have cited the extracellular space fraction (porosity) of the dorsal horn grey matter as 0.2 when at a blood pressure of 80-110mmHg, decreasing to 0.16 on a decrease of blood pressure to 50-60mmHg, and down to 0.02 under anoxic conditions of blood pressure at 20-30mmHg [181]. Other studies in the CNS identify similar porosities of 0.2, predominantly from brain grey matter studies [136].

Simulations were therefore run to test a range of porosity and permeability values relative to those reported in the literature for the brain and spinal cord. Values ranged from low (porosity = 0.1, permeability = $\times 10^{-17} m^2$), to average (porosity = 0.4, permeability = $\times 10^{-13} m^2$) and high (porosity = 1, permeability =

$\times 10^{-5} m^2$) to test the extremes of model sensitivity. In the Darcy flow model presented, altering porosity had a null effect on flow behaviour but permeability was greatly effectual when differentiating between white and grey matter properties, which influenced the route of blood flow. A difference in isotropic permeability between white and grey matter influenced the blood fluid path through the tissue which had the lowest resistance to flow (Figure 13).

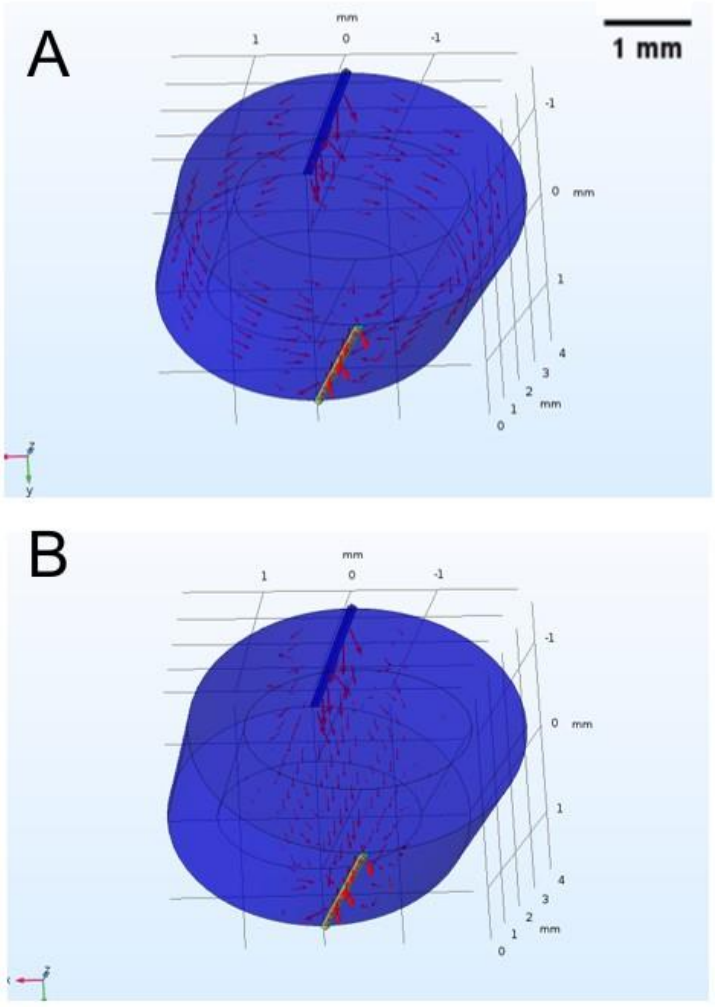

Figure 13: Planar extrinsic vessels force flow distribution evenly through length of tissue. Velocity arrow vectors (red) indicate an alteration in fluid path from the inlet to outlet at low (A) and high (B) resistances to flow in grey matter.

Next, anisotropic permeabilities were employed. White matter was defined with anisotropic permeability and grey matter as isotropic. Flow was distributed into the white matter irrespective of geometry. It was assumed the anisotropy created a less tortuous fluid path by allowing free movement in the z-direction, parallel to the free fluid pressure gradients, whereas the isotropic grey matter increased fluid path lengths due to compact ordering of the porous solid structure. It has previously been argued that anisotropic fibres compact together when compressed, reducing the extracellular space [51],[192], meanwhile isotropic properties re-route blood flow around the compact material [136]. Flow behaviour in the individual tissue types was simulated with a focus on changing the permeability in grey matter (Figure 14) where vasculature is most dense and NT-SCI damage is known to be most effectual.

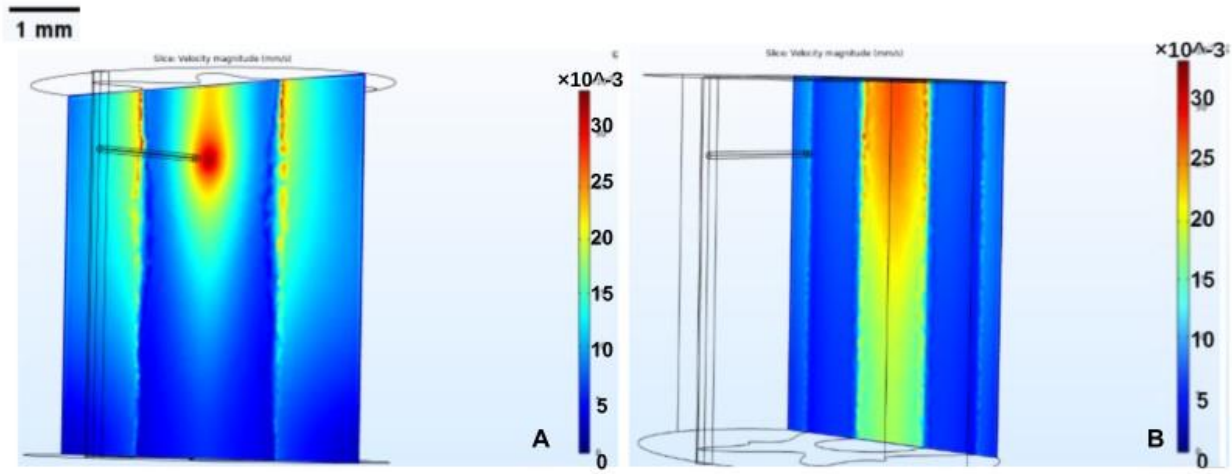

Figure 14: Distribution of flow through high and low permeabilities of grey matter. The extremes of the permeability range as high (a) and low (b) resistance to flow - when applied only to the grey matter - showed pronounced changes at planes central through the cord.

Transitional flow zones between the white and grey matter displayed harsh boundaries. When resistance to flow was higher in grey matter (figure 14a), flow was directed through the white matter. Conversely, low resistance in the grey matter streamlined flow through the isotropic grey matter (figure 14b). A range of resistances to flow were simulated to understand structure-driven changes to the fluid path, as in Table 14.

Table 14: Velocity magnitudes (mm/s) of spinal tissues compartments under variation of grey matter permeability.

Permeability of grey matter (m^2)	**Grey matter velocity magnitude (mm/s)**	**White matter velocity magnitude (mm/s)**
2×10^{-5}	0.15	0.154
2×10^{-10}	0.011	0.3
2×10^{-13}	2.64×10^{-5}	0.31

A number of biological models have defined matter permeability values at ~$\times10^{-13}m^2$ [177], [168]. However, these data complement some of the theories in terms of microvascular behaviour under injury; in assuming the grey matter has a higher resistance to flow due to compact fibres, the white matter compensates during compression due to its less dense structure. Below (Figure 15), an increased resistance to flow in the grey matter elicited faster flow through white matter, with pronounced effects under displacement (10%).

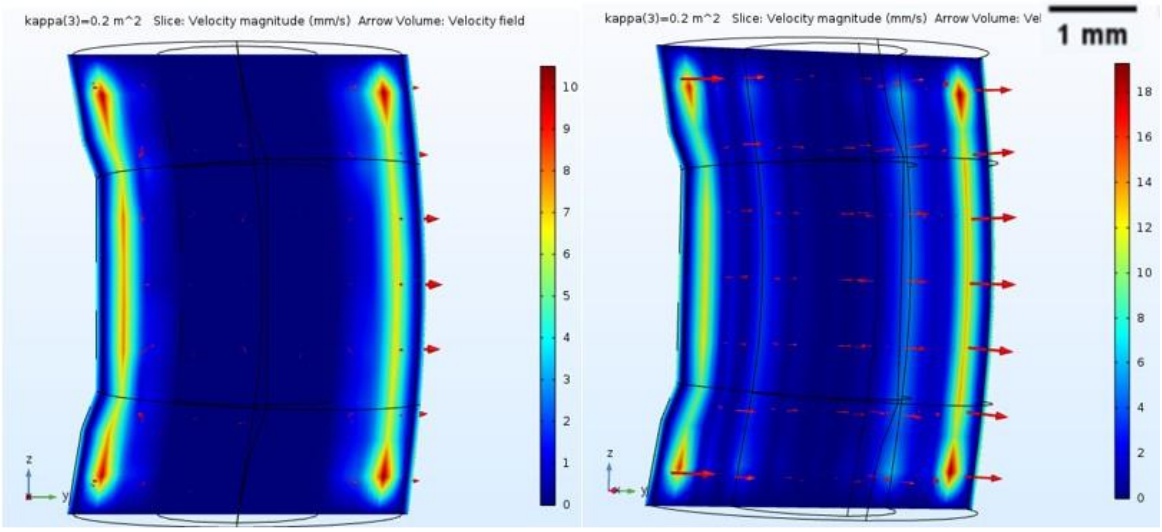

Figure 15: Slice plane of spinal tissue velocity magnitude (mm/s) under 10% deformation with high (a) and low (b) resistance to flow in the grey matter. Decreased resistance to flow is highlighted by larger velocity vectors (red arrows), coupled to presence of higher velocities at the white-grey matter boundary (light blue).

The increased velocities under compression were attributed to an increase in vessel pressures adjacent to the spinal tissue under strain, causing a compensatory increased velocity effect through the tissue. Large arrow vectors exiting the tissue into the vein are representative of heightened pressure gradients which compensate for the under-constrained pressure-driven model. From these studies, it appears permeability is a core determinant in intrinsic porous flow behaviour.

The literature-reported permeability values drive flow through the anisotropic white matter, which is physiologically representative of the vasocorona and its ingressing arterioles. However, the velocities remained too low despite the changes to the fluid model geometry sources and material properties. Therefore, the fluid physics was altered from free-Darcy to employ the

Brinkman equations which account for inertial effects in transitional free-to-porous flows [52] as means of increasing the average velocity of the spinal tissue to account for arterioles and dissipation of velocity as arteries decrease in size to arterioles and capillaries.

3.4.3 Brinkman's flow

Darcy's law does not account for the inertial transition between free-flowing sources and downstream porous flows as it derives average velocity from pressure gradients. Therefore, anatomy that is further from the arteries will have lower pressure gradients and lower velocities. It is known that grey matter has a higher density of microvessels and has a higher blood flow rate than white matter, so Darcy model behaviour assumptions do not fit with the current model requirements. Therefore, due to the unrepresentative velocities seen in section 3.4.2, the Brinkman equations model was employed to account for the inertial effects in transitional flows. This represents the presence of arterioles and vasculature between the explicitly modelled free-flow arteries and the intrinsic porous-continuum microvasculature.

Brinkman's flow is used to model single-phase flows; in this scenario, red blood cells are assumed as evenly and symmetrically distributed in the blood and non-Newtonian behaviour of the blood is also neglected. It is understood that single-phase representations of blood do not underestimate pressure or velocity changes when modelling stenosis of arteries when compared to multi-phase models [193]. On inclusion of the Brinkman equations, the primary

objective remained ascertaining the appropriate porosity and permeability values as inclusion criteria for the model.

Previous spinal cord models have employed isotropic permeability as those models primarily investigate other effects such as traumatic injuries (e.g. burst fractures [76–84]) and non-traumatic conditions (e.g. syringomyelia [96], [97], [152]) or because the local definition could not be derived experimentally or clinically.

In the context of the brain, porous vasculature models commonly employ a known permeability tensor across the whole tissue and have specific sink and source terms for individual vessel representation or have multi-compartment models representative of anatomies with varying permeability or behaviour [135], [175]. A previous brain model simulated a porous continuum model to investigate the changes to perfusion throughout the whole brain when one large intracranial blood vessel was occluded. The brain model included anisotropic permeabilities to account for variations in space, relative to those seen physiologically (i.e. arteriole-dense region, capillary-dense region) [182]. The specific behaviour of vessels within the brain regions was highlighted as imperative to include in understanding the true effects of occlusion; in whole organ models, one-dimensional network models are commonly prescribed for large vessels and multi-compartment porous continuum models for the respective arteriole or venule microvasculature, but the use of a one-dimensional network does not account for the transitional, mid-scale vasculature in the network [136]. Multi-compartment porous networks allow feeder vessels to correspond to their downstream receiving anatomies and

allow for assumptions around anatomy behaviours, such as the majority of oxygen exchange taking place in the capillary zones of spinal tissue.

Due to the nature of the simplified mathematical model presented here, the permeability of the arteries was not necessary to prescribe, as the continuation of volume output from the source-to-porous medium was inferred by the open fluid-tissue boundary and Brinkman equations. The paper assumed arteries acted as a unidirectional column flow, as depicted here through the imposed geometry and boundary conditions. As such, the pressure conditions at inlets were more applicable than identifying specific velocity thresholds at source fluid entry [174]. To avoid the need for volumetric geometry positioning for coupling that was employed in the whole brain model, models generally implement lumped parameters of fluid gradients weakly coupled to porous medium flux, as is to be employed here.

When replicated in the Brinkman model, equal low ($\kappa=2\times10^{-13}$ m^2) isotropic permeabilities in the white and grey matters directed a significant excess of flow into the white matter. In order to mitigate this, additional vessels were added to the ASA in the white matter to emulate the behaviour of the anterior sulcal arteriole (Figure 16). Scale ranges were magnified to look at velocity and concentration behaviours at the most relevant ranges for each.

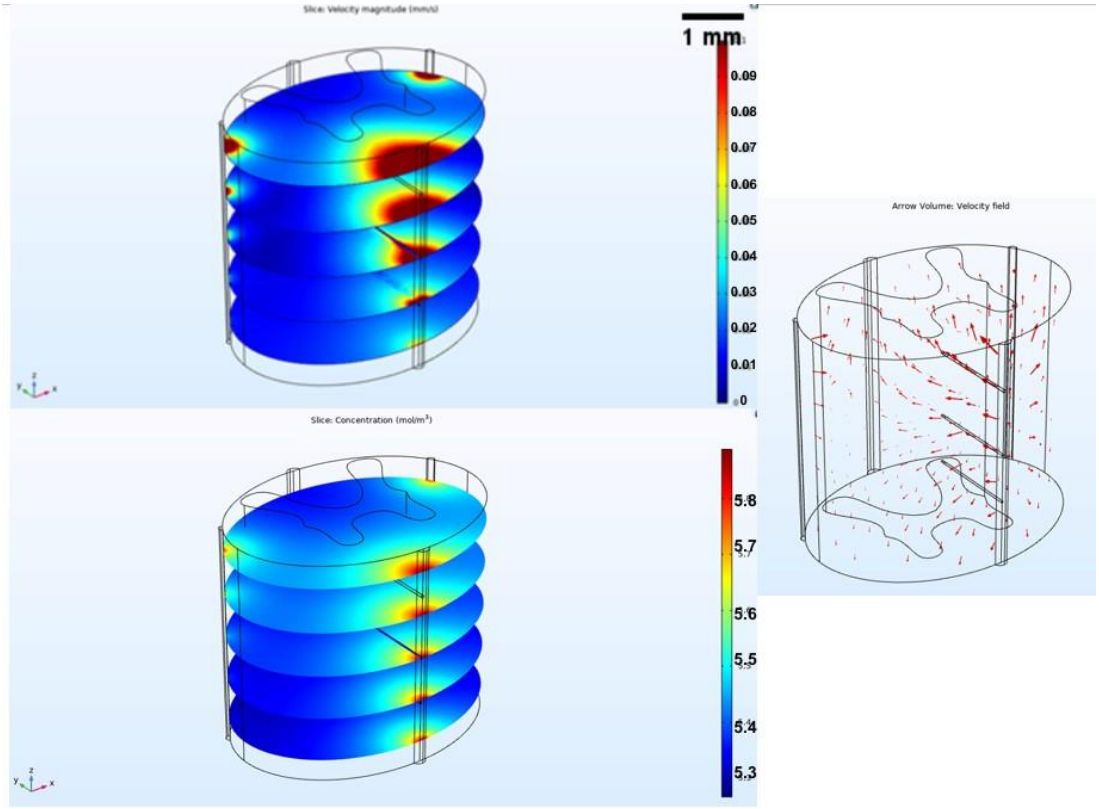

Figure 16: Uncompressed spinal cord with low isotropic permeabilities in both matter types. Contour plots of velocity magnitude (a), concentration (b) and velocity vectors (c) with isotropic permeability of $2\times10^{-13}m^2$.

As means of increasing flow rate into the grey matter from arteries, anisotropic permeability was implemented into both matter types. This directed blood into the white matter with the shortest fluid path, similar to the free-Darcy model (Figure 17).

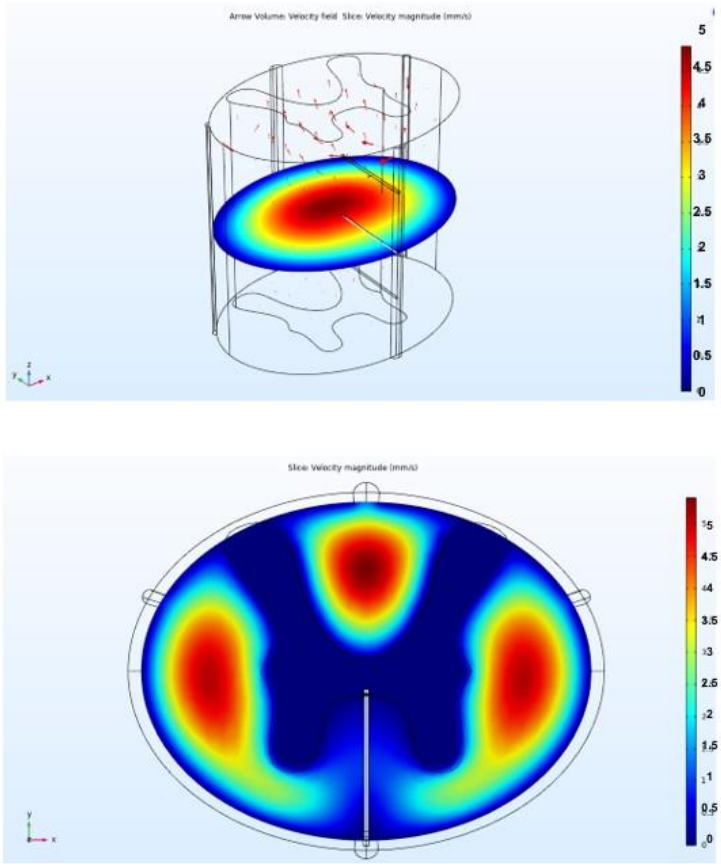

Figure 17: Blood flow behaviour when both spinal matters are anisotropic. Contour plot of anisotropic grey matter (a) and white matter (b). Scale range = 0-5mm/s.

Therefore, it was understood that the isotropy or anisotropy of the spinal tissue was the core driver of flow through the tissues. High permeability was employed in the grey matter ($2\times10^{-5}m^2$) and lower in the white matter ($2\times10^{-8}m^{2)}$, both as isotropic permeabilities relative to the increased flow rate into the grey matter seen in section 3.4.2 when both tissues were isotropic (Figure 18).

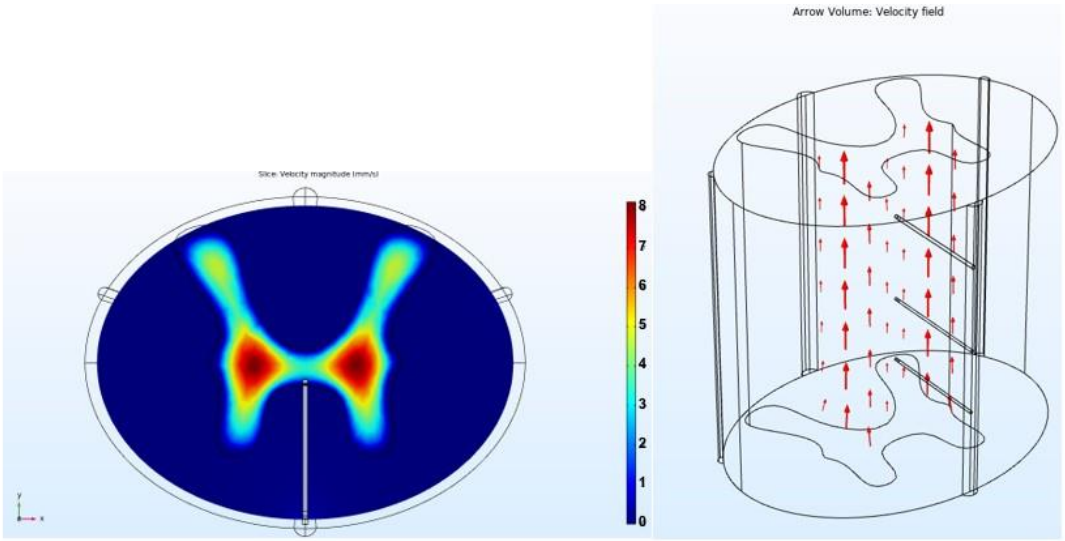

Figure 18: Contour (a) and velocity vector (b) plots of spinal cord blood velocity with high isotropic tissue permeability in grey matter and lower in white matter.

This scenario output velocities in an appropriate range (Table 15), despite the re-directed flow behaviours.

Table 15: Velocity and concentration outputs for isotropic grey and white matters, with three sulcal arteriole inputs.

	Velocity (mm/s)	**Concentration (mol/m^3)**
Grey matter	0.78	5.03
White matter	0.023	5.12
ASA [z]	69.67	5.79
PLA [z]	13.29	5.39
Branch 1 (z=2.75)	3.5	5.35
Branch 2 (z=1.5)	0.72	5.28
Branch 3 (z=1)	0.19	5.24

The velocities were now in line with the expected outcomes but were rudimentary values that did not align with the literature. Analysis of both parameters was run to assess the behaviour of both tissues in terms of porosity, permeability and isotropy relative to known material properties from the literature (Table 16).

White matter		Grey matter			
Porosity	**Permeability (m^2)**	**Porosity**	**Permeability (m^2)**	**WM velocity magnitude (mm/s)**	**GM velocity magnitude (mm/s)**
0.2 [153], [194]	5×10^{-14} m^2 x/y-direction 2.5×10^{-13} m^2 z-direction *Anisotropic* [180]	0.45 [180]	3.3×10^{-14} m^2	0.0089	0.0043
0.2	4.28×10^{-4} mm^3 *Isotropic* [182]	0.45	3.3×10^{-14} m^2	0.037	0.005
0.2	5×10^{-14} m^2 x/y-direction 2.5×10^{-13} m^2 z-direction	0.25 [180]	$1.234mm^3$	0.0071	0.12
0.2	4.28×10^{-4} mm^3	0.25	$1.234mm^3$	0.032	0.49
0.2	5×10^{-14} m^2 x/y-direction 2.5×10^{-13} m^2 z-direction	0.25	3.3×10^{-14} m^2	0.0088	0.0043
0.2	4.28×10^{-4} mm^3	0.25	3.3×10^{-14} m^2	0.037	0.005
0.2	5×10^{-14} m^2 x/y-direction 2.5×10^{-13} m^2 z-direction	0.45	$1.234mm^3$	0.007	0.13
0.2	4.28×10^{-4} m^3	0.45	$1.234mm^3$	0.032	0.46

0.4 [180]	5×10^{-14} m^2 x/y-direction 2.5×10^{-13} m^2 z-direction	0.25	1.234mm^3	0.0071	0.12
0.4	4.28×10^{-4} mm^3	0.25	1.234mm^3	0.0325	0.51
0.4	5×10^{-14} m^2 x/y-direction 2.5×10^{-13} m^2 z-direction	0.45	3.3×10^{-14} m^2	0.0089	0.004
0.4	4.28×10^{-4} mm^3	0.45	3.3×10^{-14} m^2	0.037	0.005
0.4	5×10^{-14} m^2 x/y-direction 2.5×10^{-13} m^2 z-direction	0.25	3.3×10^{-14} m^2	0.004	0.004
0.4	4.28×10^{-4} mm^3	0.25	3.3×10^{-14} m^2	0.037	0.0053
0.4	5×10^{-14} m^2 x/y-direction 2.5×10^{-13} m^2 z-direction	0.45	1.234mm^3	0.007	0.13
0.4	4.28×10^{-4} mm^3	0.45	1.234mm^3	0.032	0.455

Table 16: Analysis of porous material properties on blood velocities through the spinal matter types when implementing the Brinkman flow model. The highlighted rows indicate the material parameters chosen for future model iterations.

Relative to the above data, the shaded rows indicate the material parameters that produced the expected average velocity magnitude for the tissue volume. The data highlights that porosity is not hugely influential on fluid behaviour and that permeability is a core driver of flow. Lower resistances to flow in both tissues were required to represent microvascular behaviour at the appropriate scale. Therefore, the isotropic permeabilities employed were derived from a brain model study and porosity values from a study in the spinal cord, as in Table 6 in section 2.4.1. The assumption implemented here was based on the grey matter being a vascular-dense tissue, therefore defined with the arterial system permeability from the brain model to produce higher blood flow rates (κ=1.234mm^3). The white matter was defined with capillary system permeability from the brain model (κ=4.28×10-4mm^3), as its vasculature is generally sparser and is governed by branching arterioles from the vasocorona. Porosity was defined relative to the extracellular volume fraction defined in the dorsal horn grey matter of the rat spinal cord under normal conditions (ε=0.25) [181], [153] and that of the known porosity for spinal cord white matter (ε=0.4) [180].

Anisotropy of the white matter is therefore not accounted for in this model as it did not output the expected velocities and was therefore excluded from the model criteria. Anisotropic permeability is reported to overly skew flow distribution in poroelastic models of vasculature, including in injury scenarios [137]. The influence of this is likely driven by coupling an inherent preference for blood flow path to tissue ability to alter its pore shape in a poroelastic model. This was inferred here when anisotropic white matter was paired with low resistance to flow in the grey matter, the velocities in grey matter remain below

what would be expected, despite a higher pore volume fraction in the grey matter. This was assumed as due to reduced flows from the arteries through white matter into the grey matter. Prior literature values at the scale of ~×10^{-13} m^2 therefore are unlikely to represent the vasculature and may predominantly account for the extracellular fluid space that governs interstitial fluid and cerebrospinal fluid.

On surmising the appropriate fluid models to achieve the required baseline velocities in each tissue type, oxygen transport is to be coupled to the blood flow model to fully understand tissue response to ischemia.

3.5 Oxygen transport

When modelling both fluid mechanics models (Darcy only 3.4.1-2 and Brinkman 3.4.3), oxygen transport was modelled concurrently. Convection of oxygen within blood was coupled to blood velocity outputs and diffusion of oxygen was attributed an effective diffusivity and dispersion model for movement through the porous tissue. The oxygen source was defined at artery inlets and outlets were assigned at vessel outlets, the posterior vein and at the top and bottom of the cord to emulate circulation into other segments.

Primary objectives of this model were to elucidate the appropriate inflow concentration boundary conditions and how to define the oxygen consumption model. As an initial test, a Krogh cylinder model (oxygen source vessel running centre down the tissue) was developed to test the diffusion model setup. The Krogh tissue cylinder model is a simplified model of oxygen change in muscle

tissue, emulating immediate oxygen exchange into surrounding tissue from a single, central blood vessel. The Krogh model assumes a steady state, radial symmetry of a cylindrical capillary, continuous distribution of reaction and no radial flux when the vessel is the sole oxygen supplier of the surrounding tissue (Figure 19). The model was employed with a constant consumption term in the white and grey matter, These models are generally applied to modelling of muscular vasculature, due to the structural regularity of muscle fibres and requirements for oxygen: this is not akin to the spinal cord vasculature as vessel positioning is irregular through the cord but it has also been employed in previous brain oxygen models for simplicity [172].

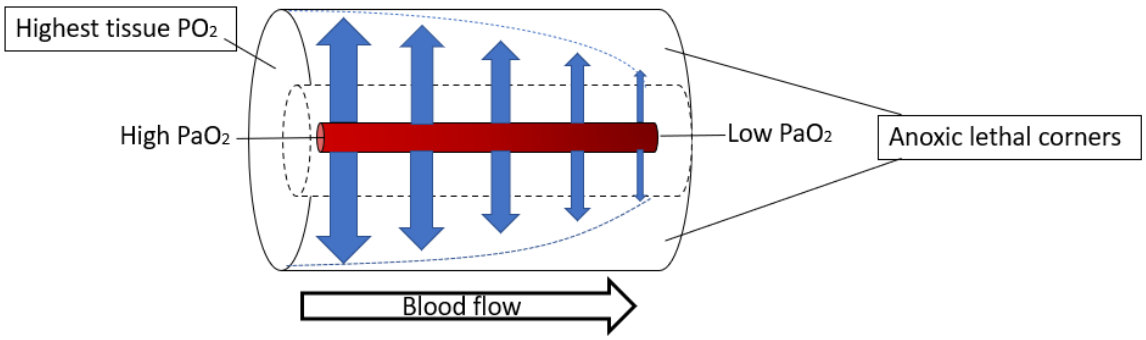

Figure 19: The Krogh cylinder model of oxygen transport from a capillary into surrounding tissue. Oxygen concentration decreases with longitudinal progression down the capillary as the fluid pressure also decreases, hence the surrounding tissue experiences a correlated decrease in oxygen.

The Krogh cylinder model is therefore a simplified means of quantifying oxygen transport and was implemented to understand gross qualitative changes, namely when iterating boundary conditions.

In the free-Darcy model, initial oxygen concentrations were 0.07mol/m^3 for grey matter, 0.029mol/m^3 for white matter and 0.38mol/m^3 within the Krogh cylinder vessel, which were too low compared to literature-reported values. Therefore, the boundary conditions were assumed to be under-constrained as a downstream effect of the fluid model and it was assumed that the constant consumption rate was too high. Time-dependent simulations were run to determine if oxygen was not progressing through the tissue due to a lack of constraints, or if the consumption expression was incorrect. Progression of oxygen down the vessel and into the porous tissue was visible in time-dependent simulations (Figure 20).

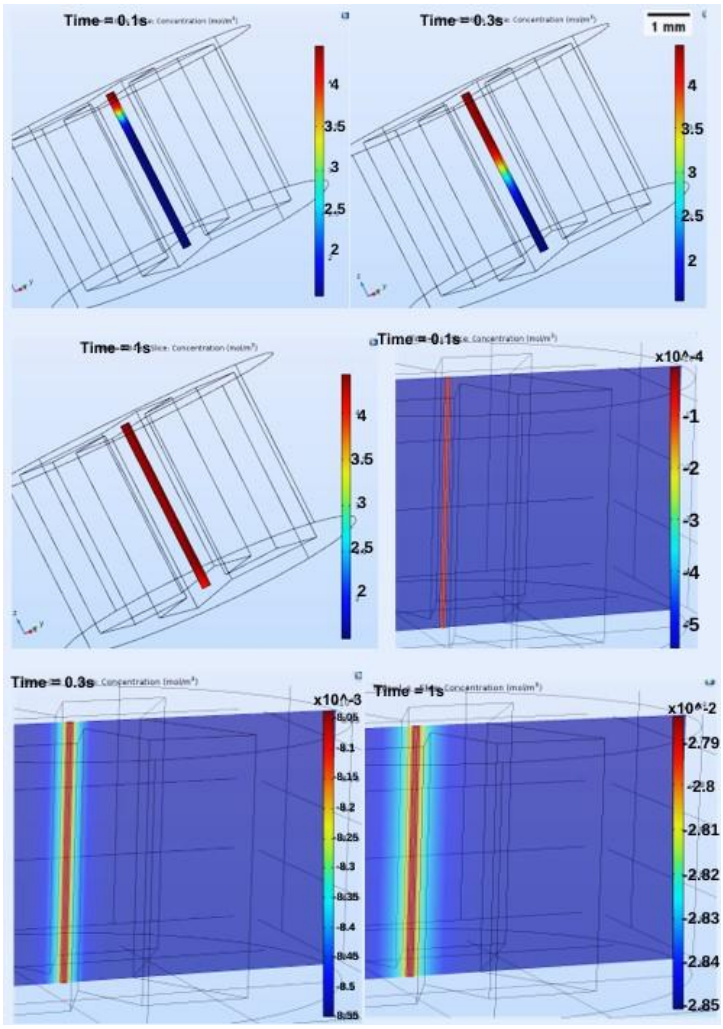

Figure 20: Oxygen distribution through the spinal cord over 1-second time period. Spread of oxygen over time is present when solving only for vessel concentration (a-c) and for vessel diffusive spread into the tissue (d-f). Movement of oxygen species outward into tissue (d-f) increases with time (d=0s, e=0.3s, f=1s).

Oxygen was seen progressing with time into the porous medium until it reached the maximum consumption level, affirming excess consumption by the sink model. In order to combat this, the source oxygen concentration setup was altered to be defined by pointwise constraints of a set concentration at the inlet boundary, whereas a previously employed flux condition based the inlet

concentration on velocity at entry, which forced dependency on the inadequate free-Darcy fluid behaviour (Figure 21).

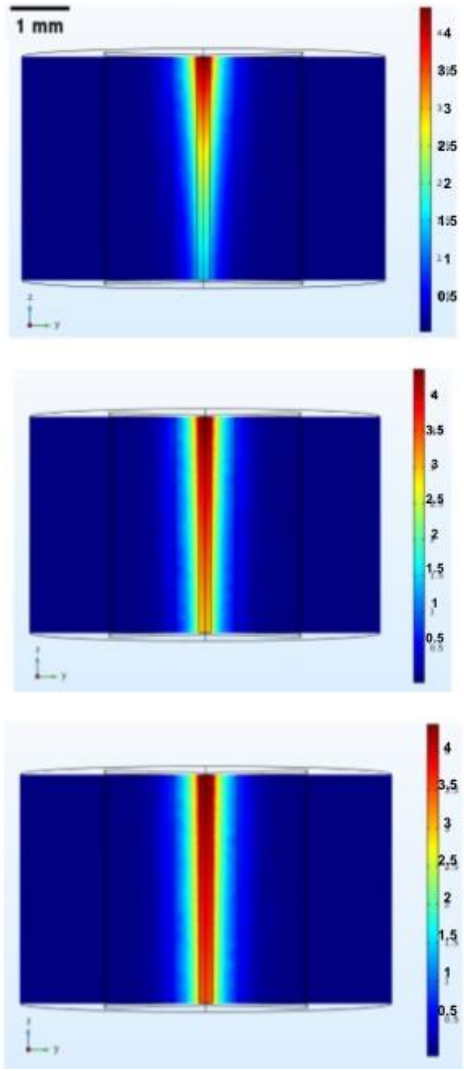

Figure 21: Increasing pressure-driven diffusion gradients display further diffusion of oxygen. Inflow pressure is increased by 3-fold (b) and 5-fold (c) with newly employed pointwise concentration inflow conditions.

In defining the source oxygen concentration as pointwise and enforcing the same boundary pressure constraints on the Darcy tissue as the free-flowing artery, the concentration gradient in the tissue fulfilled the initial oxygen

condition as the expected tissue average of 0.5-0.7mol/m^3. However, these edits had taken place in line with the previous Darcy model where velocities had remained too low and the final material properties for use had not been elucidated yet.

Variations in permeability were investigated in the Krogh cylinder model to ascertain the appropriate material properties for sufficient oxygen exchange. A range of permeability values were studied, wherein spread of oxygen was limited or free to move due relative to the resistance to fluid flow (Figure 22).

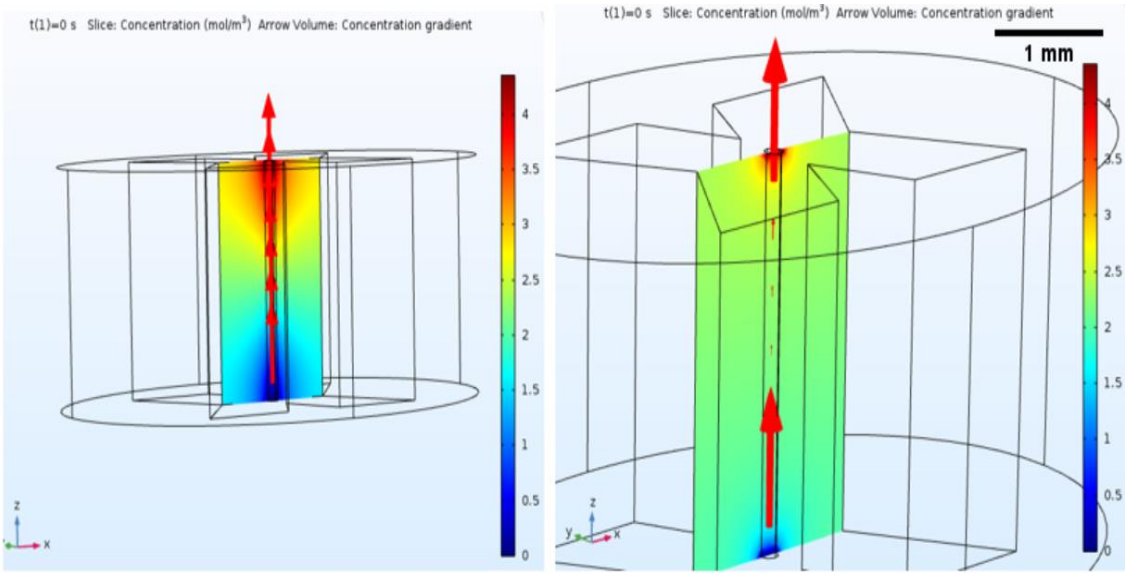

Figure 22: Oxygen diffusion profiles through grey matter at high and low permeabilities. Concentration gradients at extreme permeability and porosity gradients of permeability=0m^2 and porosity=0.0001 (a) and permeability=50m^2 and porosity=1 (b).

The general transport trends were as expected; spread of oxygen through tissue was seen in scenarios with low resistance to flow, meanwhile transport was limited under high resistance to flow which was therefore governed by

sharp pressure gradient changes at the vessel inlet and outlet boundaries (Figure 23).

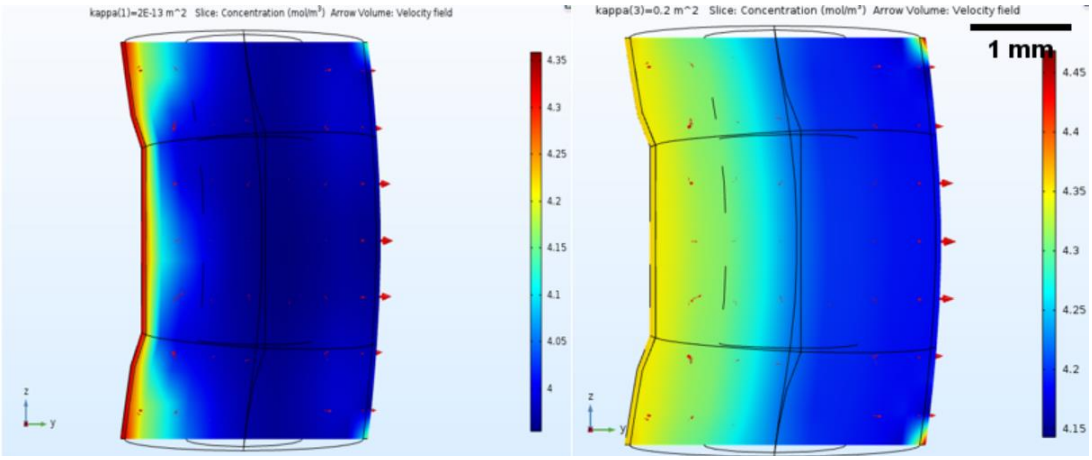

Figure 23: Diffusive spread relative to high and low permeability in both spinal tissue types. Low resistance to flow (b) increases the spread of oxygen, but is still limiting in reach and diffusive capability, particularly in the case of high (b), literature-derived parameters.

The concentration outputs were considerably higher than the expected 0.5-0.7mol/m^3 range and did not vary dramatically between extreme material properties. The continued increase of oxygen in compressed regions with faster blood velocities highlighted an inefficiency with the sink function, which is investigated in section 3.5.1.

3.5.1 Consumption model

To account for venous structures and consumption of oxygen via capillary exchange in the spinal matter tissues, a sink model (equation 25) is assigned to react per unit volume of total pore space (Figure 24). The sink parameter is designated a consumption rate of -1.71μmol $cm^{-3}min^{-1}$, derived from the

estimated cerebral metabolic rate of rats. The rate was found from fitting changes in tissue partial pressure of oxygen (PO_2) up to 200μm from cortical penetrating arterioles into the Krogh cylinder model of diffusion [195]. It is known that the grey matter has a consumption rate of approximately three-fold in the brain, but the consumption term is employed as an average of the whole tissue - the oxygen extraction rate of the vessel-dense grey matter is assumed as represented by the matter material properties and respective blood flow and oxygen concentrations. The sink parameter is multiplied by a ramp function which means the rate is fully switched on at the tissue's highest concentration:

sink*(rm2(c/1[mol/(m^3)])-1 [22]

The model was devised to maintain an average of oxygen in the tissue by consuming continuously when concentration remained above the minimum threshold (zero). The sink function will consume at its maximum when the spinal cord tissue concentration is at its average for the two tissues (c=~0.6mol/m^3) (Figure 24).

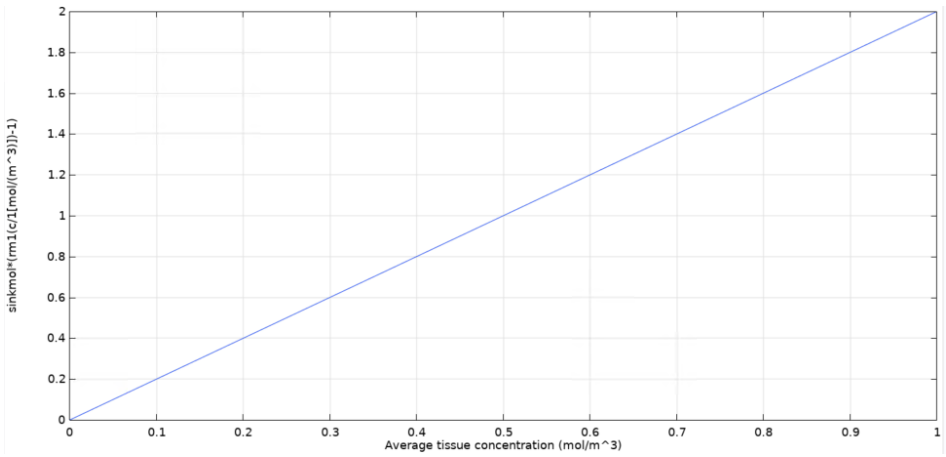

Figure 24: Plot of oxygen consumption rate as a function of tissue oxygen concentration.

The sink model reaches the maximum consumption rate when the tissue concentration is equivalent to the specified concentration of artery oxygen influx (i.e., the maximum possible before transport into neighbouring tissues). The tissue is expected to not reach this maximum was due to the dissipation of blood and oxygen through the Brinkman model - it is known that the rate of oxygen consumption is usually 80-85% of its maximum value [172]. However, in order to maintain tissue concentration under ischemic conditions, the ramp function of the sink model enabled an increase in oxygen consumption if the system was receiving less provided less blood flow and therefore oxygen, but also meant the concentration could not go below zero.

As before, the sensitivity of the porous material parameters for the model were investigated to ascertain the appropriate parameters for inclusion (Table 17).

White matter		Grey matter			
Porosity	**Permeability (m^2)**	**Porosity**	**Permeability (m^2)**	**WM concentration (mol/m^3)**	**GM concentration (mol/m^3)**
0.2 [153], [194]	5×10^{-14} m^2 x/y-direction 2.5×10^{-13} m^2 z-direction *Anisotropic* [180]	0.45 [180]	3.3×10^{-14} m^2	0.6	0.54
0.2	4.28×10^{-4} mm^3 *Isotropic* [182]	0.45	3.3×10^{-14} m^2	0.65	0.55
0.2	5×10^{-14} m^2 x/y-direction 2.5×10^{-13} m^2 z-direction	0.25 [180]	$1.234mm^3$	0.63	0.54
0.2	4.28×10^{-4} mm^3	0.25	$1.234mm^3$	0.77	0.74
0.2	5×10^{-14} m^2 x/y-direction 2.5×10^{-13} m^2 z-direction	0.25	3.3×10^{-14} m^2	0.6	0.53
0.2	4.28×10^{-4} mm^3	0.25	3.3×10^{-14} m^2	0.66	0.53
0.2	5×10^{-14} m^2 x/y-direction 2.5×10^{-13} m^2 z-direction	0.45	$1.234mm^3$	0.63	0.55
0.2	4.28×10^{-4} m^3	0.45	$1.234mm^3$	0.78	0.74

0.4 [180]	5×10^{-14} m^2 x/y-direction 2.5×10^{-13} m^2 z-direction	0.25	1.234mm^3	0.63	0.55
0.4	4.28×10^{-4} mm^3	0.25	1.234mm^3	0.78	0.74
0.4	5×10^{-14} m^2 x/y-direction 2.5×10^{-13} m^2 z-direction	0.45	3.3×10^{-14} m^2	0.6	0.54
0.4	4.28×10^{-4} mm^3	0.45	3.3×10^{-14} m^2	0.66	0.55
0.4	5×10^{-14} m^2 x/y-direction 2.5×10^{-13} m^2 z-direction	0.25	3.3×10^{-14} m^2	0.53	0.53
0.4	4.28×10^{-4} mm^3	0.25	3.3×10^{-14} m^2	0.66	0.55
0.4	5×10^{-14} m^2 x/y-direction 2.5×10^{-13} m^2 z-direction	0.45	1.234mm^3	0.63	0.56
0.4	4.28×10^{-4} mm^3	0.45	1.234mm^3	0.77	0.74

Table 17: Analysis of porous material properties in the oxygen transport through spinal matter types. The highlighted rows indicate the material parameters chosen for future model iterations.

In agreement with the Brinkman flow data for spinal tissue blood velocities, the permeability and porosity factors highlighted above were included as inclusion criteria for moving forward. Similarly, lower anisotropic permeability of white matter reduced oxygen concentrations in both tissue types even when grey matter had low resistance to flow, agreeing that isotropic permeabilities are most suitable for implementation in the model.

On addition of the appropriate oxygen transport and consumption models, the solid, fluid and oxygen models had to be coupled to simulate the gross effect of NT-SCI on all aspects of the spinal tissue and its vascular network. Therefore, the fluid-structure interaction setup is to be investigated. In order to couple the multi-physics of oxygen consumption in blood flow, a reacting flow coupling is defined. This ensures coupling of the computed blood velocity to oxygen transport which is dependent on its behaviour and changes in composition. This would be more applicable if blood had been modelled with its non-Newtonian properties; convection is already driven by the velocity outputs of the model.

3.6 Fluid-structure interaction

A coupling condition was required to govern the relationship between the fluid and solid aspects of the model. The fluid-structure interaction was set up to couple the solid loading onto the free and therefore porous fluids.

3.6.1 Analysis of the fluid-structure coupling

To better understand the coupling required between the fluid-structures under deformation, a two-dimensional model was constructed to magnify visualisation when troubleshooting the meshes and conditions at the fluid-structure boundaries where the mesh was most prone to failure (Figure 25).

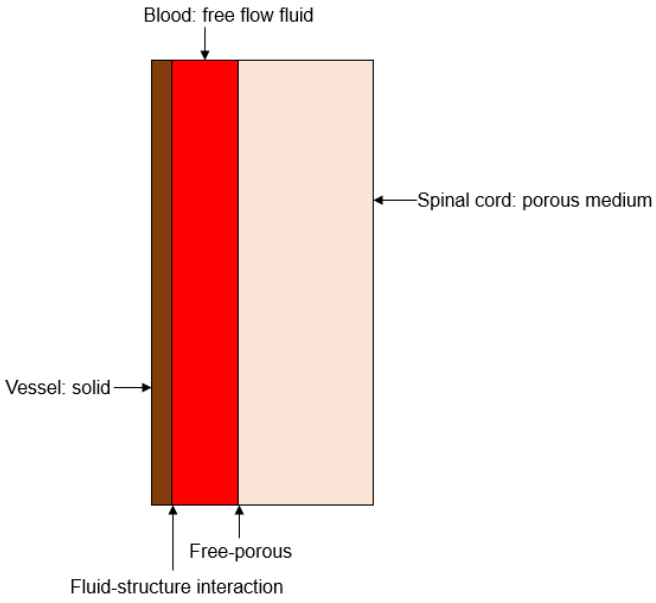

Figure 25: Boundary conditions of the two-dimensional model.

Initially, fluid-structure interactions and moving mesh deformations were defined at the same boundaries. The moving mesh was set to have fixed constraints at the top and bottom, with a default Yeoh correction stiffness of 10. However, the moving mesh prevented sufficient coupling of the material and spatial frames. The spatial domain would move relative to the moving mesh, but material domain would not (Figure 26).

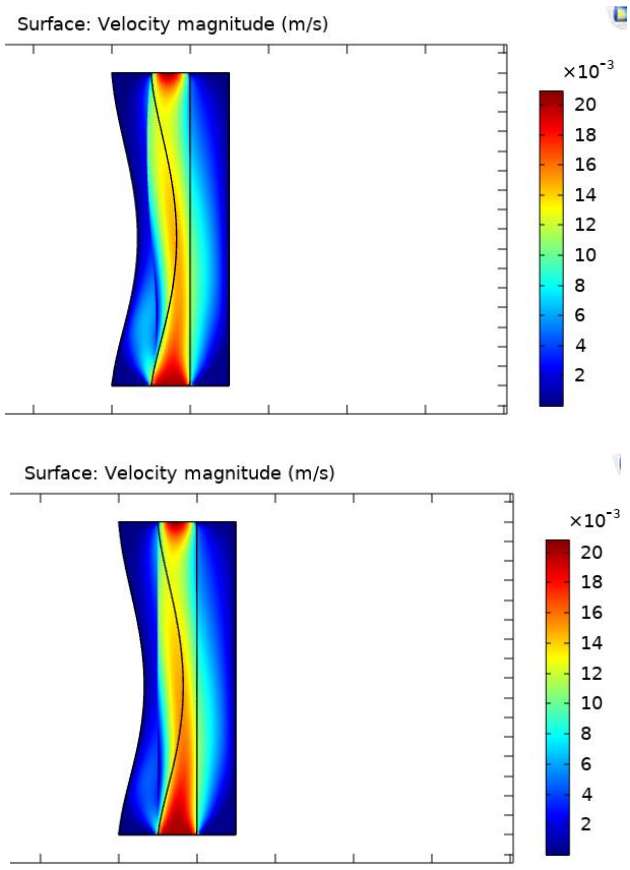

Figure 26: Uncoupled solid-fluid model frames. Initial FSI setup highlighted a change in solid model, which was not coupled to the fluid model in terms of the spatial domain and moving mesh.

It was deduced that the fluid-structure moving mesh had been over-constrained and clashed with the solid mechanics solver (fig.30). In FSI, the fluid model is defined on the moving spatial frame and solid mechanics on the material frame. The ALE method monitors the movement of the fluid mesh relative to the solid deformation which are used as wall boundary conditions for the fluid model. Fully coupled fluid-structure interactions were defined at the vessel-blood and blood-spinal cord boundaries; deformation influence was controlled by prescribed displacements on the exterior of the solid vessel (Figure 27).

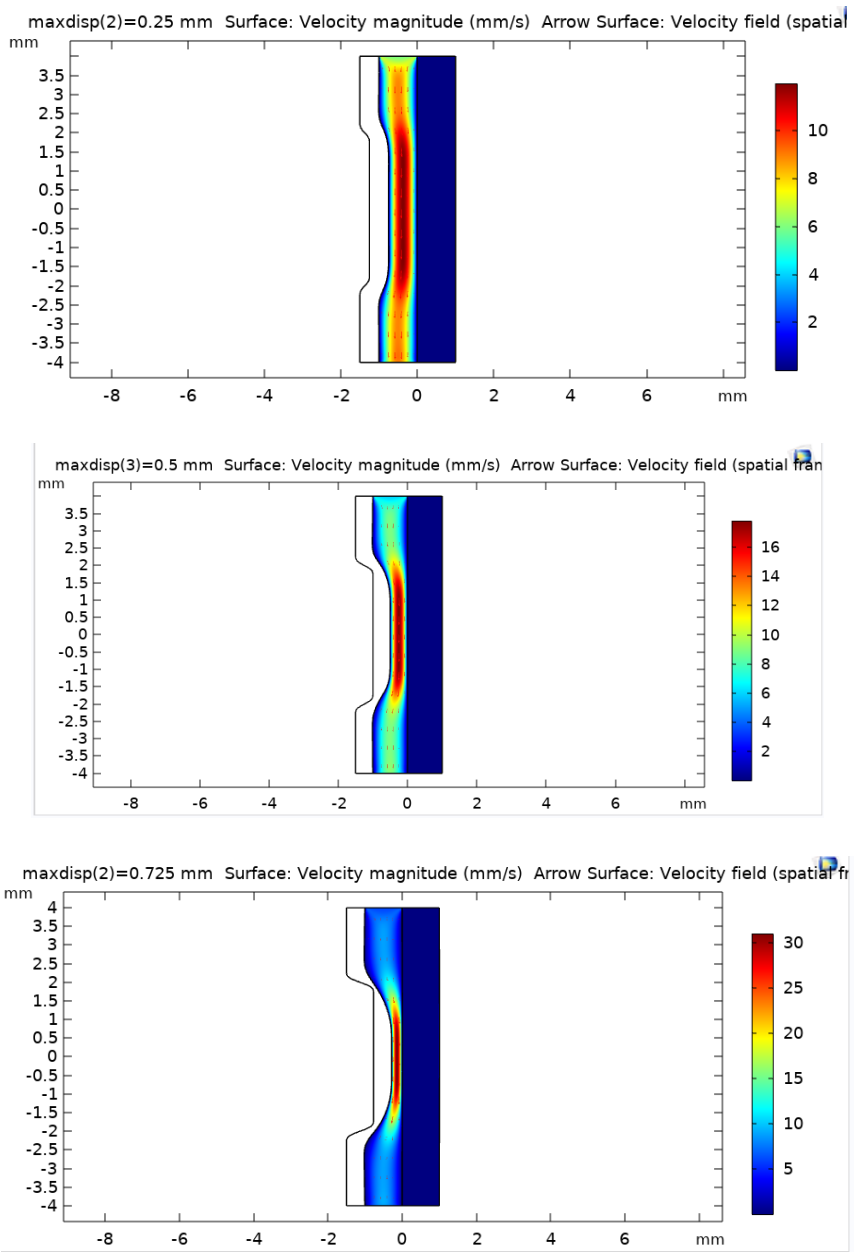

Figure 27: Compression from 0-30% (a-d) effect on velocity magnitude.

In this scenario, deformation was feasible up to 30%, including coupling the porous flow and applying the oxygen model (Figure 28).

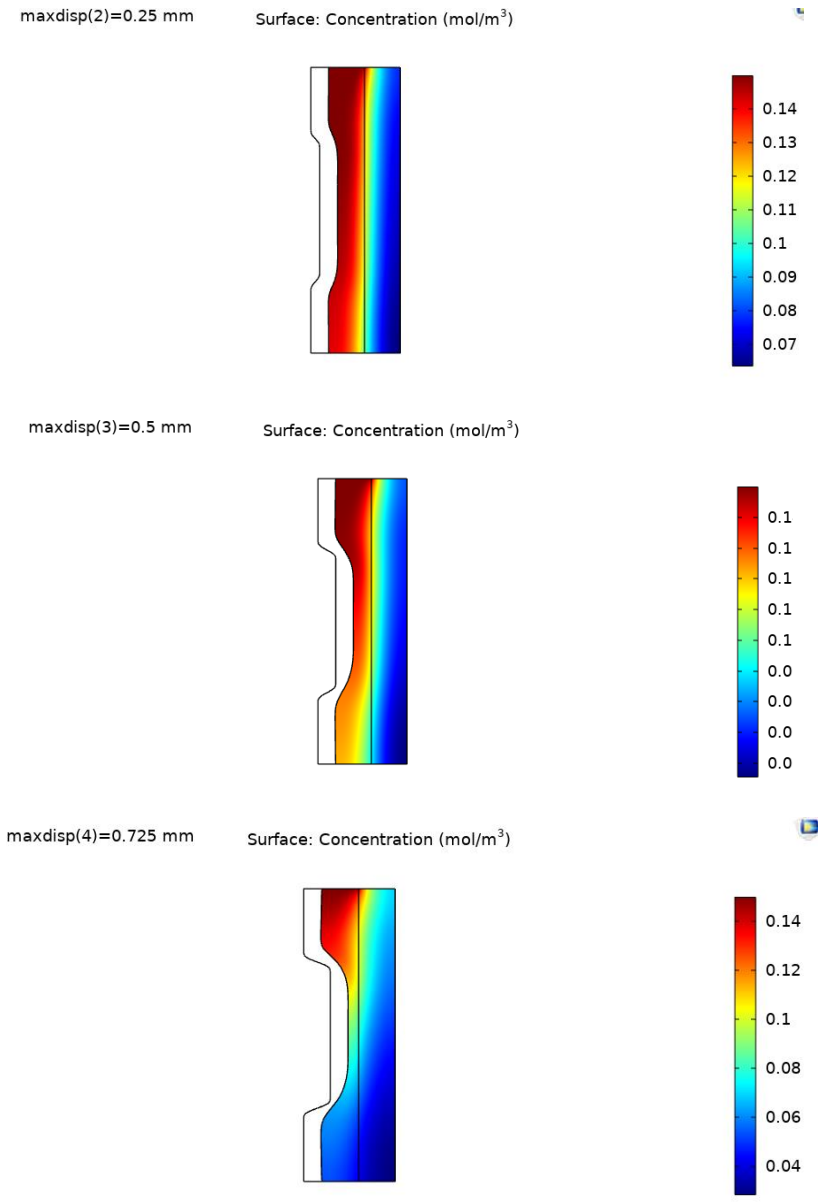

Figure 28: Oxygen concentration at 10, 20 and 30% deformation (a-c).

As expected, oxygen decreased in concentration below the arterial occlusion and therefore presented an uneven distribution into tissue as strain increased.

The model implemented the 2-D numerical aspects and into a 3-D geometry. As below, the interaction was fully coupled between the cord tissue and blood

vessel (Figure 29). This utilised the free-Darcy fluid model and implemented a moving mesh on the tissue.

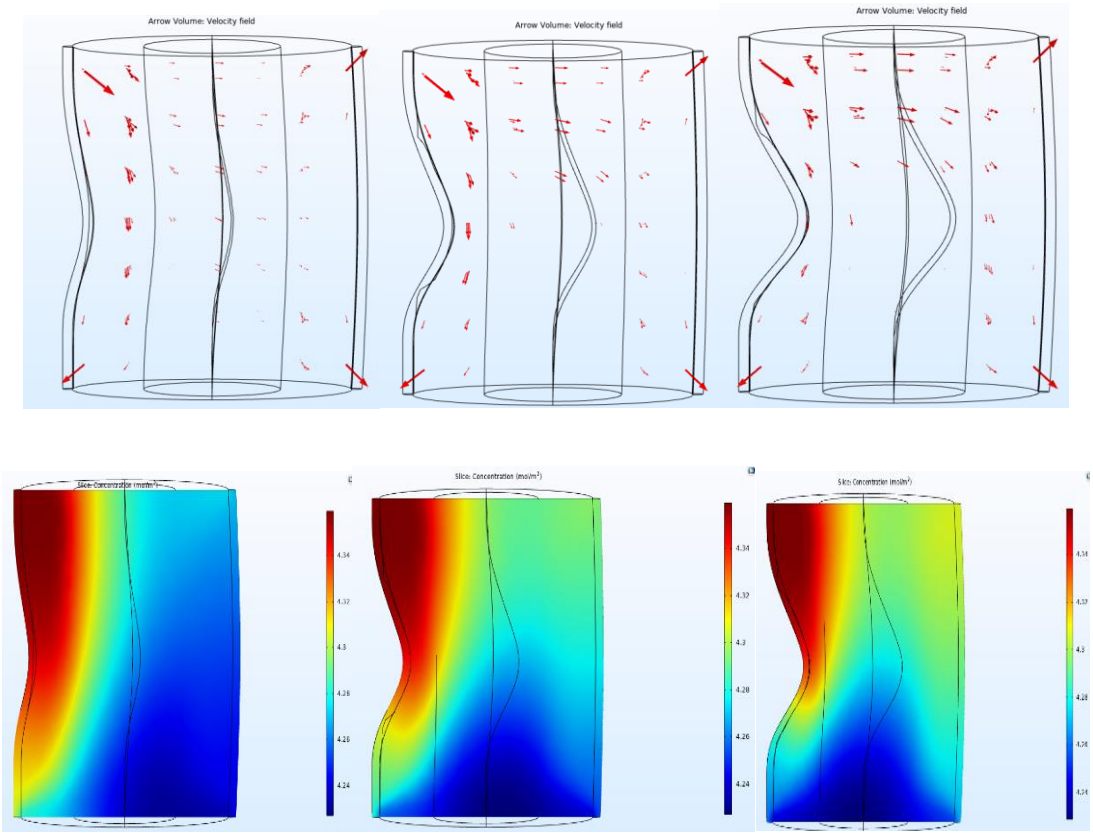

Figure 29: Blood velocity vectors (a-c) and oxygen concentration profiles (d-f) at 10, 20 and 30% compressions respectively.

Upon modelling the velocity vectors, fluid was being forced from the high pressure inlet into the tissue above the compressed region, with increased effect under higher strains. Below the compression apex, internal velocity vectors were negligible. This was expected and could be indicative of zones of lower fluid pressure as the pressure gradient decreases longitudinally down the arteries. It is expected that overall flow rate and oxygen availability would eventually decrease, after having increased due to compensatory

mechanisms. As below, the model displayed compensatory behaviour even at higher strains in the free-Darcy model (Table 18).

Table 18: Summary of average velocity magnitudes and oxygen concentrations in the free-Darcy model under a range of sub-clinical strains.

10% strain	**Tissue**	**Velocity (mm/s)**	**Concentration (mol/m^3)**
	Full cord tissue	0.63	4.29
	Gray matter	4.65×10^{-5}	4.28
	White matter	0.94	4.3
	Artery	11.6	4.34
	Vein	0.22	4.25
20% strain	**Tissue**	**Velocity (mm/s)**	**Concentration (mol/m^3)**
	Full cord tissue	0.67	4.29
	Gray matter	7.4×10^{-5}	4.28
	White matter	1.02	4.3
	Artery	11.9	4.33
	Vein	0.14	4.28
30% strain	**Tissue**	**Velocity (mm/s)**	**Concentration (mol/m^3)**
	Full cord tissue	0.74	4.29
	Gray matter	9.84×10^{-5}	4.28
	White matter	1.16	4.3
	Artery	11.7	4.32
	Vein	0.1	4.29

However, arterial velocities and changes in vascular output were grossly under-estimated and therefore the aforementioned Brinkman model was

implemented (section 3.4.3) and the FSI model was altered to be fully coupled, which enabled stabilisation of the fluid behaviour when under strain.

3.7 Summary

Relative to the analysis of different governing physics and parameters, the work presented in this chapter led to the finalisation of the model setup.

- The implementation of a smoothed function meant displacements could be applied without harsh boundaries that cause mesh inversions and divergence of the solver.
    - This aspect enables changes in injury profile meaning focal and diffuse injury profiles can be studied parametrically alongside other variables.
    - Modelling solely solid deformations as presented in this section of the work meant the model could achieve strains of >30%, when employed with a moving solid mesh. However, on the inclusion of fluid modelling and the requirement for FSI, the solid deformation model was limited to 7.5% strain for anterior and posterior injuries and 10% for anteroposterior injury.
- Implementation of Brinkman's model accurately governed the transitional flows between arterial free flow and capillary porous flows.
    - Darcy flow underestimated the velocity and pressure gradients of the microvasculature in tissue due to the lack of viscous shear.

- Analysis of appropriate porosity and permeability values for white and grey matter highlighted that anisotropy is not an essential criterion for inclusion in simulating tissue blood flow through white matter. The model agreed with claims that anisotropy can over-estimate flow behaviour in porous models [136]. White matter permeability was defined relative to the known permeability of capillaries in the brain [182].
- Grey matter permeability was defined relative to a known permeability of arterioles in the brain [182]. The tissue was prescribed a larger volume fraction of pore space via porosity and a lower resistance to flow, relative to white matter, which had a lower pore volume space and higher resistance to flow. This aligned with the known fibre and vessel densities relative to the literature.
- Applying a sink function to the grey and white matter meant the tissue could not surpass its maximum threshold (arterial oxygen concentration) and that it could not deplete below zero. This meant the model had the ability to compensate for a lack of blood flow by increasing its consumption rate to maintain the oxygen baseline.
- Over-constraint of the fluid-structure interaction model meant the solver would not converge. Shared boundaries are employed at the artery fluid walls and neighbouring spinal matter walls. A fully coupled FSI approach was most suitable instead of a uni-directional solid effect on fluid; it is known that disruption of the cytoskeleton and vascular structures has concurrent and synergistic effect on fluid behaviour and vice versa [80], [196], [198].

The baseline simulations of input parameters, mesh verification and comparison to the known literature are presented in chapter 4 and parametric analysis of injury type effect on tissue response is presented in chapter 5. Parametric analysis solves for a sequence of stationary problems when the maximum deformation (chapter 3.3) is varied.

Chapter 4

Model verification and inclusion criteria validation

On finalisation of model input setup, verification and validation of the model was completed prior to investigative simulations of the location and injury profile parameters, presented in chapter 5.

4.1 Mesh verification

Verification of the mesh was completed to ensure consistency and accuracy of outputs by ascertaining the minimum number of elements required for convergence of the mathematical approximations. Mesh verification enables reliability of outputs when other parameters, such as displacement, are altered. Output variations can therefore be accounted for by the alterations to those inputs.

The mesh convergence testing ascertained the mesh density and localisation properties required for consistent solid and fluid outputs in line with those seen in the literature. The scale of geometries present was likely to be effectual on convergence; blood vessels had a 10-fold smaller diameter than the spinal cord, therefore convergence required a denser mesh for blood vessels. Below, velocity and concentration values were obtained by finding the output average over the anatomical volume (i.e., artery, vein, grey matter, white matter). Convection of oxygen in tissue was dependent on the fluid flow behaviour, so was inherently influenced by the upstream fluid velocities. Therefore, concentration was expected to follow the convergence profile of the fluid model

outputs. Below, convergence plots are shown for the velocity and concentration profiles of each cord anatomy (Figure 30).

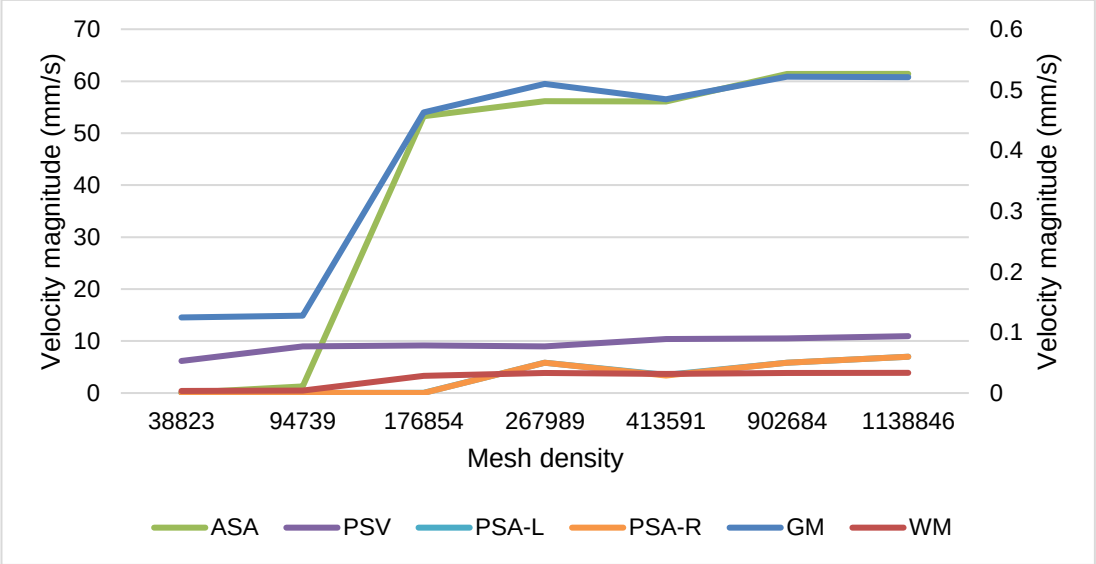

Figure 30: Mesh convergence of average velocity magnitudes (mm/s) of the simulated anatomies. The left axis scale represents ASA velocities, all other anatomy velocities are relative to the right axis' scale.

Increases in mesh density ranging 2-4x were employed until convergence of simulation outputs, defined as less than 10% deviation between outcomes, which is a known benchmark in finite element modelling that indicates model consistency. These simulations were run with no deformation applied; on addition of the deformation of multiple parameters to be run in one simulation, the computational capacity significantly lessens. Relative to the deviation of the mesh within 10% and the solver requirements to simulate the deformation accurately, a minimum total mesh of 267989 was required for appropriate convergence, as visualised in Figure 31.

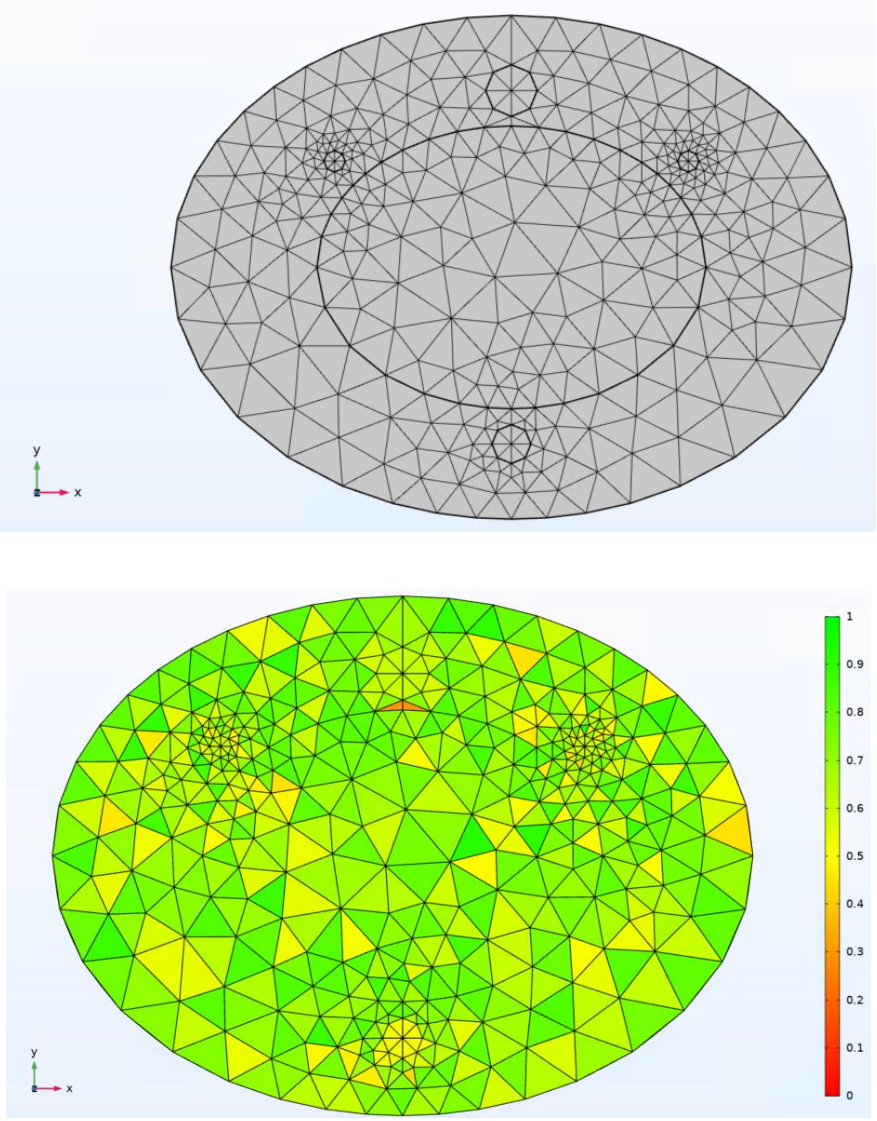

Figure 31: Finalised mesh of the spinal cord model (a) and mesh quality plot analysing mesh skewness (b) where green=low skewness and high quality.

Localised, denser meshing was required on the arteries and lower densities for the spinal tissues and vein. Relative to the mesh quality plot (Figure 31b) some weaker elements (coloured orange) are located at the boundary edges and within the smaller vessels. The number of elements required for convergence for each anatomy was as below in Table 19.

Table 19: Number of mesh elements per anatomy.

Anatomy	Number of elements
Anterior spinal artery	7322
Posterior spinal vein	1968
Posterior spinal artery (L+R)	5160 + 5168
White matter	201652
Grey matter	46719

As expected, larger anatomies (white and grey matter, ASA and PSV) required lower mesh density relative to volume as larger elements could accurately represent the anatomy. Smaller blood vessels (PSA-L and PSA-R) required a higher number of smaller elements to give accurate representation over the smaller anatomy volume. It is known that integrals over a larger model space will converge faster (grey and white matter) and local values will converge most slowly (posterior arteries). The posterior spinal vein value did not vary in concentration as it behaved as a constant sink in the model.

4.2 Solid model comparables

Validation of the solid model – namely severity and profile of injury – was planned to be done *via* parametric simulation of *in vivo* strain profiles as displacement curves. This dataset was the most accessible at the time, derived from an internal *in vivo* study that simulated mild and severe non-traumatic injuries *via* a balloon occlusion model. However, the outputs ultimately could not be simulated in the model as the strains achieved *in vivo* (>40%) were much higher than the computational model threshold (<10%).

4.2.1 *In vivo* injury severity and profile as inclusion criteria

In vivo data surrounding the non-traumatic deformable mechanics of spinal tissue is limited, due to the complications of the investigative conditions, including animal welfare and feasibility of long-term usage of apparatus. An *in vivo* model of NT-SCI was carried out by Timms [21] to elucidate the effect of chronic spinal cord compression on functional output in rodents. The experimental study, histology and imaging was undertaken by Timms. The image measurements and analyses presented in this chapter were performed separately for this project to investigate research questions relevant to this thesis. Six female Wistar rats were anaesthetised using 5%(v/v) isoflurane in oxygen at 2L/min and incisions of 2-3cm were made from approximately T6-T12. A partial laminectomy of the right-hand side was done at T10 for introduction of a balloon-catheter system on the right-hand lateral edge of the spinal cord. The catheter was pushed rostro-ventrally for 1cm, therefore the balloon ultimately resided at T8-T9. An injection port was made by feeding tubing to the T10 level from an incision made between the shoulder blades, which enabled addition of fluids to slowly expand the balloon. The balloon was inflated daily for three days post-surgery. Sham (n=2) subjects had the system implanted but not inflated, meanwhile mild (n=2) inflated up to 12.5µL and severe (n=2) subjects up to 15µL. Mild and severe injuries output Beattie, Basso Bresnahan scores (appendix A) of 18 and 10 out of 25, respectively. Animals were sacrificed and perfused after maximal inflation was achieved, for sectioning of the injured cord in 40µm sections to undergo hematoxylin & eosin (H&E) staining.

Histology sections were analysed to ascertain the strains underwent by the thoracic spinal cord during NT-SCI. Analysis sought to determine the shape and severity of displacement on the cord for replication in parametric studies of the computational model. Histology section dimensions were sized in ImageJ: strain was calculated as the difference in the elliptical axes between the outermost rostral and caudal sections of the animal and those innermost to the injury epicentre. This assumes a constant diameter longitudinally down the sections. Each study group (sham, mild, severe) had sections taken 7mm, 5mm, 2mm, 1mm caudal to the 0mm epicentre and -7mm, -5mm, -2mm, -1mm rostral to the epicentre. Therefore, average displacements were derived from the +/- 7mm rostral/caudal sections as the base from which a change in diameter and strain can therefore be calculated from.

Both white and grey matter strains were analysed: the coronal axis of the transverse cross-section of the cord was measured from the hematoxylin-stained dura mater that circumferentially lines the cord tissue, measuring through the midline of the lateral grey columns and central canal (Figure 32a). The sagittal axis was measured from the hematoxylin-stained boundary of the anterior to posterior funiculus, running directly through the centre of the ventral grey columns (Figure 32b). The same approach was taken when analysing grey matter, but measurements were taken from the external boundaries of the hematoxylin-stained, cell-nuclei dense grey matter to run through the lateral grey horns via the central canal (coronal axis) and through the ventral and dorsal horn midlines (sagittal axis) (Figure 32c-d).

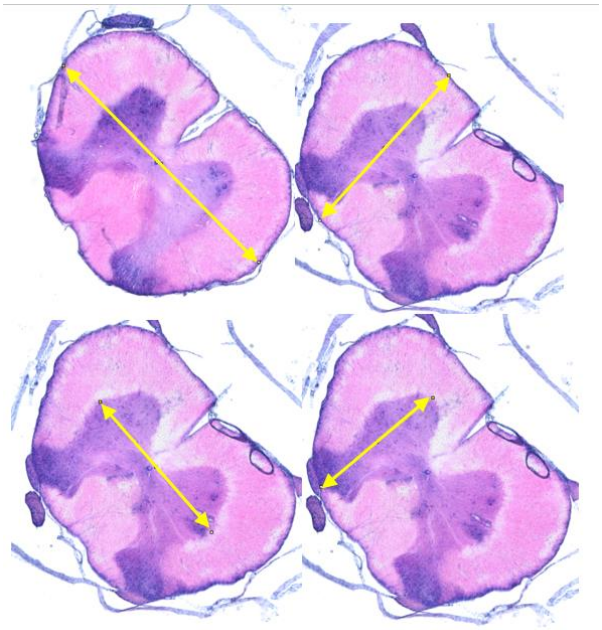

Figure 32: Strain measurement methodologies for white matter and grey after *in vivo* injury, adapted from Timms [21]**.** Measurements were taken (yellow line) through the geometry to determine the coronal (a) and sagittal (b) dimensions for the white matter and the same for grey matter (c-d), relative to the image scale of 603 pixels/mm.

On receiving the images (Figure 33) from the Timms study [21], strain analysis was undertaken for this work. Sagittal and coronal strains were compared for both white and grey matter individually, in both mild and severe injury groups which are presented in**.** Each injury group had two specimens, labelled respectively, and the per cent axes change described a decrease under compressive strain when negative. Positive per cent axes changes represented tensive strain and an increase in dimension (Figure 34).

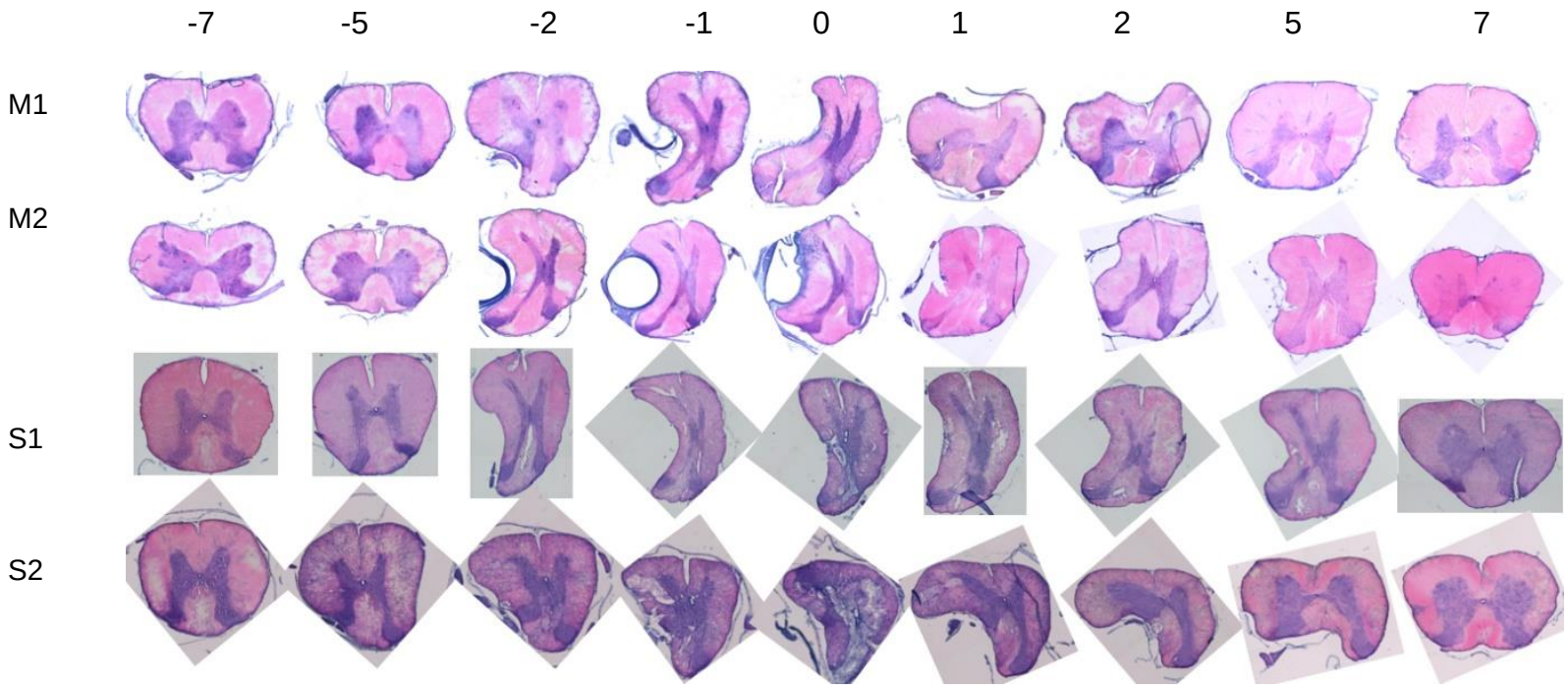

Figure 33: Histological slices of mild and severe spinal cord injury surgeries performed at T9 level of rat, adapted from Timms [21]**.**

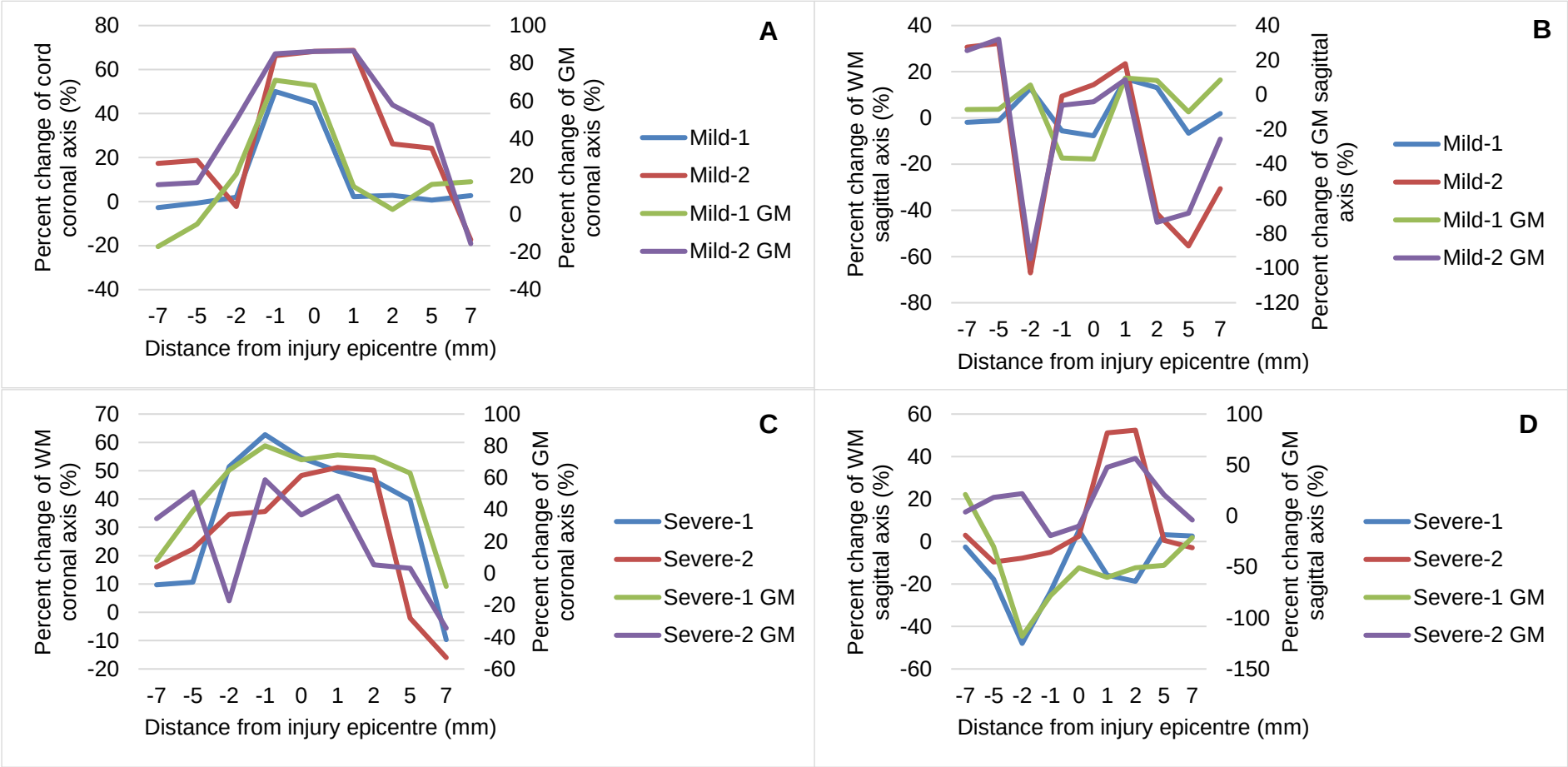

Figure 34: Strain profile of coronal (A+C) and sagittal (B+D) dimension alterations in both white and grey matter in the mild (A+B) and severe (C+D) injury group.

Under mild injury, the coronal axes of the white matter and grey matter seem to follow the same displacement behaviour and profile. However, under severe injury, grey matter strain is pronounced, which correlates with the literature definitions of NT-SCI, namely the disruption of the grey matter cell nuclei under higher strains [67]. There was agreement between injury severity groups that the injury epicentre underwent the highest deformation, with segment levels further from the injury receiving less strain: these data informed the development of the bell-shaped deformation function in the model.

As well as determining the strain cross-sectional lengths, analysis was done to determine the changes in spinal cord area (Figure 35). Histological sections were converted to 8-bit monochrome, with a threshold of 200 applied to isolate the spinal tissue from slice debris. This threshold separated the hematoxylin-stained white matter perimeter and grey matter from the internal eosin-stained white matter. Some section images required deletion of extraspinal tissues that remained, such as the dura and meninges. The outer perimeter of the isolated white matter tissue was identified as the region of interest, with measurement analysis of the area done using in-built ImageJ tools.

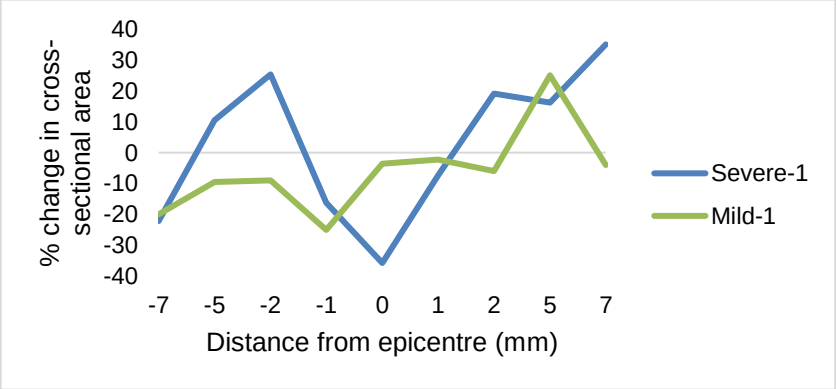

Figure 35: Cross-sectional area measurements of spinal cord histology sections.

The data presented is reflective of one animal from each study group (mild and severe where n=2 for each); the second animal group datasets had re-sized source images for the rostral sections (-7 to -2 mm), therefore the presented areas were skewed relative to the globally applied scale and were thus neglected. The visualised data infers similar trends to the cross-sectional axes lengths. Animals from the sham injury group (not presented) had relatively consistent areas spread through the section slices as expected, meanwhile animals in the mild and severe injury groups decreased in area at the injury epicentre, with lesion severity decreasing at sections further rostral and caudal from the epicentre. Severe injury showed similar trends to current computational data, as increased degree of compression further reduced area at the injury epicentre and immediate cranial-caudal sites, whereas mild injury presented as an even distribution of decline in area [26].

The data presented above highlights the differences of injury severity relative to degree of compression. These align with previous FEM data highlighting lower stresses at 10% and 20% strain, but an increase in intramedullary stress leading to grey matter degradation at a threshold of 30% strain [26]. The mild injury groups displayed a BBB score of 18 after 20 days of balloon implantation, meanwhile severe-group subjects displayed BBB scores of 10 at the same timepoint. The dataset presented infers that strain is not the sole determinant in functional outcome, due to similarity in severity, location and timescale – rate of change of occlusion was deemed an essential factor in determining functional outcome between mild and severe injury groups [4]. It is important to note that balloon occlusion models have been critiqued in their capability to produce true injury representations due to a lack of fixation *in vivo*,

allowing for movement and therefore stress variability across longitudinal studies.

However, relative to the profiles of strain inflicted in this model; it is known that displacements that spread laterally along the superior-inferior axes of the cord create stresses of an even distribution throughout all segments, whereas focal displacements create higher, localised stresses throughout the afflicted segment (Figure 36) [23]. Diffuse injury is the most destructive as it induces the highest stresses through both the grey and white matter [23].

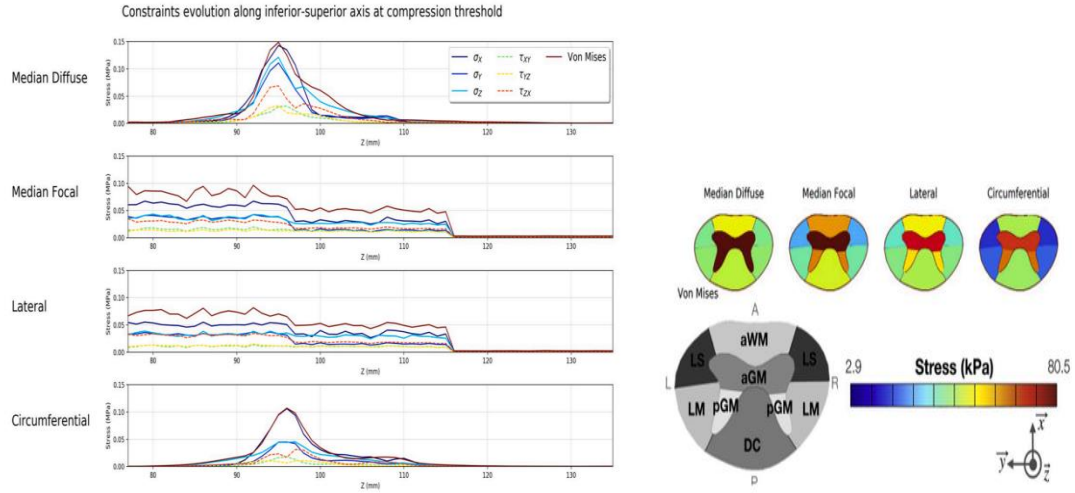

Figure 36: Outputs of stress constraints up to 30% compression (95th percentile of the absolute value by millimetre) along the inferior-superior axis for different strain profiles (a), visualisation of von Mises stress outputs under differing strain profiles (b). (Adapted from [23])[1].

1 Adapted and re-printed from Clinical Biomechanics and The Lancet, Vol 81, January 2021, Levy *et al.*, "Biomechanical comparison of spinal cord compression types occurring in Degenerative Cervical Myelopathy", p.105174, (2020), with permission from Elsevier.

These data were derived from FEM models of the human spinal cord but the mechanical assumptions can be assumed as similar to the rat spinal cord behaviour, which is commonly used for *in vivo* representation [105]. It could be inferred that the diffused compression of the sagittal anteroposterior axis of the grey matter resulted in poorer functional outcome in the severe study group. The mild injury group subjects displayed a consistent area change across a 2mm injury zone, whereas the severe group showed a severe compressive decrease at the epicentre, spread across a 4mm injury zone, highlighting the importance of injury profile and not necessarily the severity of strain, which agrees with the clinical literature [18]. The maximum diameter of the balloon used in occlusion reached 2.8mm, which agrees with a balloon occlusion model in dogs that highlighted the effect of injury profile on outcome: 2-mm produced 12.5-20% reduction in spinal canal diameter, whilst 4mm caused 28-56% decrease and 7mm caused 62-82% [12] – relative to an average spinal canal diameter of 6-9mm for dogs – this would infer a correlation between injury profile, mechanical stress and functional outcome.

In terms of the vasculature, a balloon occlusion study in monkeys found that compressions deeper than 2mm occluded the sulcal arteries [20]. Therefore, focal injuries should be modelled as 2mm spread and diffused injuries as 7mm in the model presented in this thesis. Relative to the underlying vasculature, no changes were observed in the number of blood vessels but the diameter of underlying blood vessels decreased by approximately 7% in the mild injury group and by 50% in severe injury, despite similar deformation severity and location [21]. A previous study implementing absorbable polymer in the rat cervical spinal cord reduced microvascular density by 33% [145]. Studies

utilising human patient data have modelled compression of the cervical region from asymptomatic strain ranges of 10-30% and found that tissue stress-response was relative to the morphology of each segment or compression component [26], [199], [200]. Under 10% strain, a mild increase in dorsal horn stress was evident; 20% strain created stress in the lateral side of the posterior funiculus and 30% compression transmitted stress through the posterior and lateral funiculi. However, under 40% compression, stress was increased throughout the grey matter, lateral and posterior funiculi of all affected segments with little difference in stress profile between the anatomies [26]. Relative to the *in vivo* data presented here, cross-sectional area was consistently reduced by 30% at the injury epicentre and the maximum area decreases varied by 12% between mild and severe injuries, therefore it was hypothesised that a compression threshold between 32 and 44% is where symptom manifestation and the compressive severity threshold lies for NT-SCI, which correlated with literature understanding of 25-50% compression [21].

The *in vivo* data informed inclusion of profile as a study criterion which correlates to the variance in aetiologies and functional outcome. Diffused deformations are seen in degenerative conditions such as CSM and disc herniation, whereas focal injuries are akin to indications such as the ossification of the posterior longitudinal ligament [23]. Ideally, the *in vivo* data would be used as means of validating the computational model presented but the compression thresholds required (20-40% deformation) were beyond the capacity of the model. Similarly, the data infers the rate of development of

injury should be considered in NT-SCI pathophysiology but was not possible to be factored into the modelling undertaken here.

4.3 Fluid model validation

Table 20 lists the expected baseline outputs for the model under healthy settings, derived from *in vivo* measurements of sham animals.

Table 20: Expected model outputs under control and ischemic/hypoxic conditions.

Anatomy	**Velocity (mm/s)**	**Ischemic velocity (70% decrease)**	**Concentration (mol/m^3)**	**Hypoxic oxygen concentration (mol/m^3)**	**Decrease in concentration (%)**
White matter	0.03	0.009mm/s	0.57 [186]– Rat SC white matter	0.35 [188] – Rat brain interstitium	39
Grey matter	0.6	0.21mm/s	0.72 [186]– Rat SC grey matter	0.35 [188] – Rat brain interstitium	51
ASA	40-60 [184], [73]	18mm/s	7.4 [188]	1.96 [188]	74
PSA	5-8 [102]	1.95	3.5 [16]	N/A	N/A
PSV	10 [102]	3mm/s	2.08 [16]	N/A	N/A

The relationships between average vessel diameter and blood velocity in the spinal cord using functional ultrasound and ultrasound localisation microscopy have identified vessel blood velocity behaviour down to microvascular diameters of 10μm, as in Table 21 [102].

Table 21: Velocity data of vascular structures relative to vessel size [102]**.**

Diameter of vessel ± 5(μm)	**Velocity ± 1(mm.s^{-1})**
200 (ASA)	15-20
50	5-8
15 (arterioles)	1-5
<5 (parenchyma)	1
PSV	10

These average velocity profiles can be used to validate the behaviour of the porous microvasculature, but the velocity of the ASA was low at >15mm/s in comparison to other studies. The data was derived from T12-L2 where other vascular supplies are available compared to the mid-thoracic cord when the ASA supplies two-thirds of the blood flow [102]. Arterioles are neglected from the geometry modelled here but are assumed as represented in the porous continuum by the Brinkman equations – the model should therefore produce higher tissue velocities deriving from the feeder arteries of around 1.5mm/s.

A recent study investigating traumatic spinal cord injury in the thoracic spinal cord detailed velocity measurements of vascular flow in larger blood vessels (anterior spinal artery, arterioles) of 4-6cm/sec by using ultrafast contrast-enhanced ultrasound Doppler [73]. This imaging technique enabled separation of higher velocity vessels (larger vessels) and lower velocity microcirculation by injecting microbubbles for visualisation of blood flow in real time. The study had defined a critical loss of perfusion as below 40% perfusion compared to surrounding tissue [81]; CT images from patients deduced that a decrease by 70% perfusion rate was the threshold in which a tissue region was defined as

ischemic [201], therefore worst-case ischemic conditions were derived from this assumption and that of *in vivo* data that highlighted a loss of function at <30% cerebral blood flow [72].

Oxygen concentrations were derived for both thoracic spinal cord matter types from hydrogen clearance microelectrode techniques [186]. Oxygen tension in the arteries of the brain has been measured using electron paramagnetic resonance oximetry [188] and smaller vasculature oxygen tension from the mouse brain was measured by two-photon phosphorescence lifetime microscopy [16]. The effect of hypoxia in the awake mouse brain has been measured *via* a progressive decrease in fraction of inspired oxygen, measured by EPR oximetry. A decrease in inspired oxygen from 30% to 10% elicited a 70% decrease in partial pressure of arterial oxygen and a 55% decrease in partial pressure of spinal tissue oxygen. From these data, it correlates with the literature that a 70% decrease in perfusion results in ischemia and that the correlating oxygen concentrations of provisional arteries also decrease by 70% [201], meanwhile microvasculature in the grey and white matter of the brain decrease by approximately 40-50% in a hypoxic scenario [186],[188]. Therefore, understanding the mechanics required to reduce blood flow rates and oxygen tension by 70% in arteries and 50% in tissue would be a useful indicator of NT-SCI progression into a severe injury.

As below in Table 22, the model outputs aligned with those expected, derived from known values in the literature from *in vivo* models of the spinal cord and brain.

Table 22: Actual model outputs under control conditions.

Tissue	**Velocity (mm/s)**	**Concentration (mol/m^3)**
Anterior spinal artery	61.8	7.16
Posterior spinal vein	9.1	0.5
Posterior spinal artery (left and right)	5.8	2.7
White matter	0.033	0.76
Grey matter	0.51	0.73

The model generally aligns with the expectations of the blood and oxygen behaviour. The oxygen concentrations of the posterior spinal artery are slightly lower than expected but the velocity was at the lower end of its expected range (5-8mm/s), therefore the lower concentration was attributed to that. Microvascular flows behaved as expected relative to geometry setup and numerical implementation of material parameters (Figure 37).

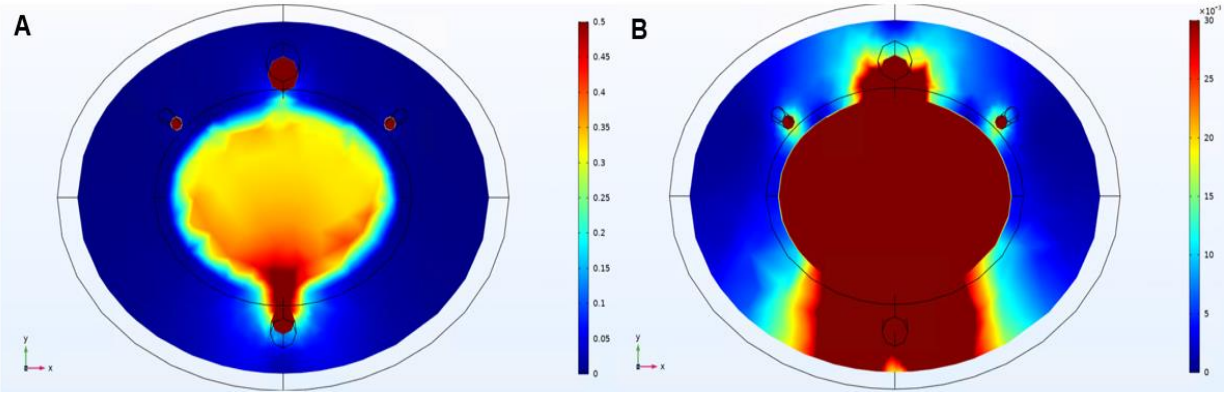

Figure 37: Velocity magnitude (mm/s) of spinal tissue matters at centre of the modelled cord segments (z=0). Contour plot range is 0-0.5mm/s to highlight grey matter (a) and 0-0.03mm/s to highlight white matter (b) behaviours.

The contour plots highlight the importance of the ASA in providing blood flow to the grey matter (Figure 37a); the ventral end experiences higher blood velocities through tissue but is generally evenly spread (figure 37b). Higher velocities are seen beside the arteries, as expected due to the Brinkman model for representation sulcal of arterioles. The white matter indicates spread of blood flow throughout the tissue at capillary velocities and highlights a sparseness of vasculature in the lateral columns (Figure 37b), with a focus on blood flowing through the grey matter directly to the PSV. The posterior arteries provide additional arteriole velocities in the dorsal end of the cord.

The oxygen concentration for white matter was 35% above that expected but did remain in line with the expected values for the rat brain interstitium. It was not expected that white matter would have the same oxygen concentration as the grey matter but relative to the simplifications of the model (same consumption rate across both tissues, geometric location of arteries in the white matter, implementation of capillary-based isotropic permeability), this did not seem unfeasible or unrepresentative of model fundamentals.

4.4 Summary

In analysing the available *in vivo* data and referencing recent works in the literature, relevant parameters and expectations for model behaviour were decided.

- The requisite mesh density for convergence was 267989. Larger volume integrals (white and grey matter) converged at lower mesh densities than those that required localised, finer densities (posterior arteries).
- The baseline model with no deformation produced outcomes in line with that of the literature.
- The *in vivo* data agreed with the literature that severity is not a sole predictor of severity of outcome.
    - Injury profile appeared to be contributory to functional outcome differences seen between mild and severe injury groups, which is assumed as representative of the varying aetiologies and respective outcomes across NT-SCI injuries.
        - A key contributor to NT-SCI is also assumed to be the rate of injury, which is known to significantly affect functional outcomes assumed as due to rate of occlusion of contributory blood vessels and underlying microvessel densities. The work presented here focuses on stationary models of injury so this is not considered but an increase in severity could be assumed as a proxy for injury development.

- Modelling the change in vessel densities would be viable if the spinal tissue fluid models were governed by poroelasticity, in which the shape of the porous skeleton (spinal tissue) and the fluid (blood) are fully coupled to each other in terms of deformation and ease of flow. However, this interaction cannot be coupled to the larger structure FSI to account for external deformations on free-flowing arteries, therefore was not pursued in this work due to the known importance of the ASA in the thoracic NT-SCI scenario.

Therefore, the model was validated against the expected outcomes from the literature and robustness of the mesh was assured from convergence analysis. Definitions for ischemia and hypoxia relative to known values from the literature were derived. Injury parameters for assessment were also validated relative to gaps in the literature, namely in terms of bridging the current understanding around injury profile, location and severity relative to vascular response. Parametric analyses were therefore undertaken to elucidate the behaviour of blood flow and oxygen transport in mild NT-SCI scenarios (chapter 5).

Chapter 5

Parametric analysis of blood and oxygen response to non-traumatic spinal cord deformation

Parametric analyses were run to ascertain the developmental pathophysiology of NT-SCI during mild compression (defined as 0-10% compression). As mentioned, the location (anterior, posterior and anteroposterior) of injuries produce outcomes that differ relative to the underlying vascular and anatomical structures effected [19], [26]. Previous papers have highlighted that stress produced by NT-SCI was influenced by spinal segment anatomy and profile of the injury [23], [199]. It was already known that stress is correlated with injury progression and that severity of strain is not a key indicator of injury outcome [1], despite an understanding that 30% compression of the spinal canal diameter is assumed as the symptomatic threshold [23]. Therefore, the early development of the pathophysiology below this threshold remained misunderstood. In order to gain a better understanding of the injury processes, particularly around vasculature in the early development of NT-SCI, simulations of two injury profiles across three injury locations at subclinical compressive strains were done to identify trends in behaviour during the early onset of NT-SCI.

Displacements are applied on the anterior, posterior and anteroposterior regions of the cord with increasing strain intervals of 2.5% up to maximum compressions of 7.5% in anterior and posterior models and 10% in the anteroposterior injury model. Anterior and posterior simulations were limited in deformation capacity as the solution would not converge at higher degrees of

compression (~10%). Displacement profiles were analysed over spreads of 2mm to represent focal strain (focused within one spinal segment) and over a 7mm spread to represent diffuse strain (spread over 2 spinal segments), relative to the analysis in chapter 4.

5.1 Blood and oxygen response to injuries

Parametric simulations were run to investigate the relationship between compressive mechanics and blood and oxygen dynamics in the spinal cord during early development of NT-SCI. The blood and oxygen responses of different anatomies (ASA, white matter, grey matter) within the injury scenarios are presented below.

5.1.1 Anteroposterior injury

The majority of papers in the field model injury at the anteroposterior location, as it is easiest to replicate *in vivo* and therefore validate [202]. Models were run with displacement profiles of 2mm and 7mm at 0, 2.5, 5, 7.5 and 10% compression (defined by per cent reduction of the coronal cross-section of the spinal cord) on the lateral face of the cord, applied in the x-direction. The anteroposterior compression models were most effectual on the posterior spinal artery as expected, due to its proximity to the injury site. In the diffuse scenario, the posterior spinal artery closest to the injury site experienced a 10% decrease in average pressure. The PSA showed an increase in oxygen concentration alongside a low increase in velocity under diffused injury, but

both effects represented a <1% change. Changes to blood velocity and oxygen concentration in the white and grey matter are as follows (Figure 38):

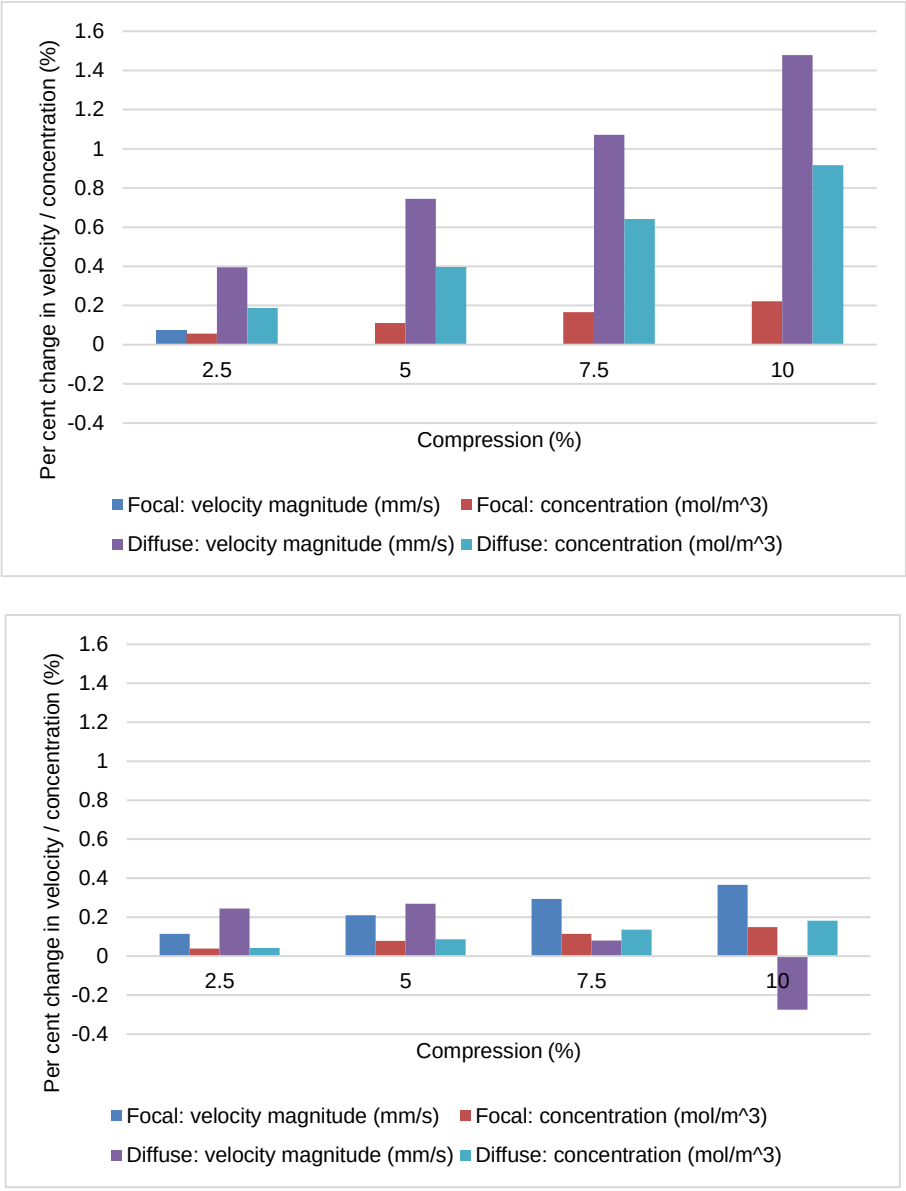

Figure 38: Fluid outputs of the white matter (a) and grey matter (b) response during increasing anteroposterior compression from 2.5-10% under both focal and diffuse compression injury profiles.

Average blood pressure remained roughly the same across all anatomies; relative to the pressure-driven governance of flow in porous tissue, this would elicit little change in blood velocities. Average velocity magnitudes in the white

matter increased by 1-1.5% across the two injury types (Figure 38b). An increase in white matter concentration coupled to increase blood flow speeds provide a compensatory effect. Under strain, white matter fibres have been known to become more isotropic due to compaction and therefore increase the radial and axial diffusivity potential, namely in the lateral and dorsal columns where anisotropic white matter is dominant [203]. Grey matter velocity magnitudes incrementally increase under increased focal anteroposterior strain (Figure 38c). Under diffused injury, grey matter velocities increase marginally but then decrease to below its baseline at 10% strain. The compression of the white matter lateral horn has likely skewed the posterior spinal artery concentration gradient and white matter has therefore increased its velocity to maintain concentration levels. This is highlighted by an increased oxygen extraction rate of 2.5% in white matter experiencing diffused injury, which increases its average oxygen concentration by ~1%. Grey matter (in both injury profiles) and focally injured white matter only experience slight increases in consumption rate (0.5%) (Figure 39).

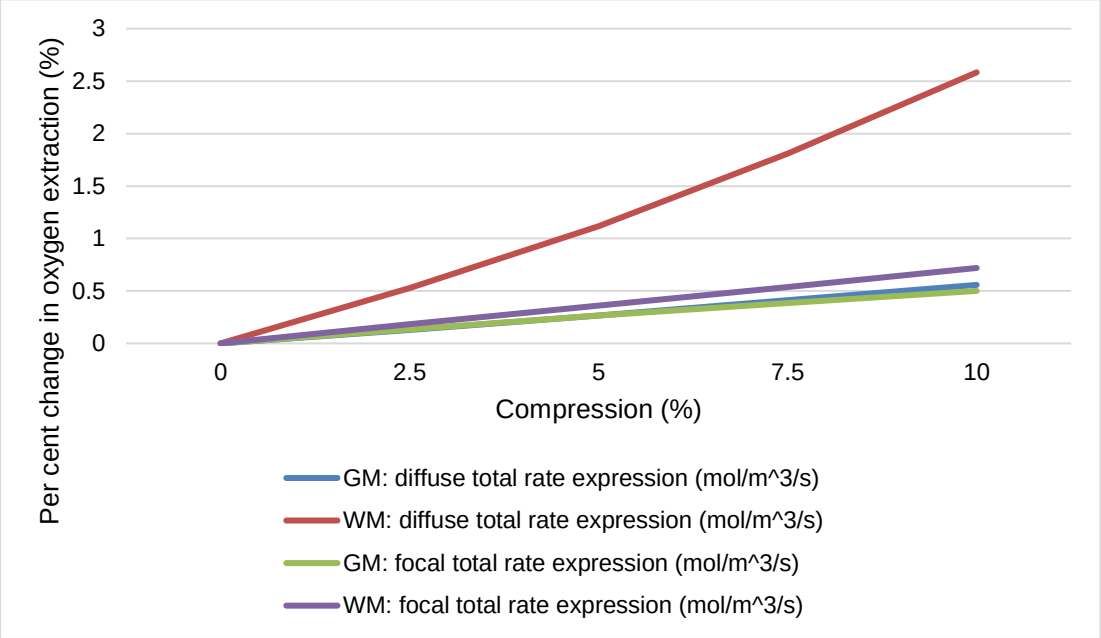

Figure 39: Oxygen extraction rate of the grey and white matter under focal and diffuse anteroposterior injury conditions.

It was therefore assumed that compensatory behaviour of the porous microvasculature took place to balance the system by increasing oxygen extraction rate and blood velocity in the compressed white matter, which has either diverted flows from the grey matter at 10% compression to compensate for white matter tissue ischemia, or early development of ischemia may have been triggered in the grey matter at this threshold. This level of low detail cannot be surmised from the model.

5.1.2 Anterior injury

Models were run with displacement profiles of 2mm and 7mm at 0, 2.5, 5 and 7.5% compression (defined by per cent reduction of the sagittal cross-section of the spinal cord) on the anterior face of the cord, applied in the y-direction. Diffused injury elicited more drastic changes to blood and oxygen behaviour than that of focal injury, as expected, due to a larger section of the ASA and adjacent arterioles being compressed (Figure 40).

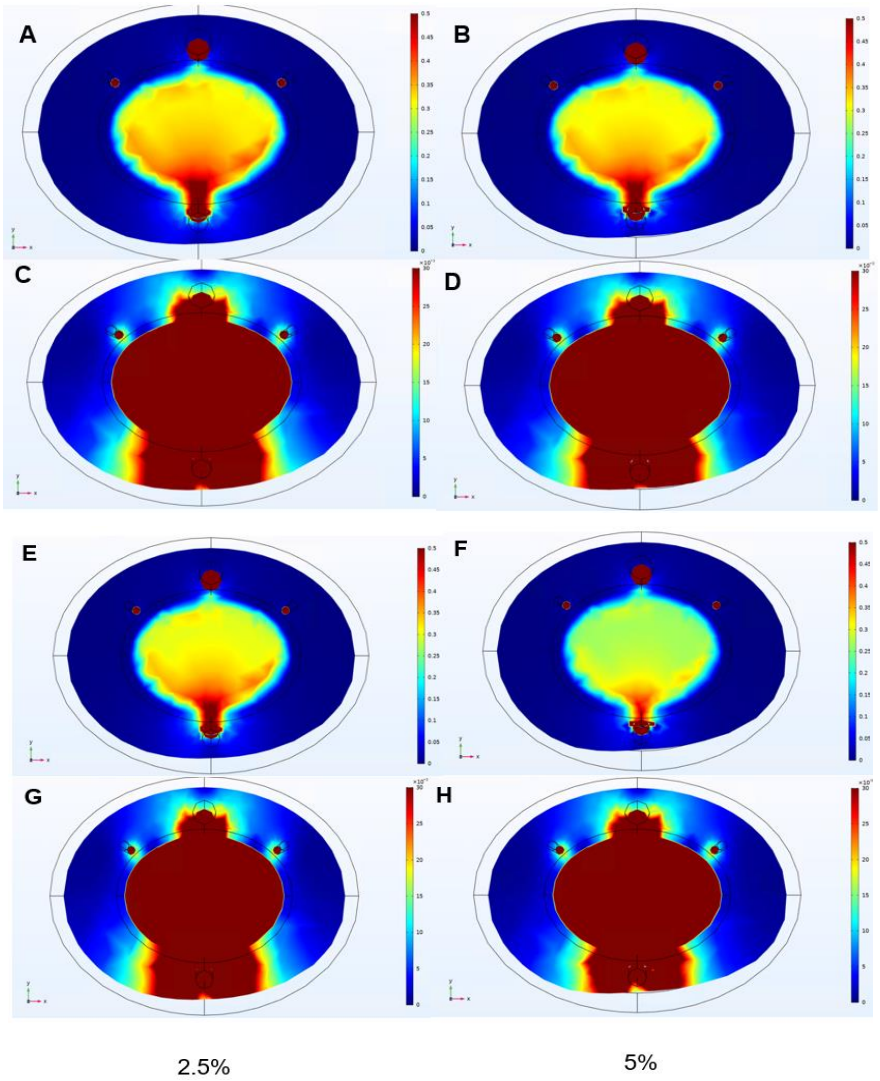

Figure 40: Velocity magnitude (mm/s) plots for focal (a-d) and diffused (e-h) anterior injuries. Plot scale range = 0-0.5mm/s for grey matter behaviour (a-b, e-f) and 0-0.03mm/s for white matter (c-d, g-h).

Flow is directed into the grey matter but a decrease in velocity can be seen flowing from the ASA into the grey matter as compression increases. Blood flow in arterioles adjacent to the arteries also decreases as compression increases. Diffused injury again elicits a greater decrease in average velocity magnitudes. The plots highlight the effect of anterior injury in decreasing blood flow to the ventral horns and anterior sulcal arteries, which has been assumed as a core ischemic mechanism in the pathophysiology to date [204].

In the ASA, the pressure decreased by 2% in the focal scenario and by 10% in diffused injury. Its velocities did not alter significantly; the ASA is known to have little collateral vasculature supply. Pressure drops were similar in grey and white matter under focal injury (~3%) but experienced a sharper decrease in pressure of around ~20% during diffused injuries. This highlights the dependency of the pressure-driven porous physics on the provision of the core arteries.

The behaviour of the white and grey matter are as below (Figure 41):

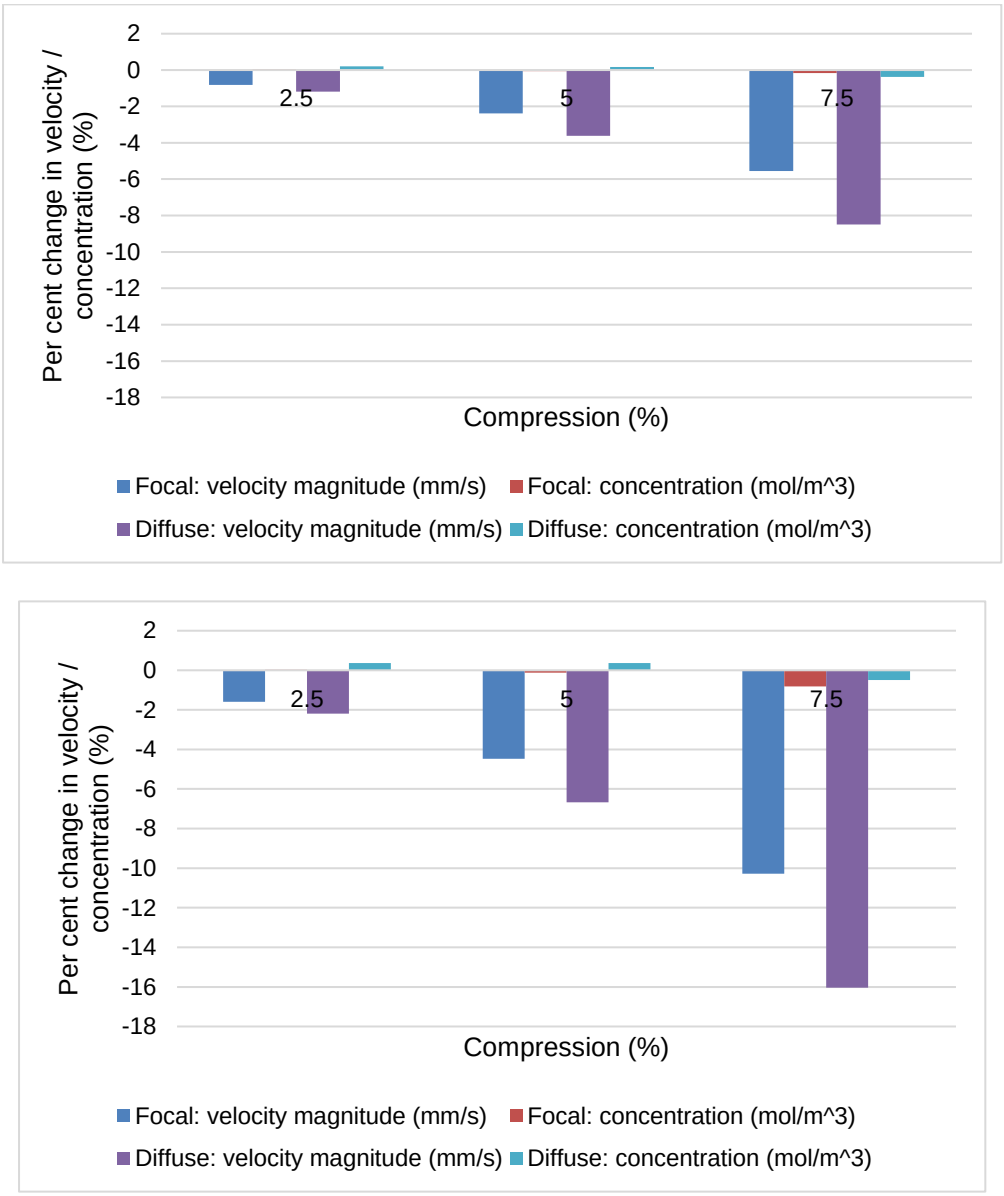

Figure 41: Fluid outputs of the white matter (a) and grey matter (b) response during increasing anterior compression from 2.5-7.5% under both focal and diffuse compression injury profiles.

Concentration remained close to baseline in both tissues for both injury profiles during anterior injury. However, velocity magnitudes of the tissues decreased below baseline in both injury scenarios at the lowest degree of compression at 2.5%. Decreases in grey matter blood velocity were double that of those seen in the white matter. These data agree with the literature in highlighting

the susceptibility of thoracic grey matter to NT-SCI on occlusion of the ASA [161]. On blood velocity decreases of 10-15% in the grey matter and 5-8% in the white matter during focal and diffused injury respectively, it could be assumed oxygen concentration would therefore also decrease. However, oxygen consumption increases immediately during compression, with double the rate of consumption seen in the grey matter (Figure 42).

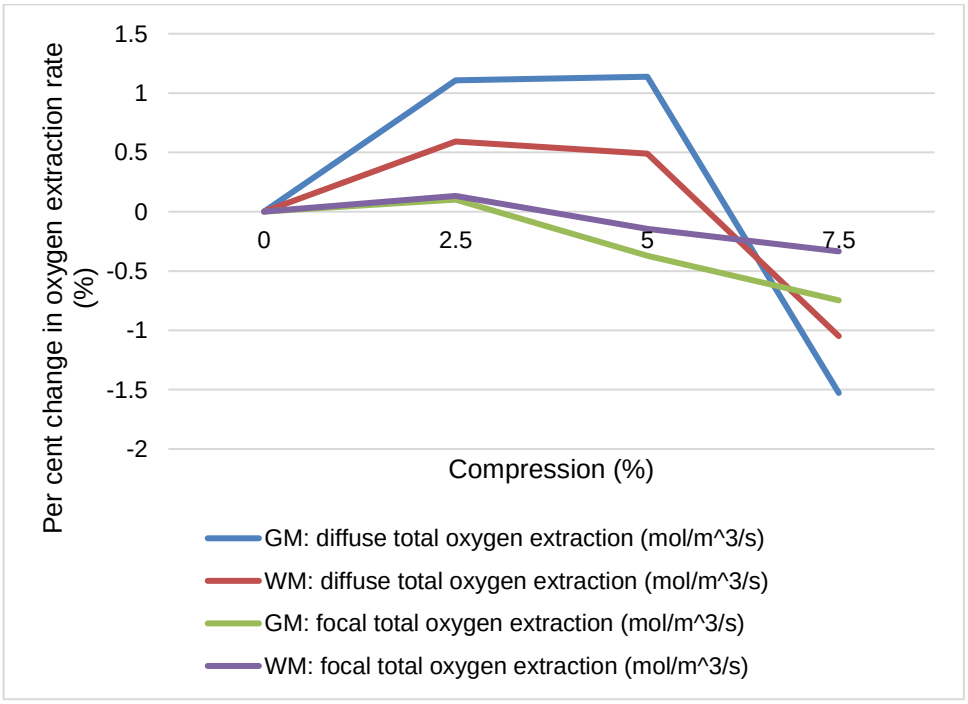

Figure 42: Oxygen extraction rate of the grey and white matter under diffuse anterior injury conditions.

Consumption plateaus at mild compressions of 2.5-5% but the tissues stop extracting oxygen at >7.5% compression and tissue concentrations begin to drop below baseline. This could infer early onset or triggering of the ischemic-hypoxic threshold in anterior injury when tissue flows are decreased by >8%.

5.1.3 Posterior injury

Models were run with displacement profiles employed at the posterior face of the spinal cord with deformation, applied in the -y direction. Displacements of 2mm and 7mm at 0, 2.5, 5, and 7.5% compression (defined by per cent reduction of the sagittal cross-section of the spinal cord).

The posterior blood vessels presented with no significant vascular response except for a 10% pressure increase in the posterior artery closest to the diffused injury site, which is assumed as due to flattening of the vessel and a subsequent increase in pressure to compensate for sustained blood flow. Anterior vessels were not affected, as expected.

The white matter experienced a slight increase in pressure (~2%) across both injury profiles, meanwhile grey matter presented a slight decrease (~2%). Velocity and concentration data for the spinal tissues are as below (Figure 43).

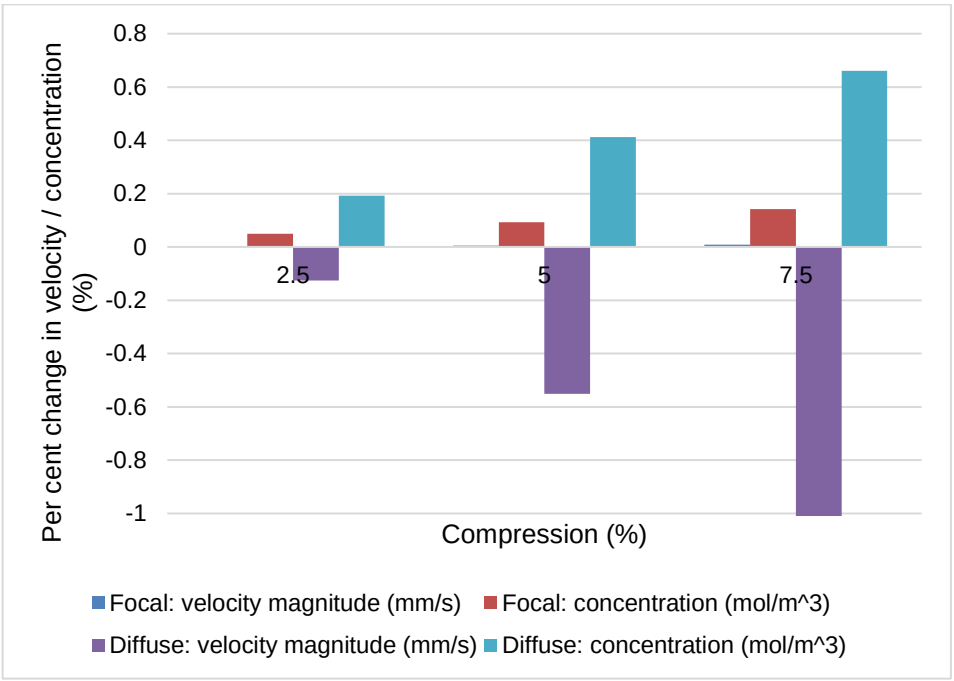

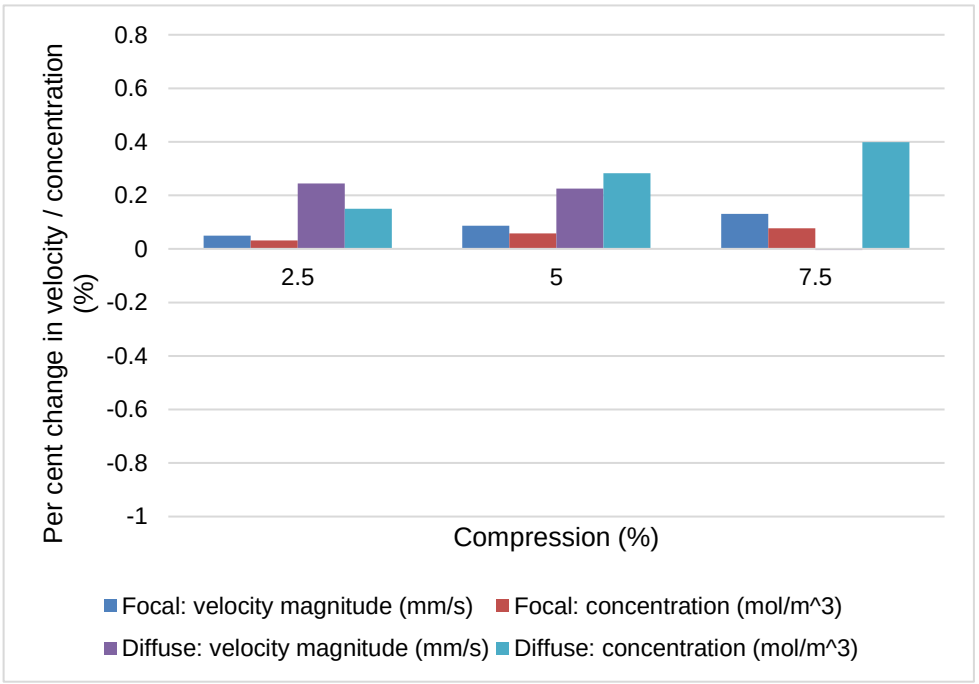

Figure 43: Fluid outputs of the white matter (a) and grey matter (b) response during increasing posterior compression from 2.5-7.5% under both focal and diffuse compression injury profiles.

Focal injury caused a continual, slow increase of blood velocity and oxygen concentration in both white and grey matter but both <1% change. Diffused

injury caused a decrease in white matter blood velocity as early as 2.5% compression and reached a maximum of 1% blood velocity decrease at 7.5% compression. Concentration increased in white matter relative to this. Grey matter conversely displayed a slight increase in velocity at milder compressions but then decreased to just below its baseline value at 7.5% compression. It can be assumed posterior injury does not have a significant effect on the underlying vasculature as it does not disrupt any core vessels but it does predominantly affect white matter dorsal columns, which aligns with the literature [67]. The data could infer that white matter velocity decreases by re-circulating blood to the grey matter, so the grey matter maintains its velocity and oxygen concentration and is only affected above a certain threshold. However, a decrease of 1% velocity across the white matter is unlikely to elicit the decreased vascular response in grey matter.

However, the increase in white matter concentration does align with the behaviour of the oxygen extraction rate, in that diffuse injury causes higher consumption rates and white matter presents with higher consumption in both injury profile models (Figure 44).

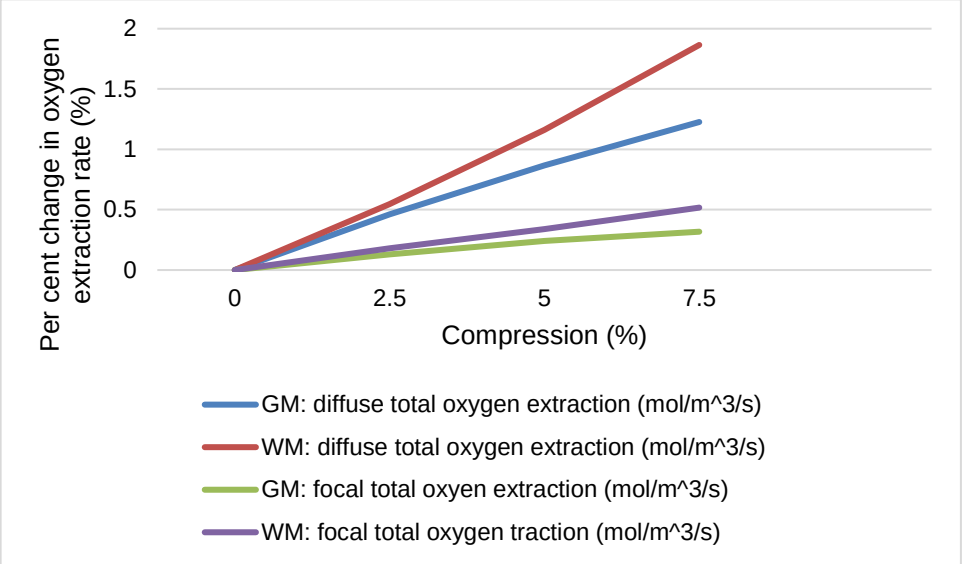

Figure 44: Oxygen extraction rate of the grey and white matter under diffuse posterior injury conditions.

White matter had two-fold extraction rates than that of grey matter; the increased oxygen extraction rate was attributed to the decreased tissue velocities and was viewed as essential to maintaining oxygen concentration.

5.1.4 Summary of blood and oxygen data

As a summary of the fluid data:

- Anteroposterior injury caused an increase in both blood velocity and oxygen concentration in both matter types during both injury scenarios. Grey matter velocities decreased below baseline at 10% compression. White matter experienced a continued increase in velocity under direct compression. The white matter had a higher oxygen extraction rate and therefore oxygen concentration than grey matter. The behaviour of the

white matter is believed to maintain the balance of its vascular system under mild compression. Focal injuries had negligible effect.

- In anterior injury, the dependency of porous system governance was highlighted during compression of the anterior spinal artery. Both tissue types displayed a decrease in velocity magnitude from 2.5% compression in both focal and diffused injury. Concentrations decreased below baseline at 7.5% compression but remained close to control conditions. Oxygen extraction rate correlated to this, an increase in consumption was seen until 5% during diffused injury which decreased below the baseline at 7.5% compression. Focal compression caused a decrease in oxygen consumption from 5%. Thoracic cord sensitivity to anterior injury was validated; the 5-10% compression zone should be further investigated to ascertain if there is an early onset of hypoxia under mild ischemic conditions.

- Posterior injury caused a decrease in white matter blood velocity coupled to an increase in concentration and increased oxygen extraction rate. Grey matter experienced slight increases in velocity and concentration but velocity decreased below baseline at 7.5% compression. Preservation of grey matter concentration was assumed to take place due to the decreased velocity in white matter but increased oxygen extraction rates in both tissues. Focal injuries cause negligible effects to the vascular system under posterior injury.

- The velocities and concentrations output were not representative of ischemia or hypoxia (~70% threshold) but do indicate changes to the vascular behaviour at much milder compressions than any reported to date.

- The data is in agreement with the trend that oxygen consumption increases as an early response mechanism to ischemic injury [18] and is a valid indicator of injury progression.

It could be hypothesised that anteroposterior injury triggers early vascular pathophysiology at compressions of 10%; the anterior vascular injury threshold may be as low as 2.5% compression and posterior vascular injury may take place at compressions above 7.5% but further work would be required to confirm these response profiles.

It has been seen *in vivo* that in the early stages of chronic compression, a reduction in blood flow is seen which increases internal pressures and causes the spinal tissue to swell; the lack of blood supply decreases the density of microvessels at the lesion site [205]. Clinical studies correlate a decrease in spinal canal diameter with decreased spinal cord blood flow, predominantly assumed as driven by compression of the anterior sulcal and grey matter arteries in anterior injury, which agreed with the data presented here [18]. However, studies have also found an increase in angiogenesis in neighbouring spinal tissue, assumed as compensatory for the localised ischemia and resultant hypoxia [83], which is assumed to have taken place in the anteroposterior injury data presented here. From a temporal perspective,

dorsal columns experience injury first and the disruption of grey matter follows, which was represented in the posterior injury model presented here [13]. The study presented here does not account for temporal changes, but the increase in static deformations could act as a proxy for an increase in severity over time.

5.2 Spinal tissue behaviour

With regards to the mechanical response of the spinal matter and vascular networks, stress response is also investigated at each parameter.

For all compressions, the mechanics experienced represented very low stress profiles, most tissues behaved similarly in terms of scale of stress experienced and that all stress profiles were exacerbated in the diffused injury scenario.

5.2.1 Anteroposterior injury

Under anteroposterior compression of the grey matter, the maximum von Mises stress of grey matter was doubled in diffused injury when compared to focal injury (Figure 45).

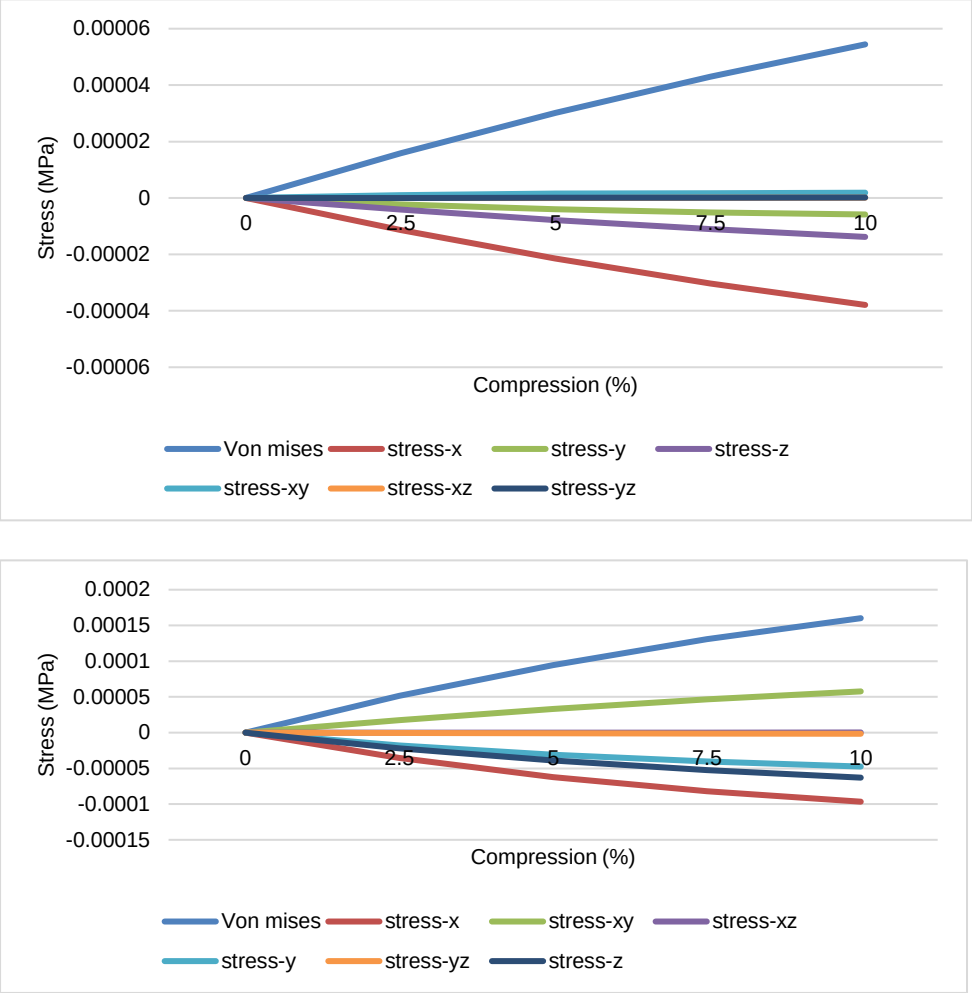

Figure 45: Stress development in the grey matter under increasing anteroposterior compressions (0-10%) during focal (a) and diffuse (b) injury.

Focal injury indicated higher tensive stresses in the stress-x direction, likely due to localisation over a smaller spread of 2mm, which would contribute to the overall von Mises volume average for the grey matter. Similar behaviour was observed for focal injury in the white matter. However, white matter behaviour under diffused injury showed an inflection in stress experienced at 7.5% compression (Figure 46).

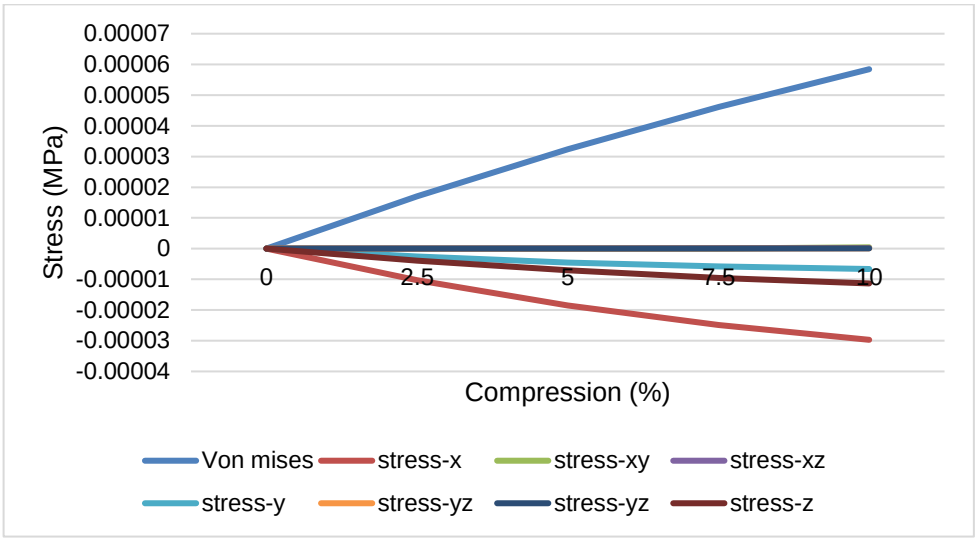

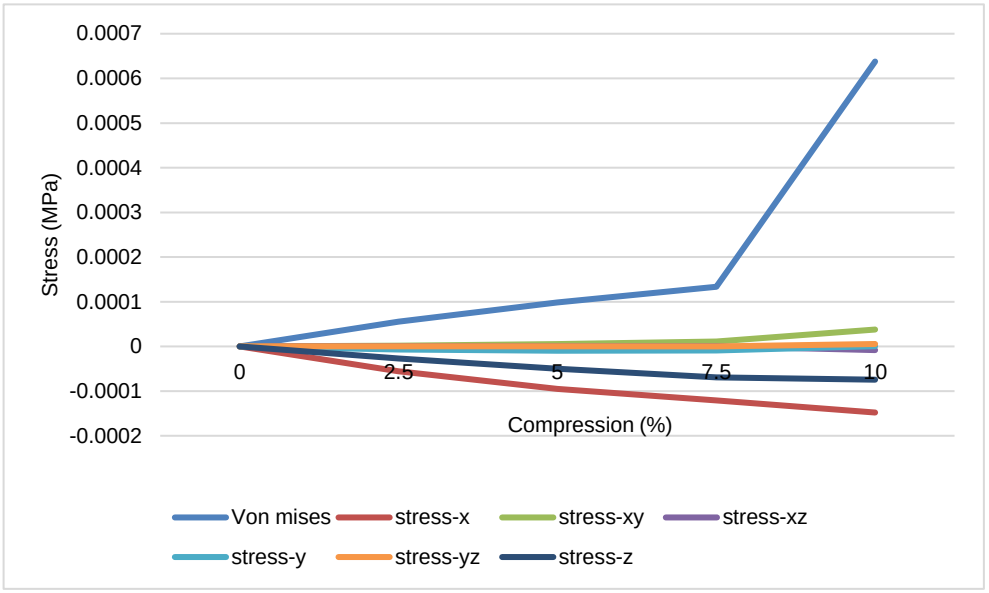

Figure 46: Stress development in the white matter under increasing anteroposterior compressions (0-10%) during focal (a) and diffuse (b) injury.

The response of tissue at this strain was visualised for analysis of internal cord behaviour (Figure 47):

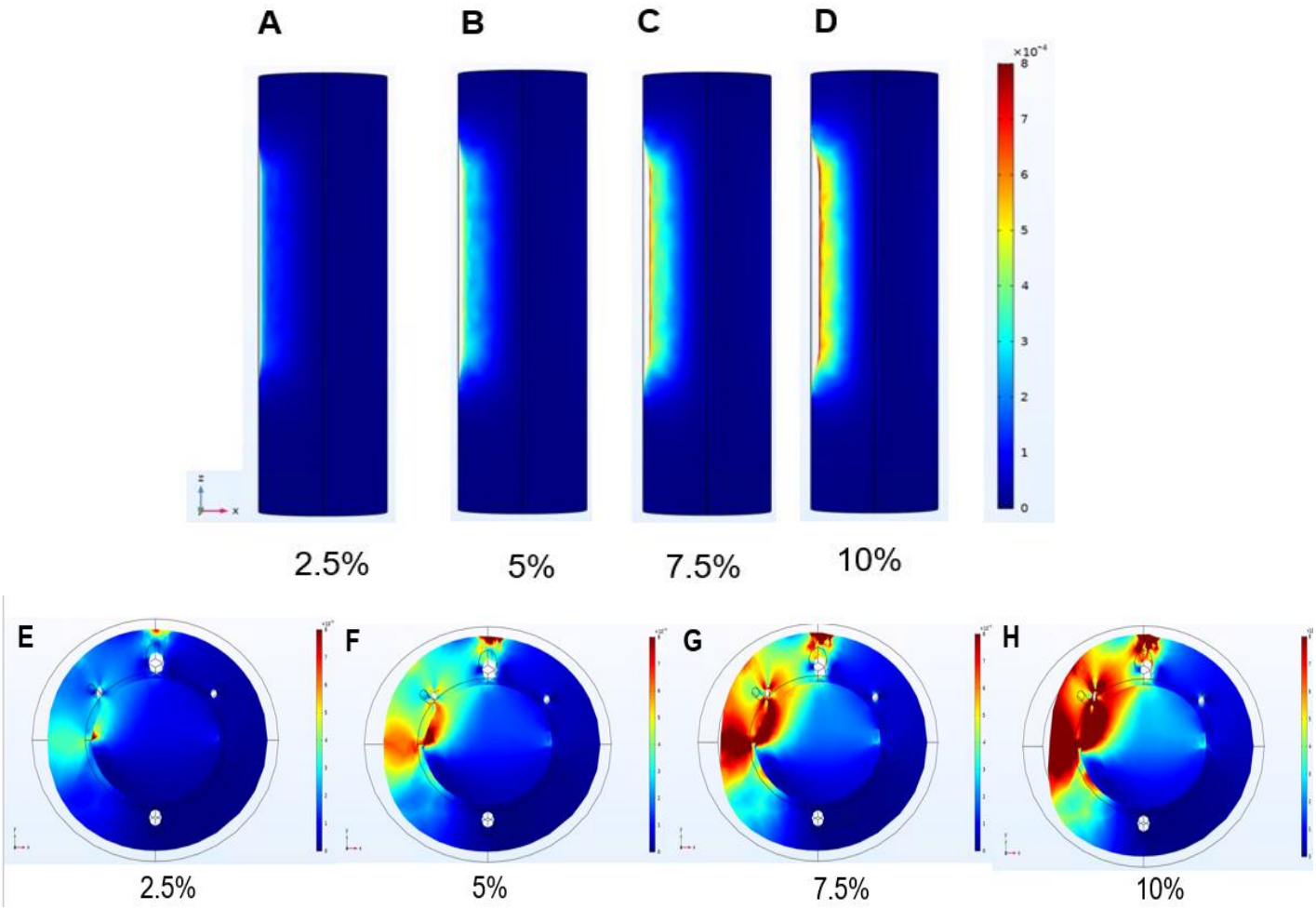

Figure 47: Von Mises stress plots of spinal tissue under diffused anteroposterior compression. Colour plot range = 0-10^{-4} MPa. Sagittal plots (a-d) are explored by transverse sections (e-h) from the injury epicentre (z=0).

Sharp increases in von Mises stresses are observed at the white-grey matter boundary on the compressed anteroposterior side of the spinal cord. Higher stress zones (coloured red) in the white matter at the injury epicentre and lateral column of the grey matter spreading to the left posterior spinal artery are likely indicative of the inflection in the stress data. With increasing compression, stresses transfer through the white matter into the grey matter. The erratic placement of stresses through the tissue is likely due to discrepancies in quality of elements in close proximity to small vessel

structures with denser, localised meshes. Therefore, the von Mises stress inflection was not assumed as contributory to the fluid pathophysiology.

5.2.2 Anterior injury

Under anterior compression of the grey matter, the maximum von Mises stress was lower than anteroposterior compression. However, focal compressions of grey matter exhibited similar increases in von Mises and stress-x components to that of anteroposterior injury (Figure 48).

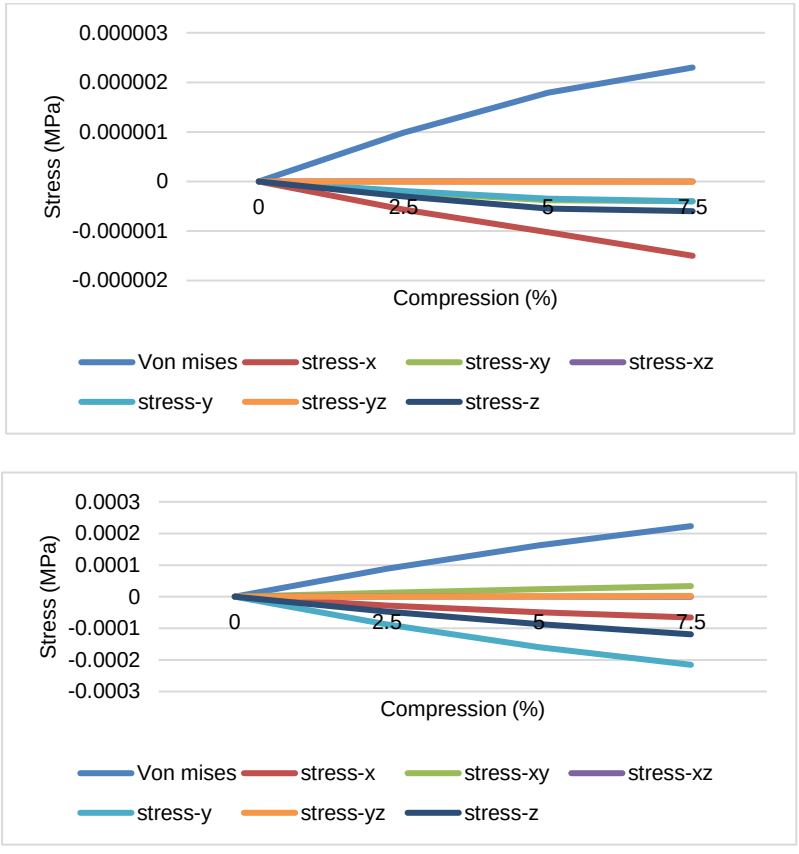

Figure 48: Stress development in grey matter under increased anterior compressions (0-7.5%) during focal (a) and diffuse (b) injury.

Grey matter experienced a 100-fold increase in stresses during diffused injury when compared to its focal profile. Tissue stresses maintain a steady increase as compressions increases, so could linked to the decreased blood and oxygen capacity; similar diffused profile stresses of ~0.0002MPa elicited a mild decrease of blood velocity in anteroposterior injury. Stress plots were visualised to understand the tissue response to focal injury (Figure 49).

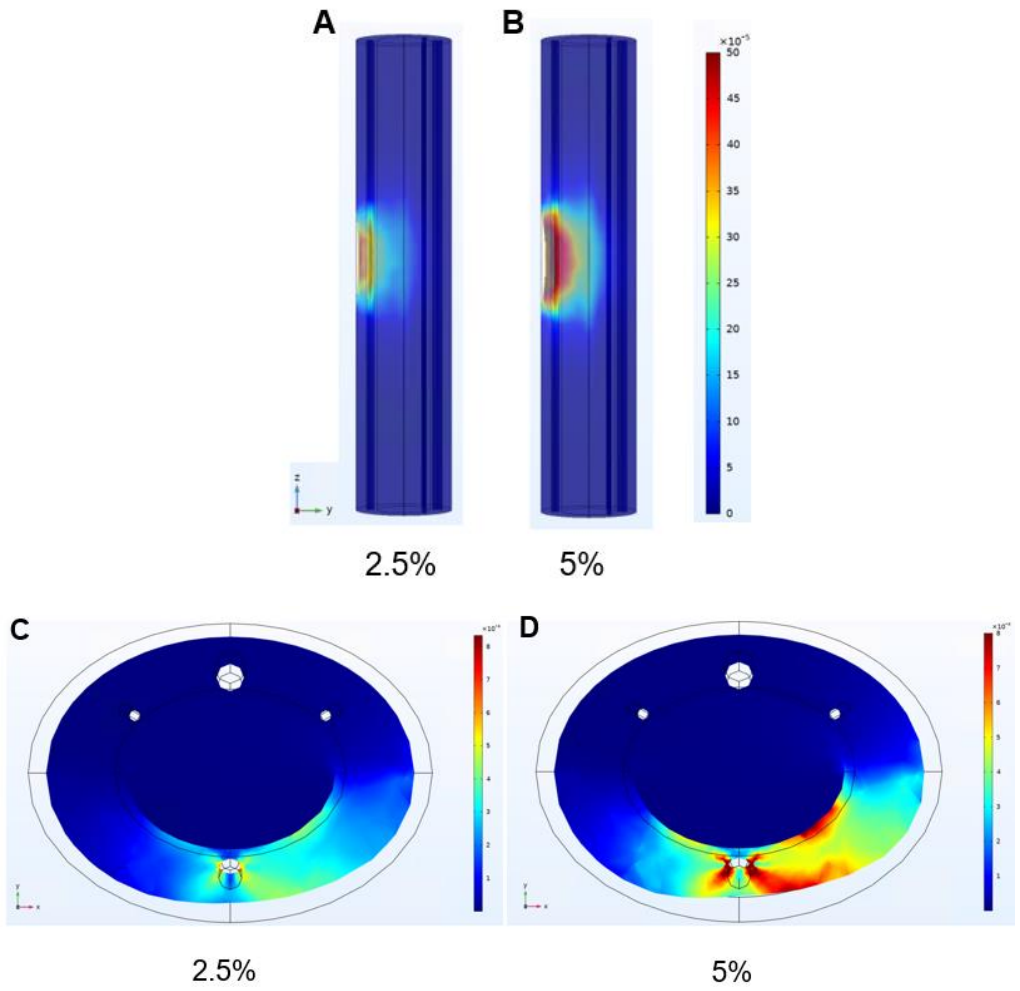

Figure 49: Von Mises stress plots of spinal tissue under focal anterior compression. Colour plot range = 0-10^{-5} MPa. Sagittal plots (a-b) are explored by transverse sections (c-d) from the injury epicentre (z=0).

Similar to the anteroposterior scenario, higher stresses were visualised around the zone of compression spreading into the tissue (y-direction) plus harsher

stresses at the ASA boundaries. White matter experienced a four-fold increase in von Mises and principal stress components during diffused injury (Figure 50).

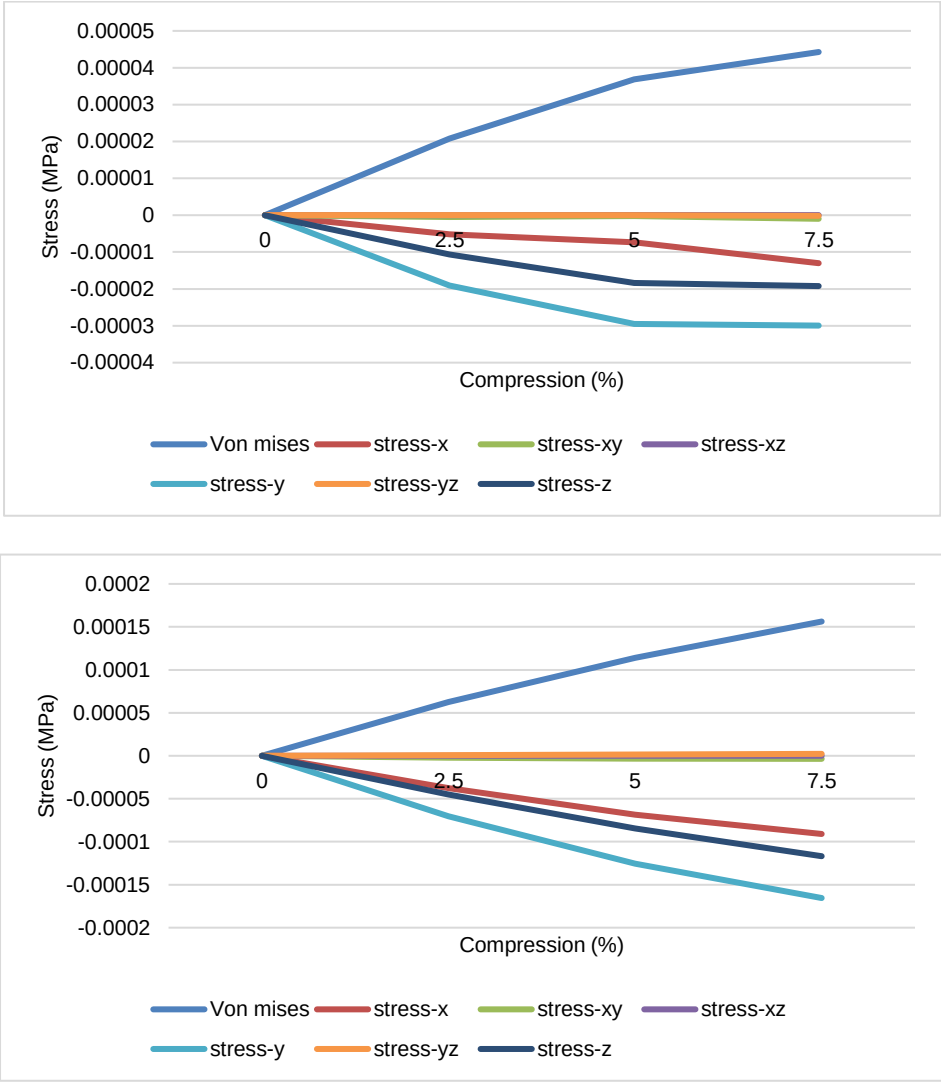

Figure 50: Stress development in the white matter under increasing anterior compressions (0-7.5%) during focal (a) and diffuse (b) injury.

Visualisation of internal stress was done again to understand effects of stress during diffused injury (Figure 51).

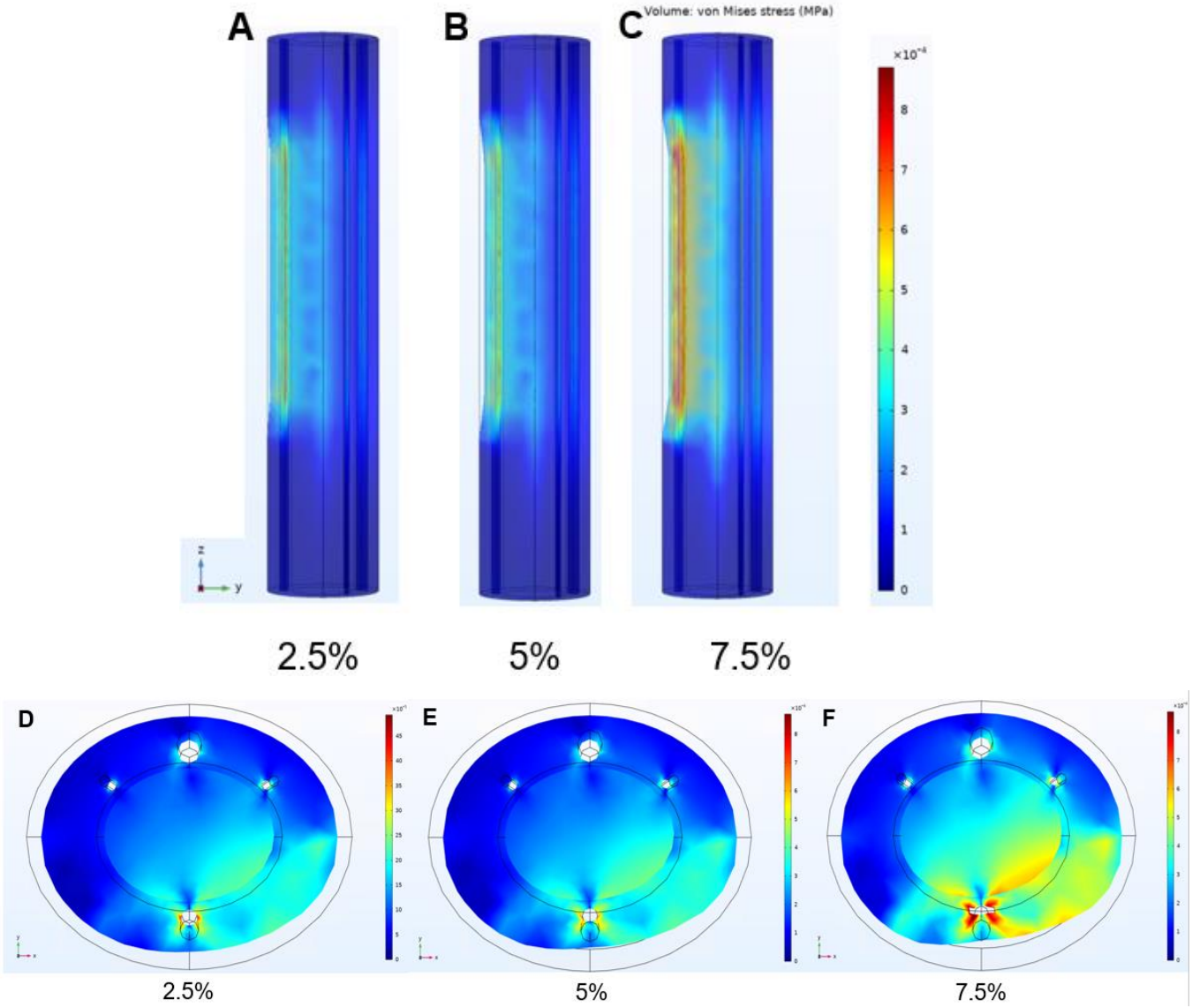

Figure 51: Von Mises stress plots of spinal tissue under diffused anterior compression. Colour plot range = 0-10^{-4} MPa. Sagittal plots (a-c) are explored by transverse sections (d-f) from the injury epicentre (z=0).

The highest stresses are seen at where the blood vessel boundary due to compression of a narrower region - flattening of the ASA can be seen in 51f as stresses spread into the grey matter. Higher von Mises stress is primarily seen in the ventral horns and anterior corticospinal tract and a spread of stress

moves through the spinal segment under increased compression, which agrees with the literature [42].

5.2.3 Posterior injury

Under posterior compression of the grey matter, focal injury was again causative of very low stresses in the cord. The maximum von Mises stress reached ~0.0002MPa in the diffuse injury model which was 2.5x higher than focal injury (Figure 52).

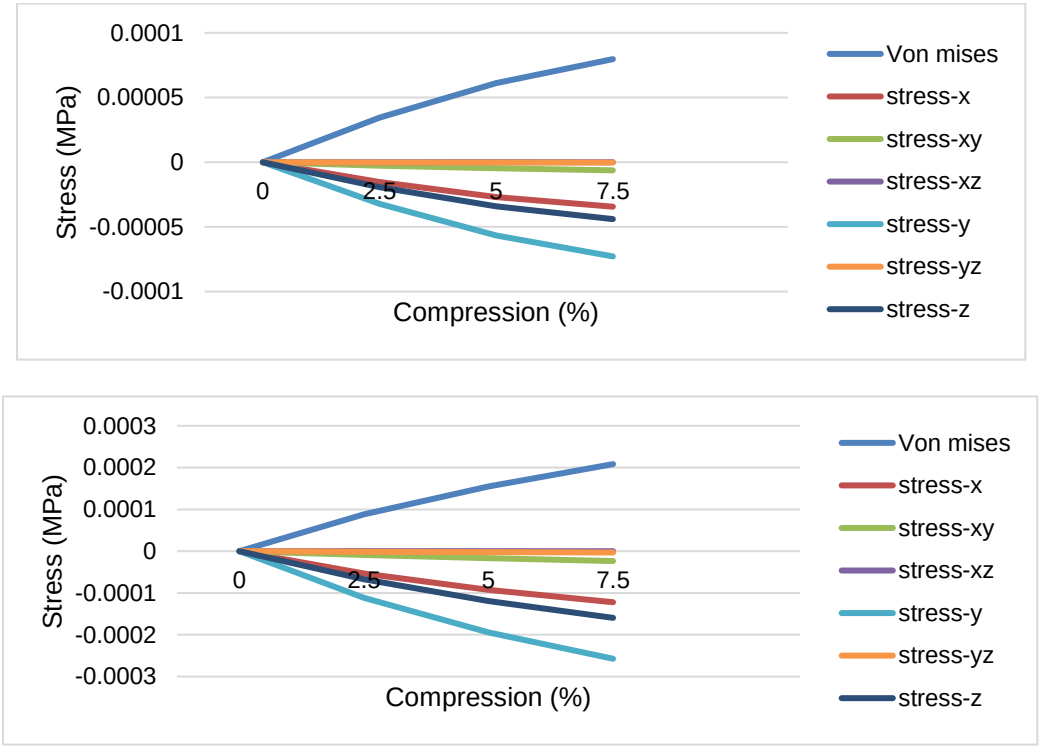

Figure 52: Stress development in the grey matter under increasing posterior compressions (0-7.5%) during focal (a) and diffuse (b) injury.

White matter also experienced 50% lower stresses in focal compression. However, diffused compression caused high inflections in stress at 7.5% compression, almost 75-fold that of grey matter (Figure 53).

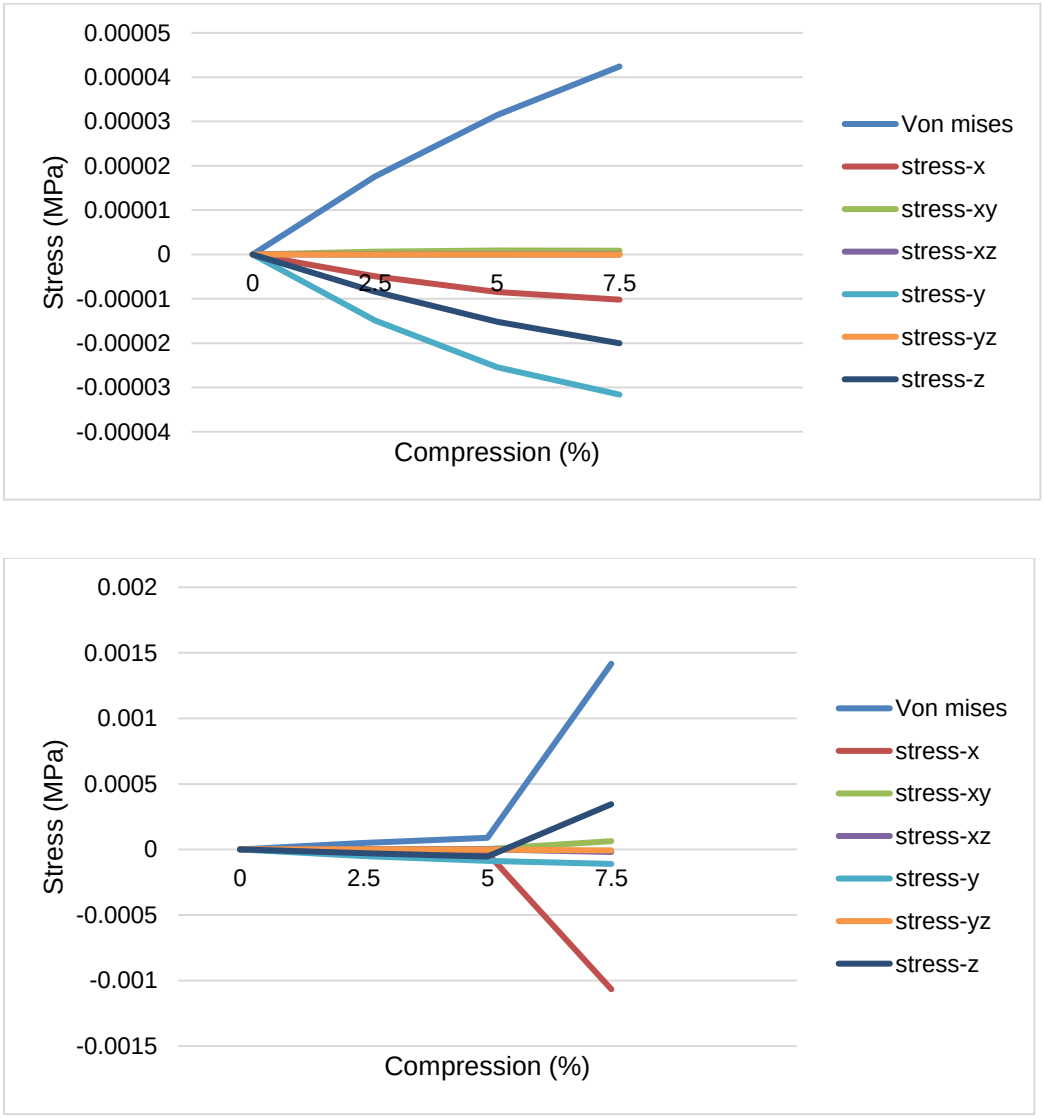

Figure 53: Stress development in the white matter under increasing posterior compressions (0-7.5%) during focal (a) and diffuse (b) injury.

The sharp tensive increases in the stress-z direction and compressive decrease in the stress-x direction infer lateral spread of the tissue. Visualisations of the internal tissue stress are as below (Figure 54).

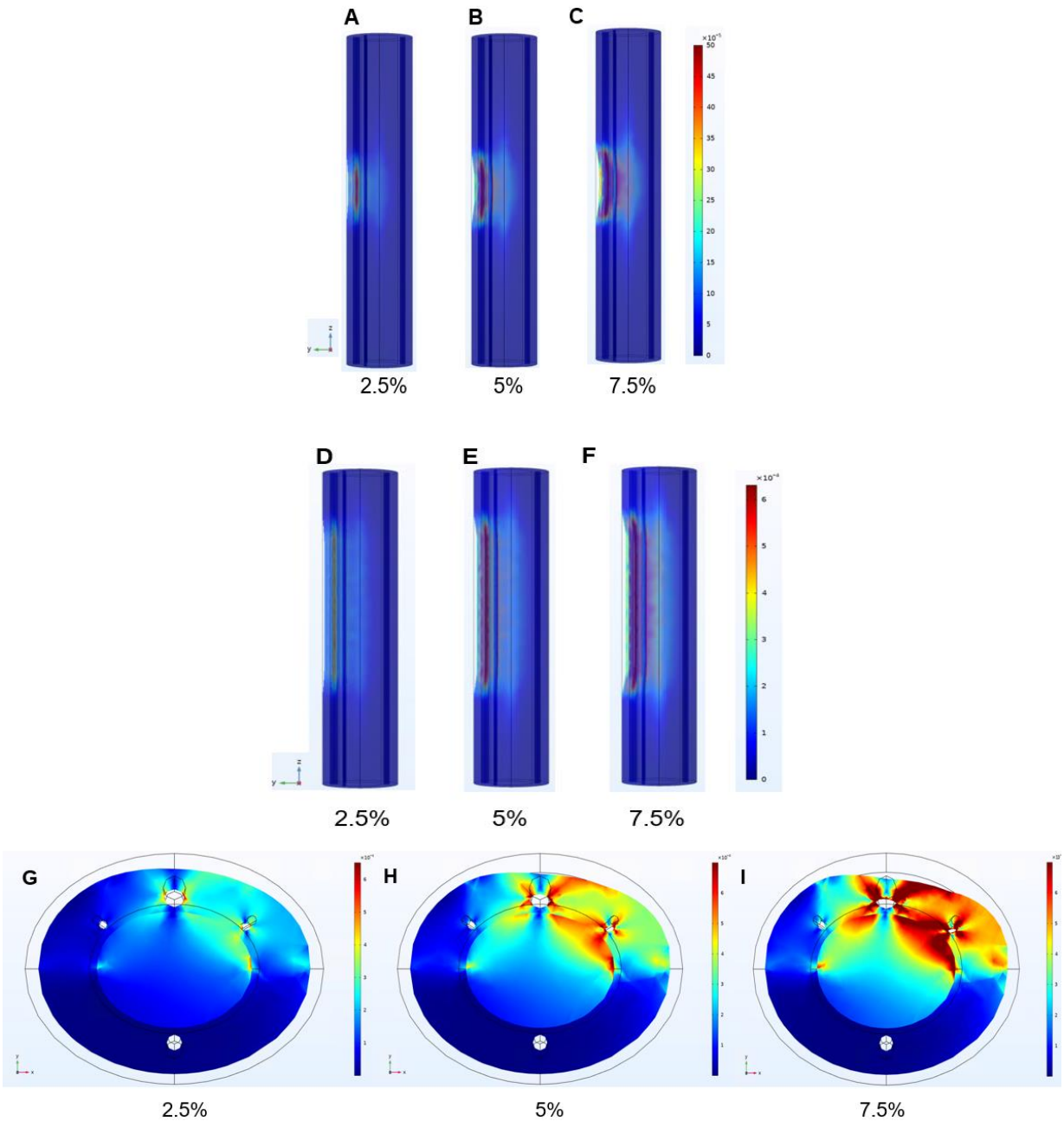

Figure 54: Von Mises stress plots of spinal tissue under focal (a-c) diffused (d-i) posterior compression. Colour plot range = 0-10^{-4} MPa. Sagittal plots (a-c) are explored by transverse sections (d-f) from the injury epicentre (z=0).

This is similar to the behaviour seen in the anteroposterior model and could be attributed to high stresses around the small artery geometries. It should be considered that the mesh was close to inversion due to the blood vessel positionings as the model could not simulate strains above this threshold. Stresses are much higher at the vessel boundaries and at the dorsal columns where the grey matter boundary is built into the model, which does reflect data from an ischemic model that showed initial damage to the dorsal columns before spread into the grey matter laminae [206].

5.2.4 Summary of spinal tissue behaviour

The solid data presented here indicates much lower stress profiles than previously reported for deformations up to 10%, which have reached 0.2MPa at the compression epicentre [26]. However, data did align with a 3-D finite element model that simulated NT-SCI as static compression and found that cord stresses were extremely low (near zero MPa) under 10% compression, with a slight increase at 20% compression [202]. The stress plots trends were in agreement that mild compression damage is predominantly situated within the dorsal horn [26]. Damage to the dorsal horn is understood to take place early in the pathophysiology of NT-SCI due to assumed preservation of the ventral horn that has much greater metabolic needs [67].

As a summary of the response of spinal tissue to mild compression:

- The stress profiles of grey and white matter were similar in anteroposterior injury between both injury profile groups except an inflection in von Mises stress during 10% diffused strain in white matter.

- Anterior diffused injury caused 100-fold increase in grey matter maximum von Mises stress and a four-fold increase in white matter maximum von Mises stress over focal injury stresses. Stresses were similar between the two tissue types.
    - Anterior compression showed particularly high stresses in the ventral horn column and corticospinal tract. This could be attributed to flattening of the ASA and associated localised stresses.

- Posterior injury produced higher stresses, particularly in the white matter which experienced 75-fold higher stresses over that of grey matter in the diffused injury scenario. The contour plots indicate much higher stress distributions, but this is more likely due to unreliable mesh quality in close proximity to the three posterior vessels. Posterior and anteroposterior diffused compressions indicated white matter was prone to compressions in the stress-x component, indicating lateral spread of tissue.

5.2 Results chapter summary

The key trends to take away from the parametric simulations of injury severity, location and profile are:

- Changes to blood flow and oxygen transport were seen at compressions prior to the assumed threshold of NT-SCI of 30%, which infers that vascular pathology is effectual earlier in the injury process.
- Diffused injuries that compress multiple segments are causative of detrimental vascular response. The effects are worse than in focal, single segment injuries.
- Anterior injury is causative of the most severe vascular response in terms of tissue velocity speeds with decreases of up to 15% observed. Effect of vascular response between 5-10% should be investigated further to elucidate any thresholds causative of a decrease in oxygen extraction rate, indicative of worsened injury and hypoxia.
- Anteroposterior and posterior injuries are causative of mild effects and do indicate detriment to white matter before affecting the grey matter. Compensatory re-rerouting for these locations should be investigated further.
    - Compression of white matter fibres may have increased the diffusivity potential of the porous transport model and be an explanation for increased concentrations and oxygen consumption despite decreased velocities.
- Degree of compression appears to have stronger correlation to oxygen extraction rate over average tissue concentration (i.e. hypoxia), which is in agreement with Ellingson *et al*. [18].

Chapter 6

Discussion and conclusions

The work presented in the thesis helps to better understand the relationship between compressive mechanics and blood and oxygen dynamics in sub-clinical, asymptomatic NT-SCI. The thesis question was investigated through developing the computational model to analyse three injury variables: severity, location and shape profile. Mild compressions were simulated to understand how mechanical stresses develop across different aetiology profiles and affect blood flow behaviour and oxygen transport in the spinal tissues.

6.1 Core findings

In developing the mathematical model and numerical implementation of the problem into a computational model, the following optimisation steps were essential as inclusion criteria for this work:

- Inclusion of Brinkman's model to model intermediate vascular network flows.
- Material properties of the porous medium representative of the spinal cord grey and white matters. Isotropic permeabilities representative of previous cerebral vascular network models were applicable [136]. Permeability was a key determinant in model behaviour, porosity was not as effective.
- Modelling oxygen consumption as a function relative to available concentration – uniform consumption models forced hypoxic scenarios and would not allow for compensatory mechanisms.

- Investigating the effect of injury profile representative of different NT-SCI aetiologies relative to the trends seen *in vivo* [21] had large effects on vascular response to injury.

On inclusion of these criteria in the mathematical model and numerical implementation, parametric analyses of NT-SCI severity, profile and location were undertaken, as presented in chapter 5.

6.1.1 Injury severity

It was assumed that white matter would be affected most at lower compression thresholds and the dorsal horns would be injured initially, as is described in the literature symptomatically as early sensory dysfunction [80][207]. It was expected that blood velocity would gradually increase, due to narrowing of primary vessels under compression, which would increase internal microvascular network pressures and velocities. With this, oxygen concentration and oxygen extraction rate were also expected to increase as the volume of blood available for oxygen exchange increased to compensate for flattened vessels. A decrease in blood velocity and oxygen concentration was expected to take place quickly at higher degrees of compression above an unknown threshold - potentially above the 10% compression within the scope of this study - as the literature had indicated strains above 20% as the estimated threshold that trigger a reduction in spinal perfusion [64][65]. This inflection point would take place after compensatory increases in vascular response due to increased pressure gradients under external forces.

These hypotheses were correct in terms of increased velocity, oxygen concentration and oxygen extraction rate at low compressions, but the identification of thresholds at which early ischemic responses are triggered under mild compression took place at thresholds well below those hypothesised in the literature.

Grey matter velocity magnitudes decreased below the baseline at 10% anteroposterior compression; white matter is assumed to have compensated for its compression by increasing its oxygen extraction rate, velocity profiles and therefore oxygen concentration, maintaining homeostasis in the cord vascular network.

Both grey and white matter velocities were decreased below the control scenario from 2.5% in anterior injury. A decrease in oxygen concentration below baseline took place at >5% compression, which aligned with a decrease in oxygen consumption by the tissue.

White matter experienced lower velocities coupled to increasing concentrations during posterior injury, whereas in anteroposterior injury, velocities and concentrations increased concurrently. Both injury types experienced an increase in oxygen extraction rate of ~2%. The increased blood availability in anteroposterior injury may reflect the delayed decrease in grey matter velocities at 10% strain when compared to a decrease at 7.5% strain in posterior injury, where less compensatory blood supply was available due to direct compression on the posterior arteries Both posterior and anteroposterior compression realistically had negligible effect on grey matter (<1% deviations from baseline), which aligns with the literature [20].

6.1.2 Injury profile

With regards to solid mechanics, no papers to date have researched the change in fluid and oxygen mechanics relative to varying injury aetiologies, despite being inferred as a core driver of NT-SCI [208]. It is understood that an inherent limitation when investigating injury profiles is the underlying spinal anatomy. Previous solid mechanic models had found that diffuse injury – such as disc herniation - produced worsened outcome (due to spread of injury across multiple spinal segments) [23]. On increase of strain, stress transferred through an individual spinal segment from white matter to grey matter, before spreading to neighbouring segments (z-direction spread from epicentre at z=0), which agreed with the trends observed here [26]. Similarly, focal compressions mainly affected the afflicted segment under compression with higher localised stresses, which agreed with data trends reported here.

It was therefore assumed that, similar to the reported solid mechanics model, diffused compression would produce worsened vascular outputs due to its spread across segments, with particular affect during anterior injury due to the importance of the primary anterior vessel. Focal compression was predicted to have localised affect that would be negligible until above the known symptomatic 30% reduction in diameter. These hypotheses were proven as correct. Stresses were similar across injury types in both white and grey matter with higher stresses experienced in all diffused injury scenarios. The ratio of increased stress response varied with injury and was most pronounced in the grey matter of anterior injury with a 100-fold increase in stress experienced

during diffused injury compared to focal injury. In posterior injury, the white matter experienced a 75-fold increase in maximum von Mises stress when compared to grey matter during the highest degree of compression. This reflects the effect of injury profile on locations and the underlying structures and anatomy.

However, in the white matter, diffuse anteroposterior and posterior injuries displayed significant uplifts in von Mises stresses at higher compressions – relative to the stress contour plot data, this was assumed due to mesh irregularities when compressions took place beside the smaller artery geometries. There have been no reports of the spinal matters rupturing at stresses as low at those derived from the model, therefore those data points are deemed unlikely as contributors to the pathophysiological processes.

6.1.3 Injury location

In order to account for the difference in anatomy and feeder vessel importance, location was investigated. It is generally understood that compression of the anterior spinal artery is most detrimental in thoracic NT-SCI, due to the aforementioned lack of collateral vessels and its significance in providing two-thirds of the blood supply of this region [35]. A study that investigated the effect of compression on the anterior artery and its sulcal network was Alshareef *et al*. [19], which validated that anterior compression was resultant in the highest decrease in blood flow. However, the model did not account for any other vessel networks in the spinal tissue (i.e., posterior, capillaries, etc). Therefore, the model presented here investigated other locations and the effect of

compression on the respective feeder vessels. It was assumed anterior injury would have the lowest tolerance and would show the greatest detriment in blood flow and oxygen transport response under a diffused injury scenario. The data inferred compressive effect on vasculature from the mildest compression at 2.5% compression and caused decrease in velocities by up to 15%. It was assumed that anteroposterior injury would decrease blood flow and oxygen transport to a lesser degree, with only slightly worsened outcomes in diffuse injury – this was generally correct but white matter displayed higher sensitivity to anteroposterior diffused compression than expected. Posterior injury was again assumed to suffer most detriment in diffuse injury cases, but to the lowest extent as it does not have any core contributing vessels in the region (posterior spinal vein only). Similar to anteroposterior, this was correct aside from a higher sensitivity of white matter to compression, but vascular changes in both injuries remained <2% so would be negligible in a real-world scenario.

6.2 Comparisons with the core literature

A key comparator paper in the literature simulating spinal compression to ascertain changes to fluid flow identified extreme drops in flow rate even under strains of <10% [19]. Under anterior compression, 6.5% dural occlusion decreased anterior spinal artery flow by approximately 30% and branching sulcal arteriole flow rates by ~5%. The data presented here aligns with the decrease in arteriole flow but not to the extent of velocity decrease in the ASA.

However, blood flow rate increased slightly in the ASA under milder compressions before eventually declining at higher degrees of compression, similar to the velocity data reported here. The study reported that posterior loading (6% occlusion) decreased arteriole branch flow rate by ~30% and ASA flow rate by ~5%, which disagrees with the data derived from the thesis model. Anteroposterior loading (9.65% occlusion) reduced branch flow rate by 30% and the ASA by 50%. Again, velocity decreases of this magnitude were not observed in the model developed here. The [19] data would infer a severe prognosis for milder injuries, which is not currently reported clinically or elsewhere in the literature. The high drops in blood flow rates are likely because vessels were presented as isolated cylindrical geometries with limited connectivity to only one sulcal network system and no capacity to re-route.

The model data presented here did, however, correlate with that of an *in vivo* study performed in monkeys, when moderate anterior compression caused microvascular deformation and a decline in perfusion in the grey matter, without a significant decrease in ASA diameter or flow [77]. Similarly, a rabbit study found that grey matter vessels had an exacerbated decrease in perfusion rate compared to the ASA under anterior compression [209]. Another study reported that anteroposterior compressions did not affect grey matter microvasculature but anterior compressions of 2mm (10% strain) were causative of occlusion of the adjacent sulcal arterioles and intramedullary branches into the grey matter [20] – this agrees with the anteroposterior and anterior data trends derived from the thesis model. Posterior compression had nominal effect on fluid or oxygen output but was assumed to affect the dorsal microvasculature and therefore lateral columns due to flattening of the cord in

the direction of compression and compensatory lateral bulging, which is in agreement with the stress plots presented in chapter 5.2.3 [20]. Clinical studies of CSM have highlighted compaction of fibre tracts under compression which alters the diffusivity profile of oxygen in the system. Neurological dysfunction is hypothesised as due to disruption and degradation of these fibre tracts at later stages of injury, but it could be assumed that an earlier response is seen through an increase in local fibre re-modelling, which correlates to an increase in inflammation and oedema [44] which is known to trigger an increase in oxygen extraction rates. Future work should investigate this relationship.

A transient ischemic model of the rat spinal cord (balloon catheter model to occlude the subclavian artery) does not reflect compression but is indicative of mild, low-level ischemia and reflects the trend that the dorsal horns are affected first; in particular, the laminae V-VII experience a loss of interneurons but neurons in ventral horns of the grey matter (laminae VIII-X) are not affected [206]. This agrees with the fluid model velocity plots for anteroposterior and posterior compressions. Other traumatic studies that have modelled mild traumatic SCI indicated minimal neurological dysfunction when SCBF is reduced by 45%, which agrees with the known ischemic and therefore symptomatic threshold of 70% [210] – the data here indicate that mild compressions do not elicit decreases in blood flow to the point of ischemia or symptom manifestation. However, on extrapolation of the decreased velocity rates in grey matter under diffused anterior injury (15% loss of blood velocity under 7.5% compression), the ischemia threshold as 70% loss of perfusion in arteries and 50% loss of perfusion in microvasculature is likely to be exceeded at around 35% strain for the arteries and at 25% strain for the sulcal

microvasculature, which correlates to the commonly understood 30% symptomatic threshold from *in vivo* studies [65], [21].

Clinical reports of patients with CSM indicate lower degrees of compression generally have higher blood flow rates and better neurological outcomes, as expected relative to the literature. However, spinal cord hypoxia is not correlated to the degree of compression, but increased oxygen extraction rate is. Patients with higher T2 hyperintensity signals (relative to degree of stenosis) tended to present with >10% oxygen extraction rates and had the worst neurological functionality [15]. Data from this thesis agrees with that trend and future clinical work should ascertain the mechanical thresholds at which changes in oxygen extraction rate trigger hypoxia and progression of NT-SCI. Anterior injury indicated a decrease in consumption rates above 5% diffused compression when tissue velocities dropped by ~8%. Ideally, the study would investigate the changes to consumption rates over chronic compression timescales to understand the relative thresholds for increased consumption before the decrease that leads to hypoxia, but the model was limited in this functionality.

With respect to the shape profile, it was known that under moderate compression, tissue stress varies and the response is dependent on the spinal segment anatomy and profile of the compression, which therefore alters the symptoms experienced [26]. The Kim *et al*. [199] paper investigated injury profile and indicated that a maximum von Mises stress of 0.004-0.006MPa was seen at 15% compression, with tissue response dependent on injury

profile and shape. Injury profiles of 4mm compared to prior groups (1-3mm) showed the highest von Mises response that varied with shape (fused or non-fused ligament representations), but shape alone (curvature of injury deformation) was not a primary driver in stresses experienced by the tissue. The thesis data alluding to worsened outcomes during diffused injury align with this, as the fluid and solid manifestations of the injury profile varied with location and severity.

The Nishida *et al.* paper [26] simulated anteroposterior injury at 10% compression and reported that the cervical spinal cord experienced stresses at around 0.012MPa, which is much higher than the stresses presented here. The posterior white matter columns experienced the highest stress under anteroposterior injury which correlated to the thesis data [26]. The model from the literature applied a focal compression directly onto the spinal cord, with no protective tissues modelled. Under anteroposterior compression, the dorsal horn experienced most stress at 10%; followed by a spread into the lateral posterior funiculus, posterior and lateral funiculi and anterolateral funiculus and grey matter anterior horn at 20%; followed by all of the lateral grey matter and funiculi being affected at the respective 30% and 40% strains. During severe compression (40%), the variance in stress profile between segments was less than under mild (0-30%) compression, but such strains could not be emulated in this model. The stresses produced in this model are very low which correlate to the compression severities being applied and do correlate with data reported by Kato *et al*. [202] where spinal cord stresses were near zero MPa at 10% compression. Relative to the Levy *et al*. [23] paper, development of the stress profiles contributory to anteroposterior injury begin

at strains as early as 9% for focal and lateral injury types and 15% for diffuse injury types – the work presented here indicates that the microvascular response of NT-SCI may begin before these mechanical thresholds are met.

6.3 Limitations

The model was built with inherent assumptions that equally act as limitations, primarily in terms of material properties and assumed behaviours of the underlying mathematics. Protective geometries of the spinal cord – such as the dura and pia mater) were not included, which would alter the stress-response profile under compression, as described above relative to known data in the field [23], [199]. The dimensions of the geometry were derived from the literature, but more accurate representations could have been employed through 3-D reconstruction of microscopy images. The number of vessels was limited to the four core extraspinal vessels known to supply the lower thoracic cord [67] and therefore is limited in its ability to truly represent the circulatory spinal system. Similarly, the detail of geometry and size of the vessels required a denser mesh but ultimately the complexity of mesh had to be limited, relative to computational capacity.

The spinal cord is understood to have hyperelastic-viscoelastic material properties, derived from *ex vivo* studies. This model only employed linear elastic properties due to the complexity of the underlying maths and scale of computational capacity that would be required for accurate simulation.

However, these material properties align with prior solid mechanics simulation data used as comparables for the model [19], [153].

The porous model and its setup inherently assume transference of inertial forces from larger vessels into the porous microvasculature medium, which is governed by pressure-driven Darcy flows. In terms of modelling the vasculature as a porous medium, the nearest comparable is that of an ischemic brain model by Jozsa *et al*. [182] which modelled the brain as a multi-compartment porous network by attributing different permeabilities and behaviours to vascular regions. The model deployed here assumes different permeabilities between white and grey matter, with grey matter assumed to behave similarly to the arterioles in the brain and white matter relative to cerebral capillary permeability [136]. These assumptions likely do not fully translate into a rat model from human, nor do the brain parameters fully reflect spinal cord behaviour, as the brain has markedly more vasculature and more collateral availability under damage. To account for vessels of varying size dispersed randomly throughout the tissue, other porous compartments and mathematical requirements would need to be employed to simulate this accurately. The mode presented here applies gross permeability terms across the whole spinal matter instead of localising permeability relative to scaling of geometry in tissue and therefore changes in pressure and concentration gradients.

Other vascular models account for non-Newtonian properties of the blood, namely diffusion from plasma into vessels via the Hill equation and consumption rates relative to saturation and hematocrit, considered by the

Michaelis-Mention equation. Previous time-dependent brain models have employed saturation of vascular tissue to represent known saturations of arterioles (85%) and capillaries (45%) [129], wherein the liquid volume fraction is then calculated from the porosity and saturation so ties in with the blood and oxygen transport models. The oxygen model used was rudimentary compared to other advanced vascular models that exist in the literature. In particular, the oxygen consumption model was defined as a single sink term employed by a variable function based on blood velocity outputs, meaning a variable sink function represented venules throughout the tissue and was designed to only consume oxygen at or above the baseline assumed oxygen concentration, therefore the circulatory effects of the feeder vessels and porous network would account as an attempt to balance oxygen metabolism back to equilibrium. The intricacies of oxygen consumption modelling are more complex than this, plus it is known that excess consumption takes place during ischemia to provide for the surviving tissue, but the compressions required to elicit ischemia and therefore hypoxia were not modelled here to exhaustively test these parameters. Other oxygen transport models have employed stationary models that impose specific consumption constraints and neglect the non-stationary aspects of blood and oxygen exchange by accounting for hematocrit, oxygen saturation and therefore alter the consumption rate based on the availability of oxygen and blood flow over time [139], [142].

6.4 Future work

During non-traumatic compression, it was already known that a decrease in blood flow was a core aspect of the pathophysiology, assumed due to hypoxic biochemical and mechanical behaviours of the damaged spinal tissue and vasculature [13], [67], [80]. It has been understood that ischemia is defined as a 70% decrease in blood perfusion [18] and hypoxia is relative to each individual tissue type. Normal blood velocities for different tissue anatomies had also been reported (section 3.1), therefore the decrease in flow and concentration relative to increasing compression at different locations and injuries was investigated to find the transition point at which it could be assumed NT-SCI would occur to a detrimental level. The model presented here could only simulate compressions up to 7.5-10% but from extrapolating the data for anterior injury, vascular response to compression profiles of 25-35% should be investigated - it is expected that vascular disruption would be one of the early primary drivers of neurological dysfunction and not a secondary response as it is in traumatic SCI. However, the complexity of the fluid-structure mathematics, geometry scales and 3D deformations required were too complex to simulate larger deformations here.

As mentioned, the oxygen model and circulatory assumptions could account for changes in viable vasculature, plasma-capillary exchange, oxygen saturation and alterations to oxygen consumption and should be considered when modelling a time-dependent chronic compression model. From a solid mechanics perspective, poroelasticity could further elucidate on the changes to the microvasculature; extracellular space fraction is known to decrease as

tortuosity of spinal vessels increase as tissues experience compression, ischemia and hypoxia [181]. Modelling poroelasticity could enable investigation of fibre compaction relative to diffusivity of oxygen throughout tissue [44], which in turn would relate to changes in oxygen consumption rates. Understanding the thresholds at which these changes take place could bring further clarification to some of the trends discovered here, namely the changes in white matter behaviour in anteroposterior and posterior injury and in further elucidation of the rationale for the oxygen extraction decrease in anterior injury.

To broaden the dataset and understanding of the variation in NT-SCI, other injury profiles should be considered, such as hypertrophy of the ligamentum flavum (circumferential compression), lateral compressions and hopefully in the future, personalised compression profiles for conditions such as metastatic spinal cord compression (tumour morphology dependent, secondary bone fragmentation, etc). The model could utilise patient-specific geometry from experimental imaging reconstruction or from medical imaging – particularly as location and morphology of the cord segments would be a core aspect of prognosis. Personalised diagnostic pathways may become commonplace in the future by using *in silico* models coupled to patient-specific medical images - work has already started in compiling *in silico* datasets for brain infarction models for use in stroke clinical trials [136].

A core component of NT-SCI that was not modelled here was the timescale of injury. It is understood that non-traumatic injuries take place over long timescales which are inherently linked to functional outcome [1]. Clinically, NT-

SCI manifests over a period of months to years but this is not feasible or humane to emulate in an *in vivo* setting. Relative to injury timescales, three days in a rat is equivalent to approximately three months in a human [211] and it is known that recovery of rats plateaus 6-8 weeks after injury [212]. From a temporal perspective, studies indicate that neural damage is irrecoverable after 9-weeks of compression [45] and decreased area of the spinal cord is strongly correlated to decreased functional output scores [213]. In particular, in a chronic compression models emulating CSM, the diameter of the ASA was smallest after 42 days, which may indicate a temporal inflection point in terms of initiating the ischemia-hypoxia pathway [214]. The change in perfusion and oxygen consumption over time, relative to the aforementioned parameters, would be useful in determining better diagnostic thresholds and treatment process for potentially earlier interventions. In particular, thoracic, incomplete and non-traumatic injury decompression surgery outcomes are speculative, as there are higher complication rates due to the non-exact nature of the injury and sensitivity of the surrounding provisional vasculature [3]. Therefore, better diagnostic criteria could identify key intervention thresholds at earlier pathological stages.

6.5 Conclusions

An *in silico* model of NT-SCI in the lower thoracic spinal cord was developed to include the effects of perfusion and oxygen changes under compression. The model provided clarity on aspects of the pathophysiological mechanisms

that have previously been hypothesised as contributory in the development of NT-SCI:

- Diffuse injury profiles (affecting multiple segments) produce more detrimental effects in terms of vascular response blood velocity and oxygen metabolism, as well as in functional outcome of rodents. Focal injury did not elicit any substantial effects.

- Anteroposterior injury indicated vascular contribution towards injury development at 10% compression with affect in the grey matter and compensatory effects in white matter.

- Anterior injury indicated vascular contribution towards injury development at 2.5% compression in both matter types.

- Posterior injury indicated vascular contribution towards injury development from 7.5% onwards and at earlier thresholds in the white matter.

- From the extrapolation of anterior compression data – an estimated threshold at which ischemia may be triggered is between 25-35% compression for diffused anterior injuries that affect the essential ASA in the thoracic spinal cord.

- Further work should investigate vascular response at higher compression thresholds (20-40%) and should look to understand the

structural and behavioural changes in spinal matter fibres and the underlying microvascular networks.

Bibliography

[1] B. M. Davies *et al.*, “A New Framework for Investigating the Biological Basis of Degenerative Cervical Myelopathy [AO Spine RECODE-DCM Research Priority Number 5]: Mechanical Stress, Vulnerability and Time,” *Glob. Spine J.*, vol. 12, no. 1_suppl, pp. 78S-96S, 2022, doi: 10.1177/21925682211057546.

[2] S. S. Smith, M. E. Stewart, B. M. Davies, and M. R. N. Kotter, “The Prevalence of Asymptomatic and Symptomatic Spinal CordCompression on Magnetic Resonance Imaging: A Systematic Review andMeta-analysis,” *Glob. Spine J.*, vol. 11, no. 4, p. 597, May 2021, doi: 10.1177/2192568220934496.

[3] D. M. Molinares, D. R. Gater, S. Daniel, and N. L. Pontee, “Nontraumatic Spinal Cord Injury: Epidemiology, Etiology and Management,” *J. Pers. Med.*, vol. 12, no. 11, Nov. 2022, doi: 10.3390/JPM12111872.

[4] J. Šedý, J. Zicha, J. Kuneš, P. Jendelová, and E. Syková, “Rapid but not Slow Spinal Cord Compression Elicits Neurogenic Pulmonary Edema in the Rat,” *Physiol. Res*, vol. 58, pp. 269–277, 2009, Accessed: Jan. 23, 2018. [Online]. Available: www.biomed.cas.cz/physiolres.

[5] C. D. Fortin, J. Voth, S. B. Jaglal, and B. C. Craven, “Inpatient rehabilitation outcomes in patients with malignant spinal cord compression compared to other non-traumatic spinal cord injury: A population based study.,” *J. Spinal Cord Med.*, vol. 38, no. 6, pp. 754–64, Nov. 2015, doi: 10.1179/2045772314Y.0000000278.

[6] P. A. Kearney, S. A. Ridella, D. C. Viano, and T. E. Anderson, “Interaction of Contact Velocity and Cord Compression in Determining the Severity of Spinal Cord Injury,” *J. Neurotrauma*, vol. 5, no. 3, pp. 187–208, Jan. 1988, doi: 10.1089/neu.1988.5.187.

[7] B. Galle, H. Ouyang, R. Shi, and E. Nauman, “Correlations between tissue-level stresses and strains and cellular damage within the guinea pig spinal cord white matter,” *J. Biomech.*, vol. 40, pp. 3029–3033, 2007, doi: 10.1016/j.jbiomech.2007.03.014.

[8] P. W. New and R. Marshall, “International Spinal Cord Injury Data Sets for non-traumatic spinal cord injury,” *Spinal Cord*, vol. 52, no. 2, pp. 123–132, Feb. 2014, doi: 10.1038/sc.2012.160.

[9] S. Kato and M. Fehlings, “Degenerative cervical myelopathy.,” *Curr. Rev. Musculoskelet. Med.*, vol. 9, no. 3, pp. 263–71, Sep. 2016, doi: 10.1007/s12178-016-9348-5.

[10] W. O. McKinley, R. T. Seel, and J. T. Hardman, “Nontraumatic spinal cord injury: incidence, epidemiology, and functional outcome,” *Arch. Phys. Med. Rehabil.*, vol. 80, no. 6, pp. 619–623, 1999, doi:

10.1016/S0003-9993(99)90162-4.

[11] P. W. New and V. Sundararajan, “Incidence of non-traumatic spinal cord injury in Victoria, Australia: a population-based study and literature review,” *Spinal Cord*, vol. 46, no. 6, pp. 406–411, Jun. 2008, doi: 10.1038/sj.sc.3102152.

[12] P. D. Purdy *et al.*, “Percutaneous translumbar spinal cord compression injury in dogs from an angioplasty balloon: MR and histopathologic changes with balloon sizes and compression times.,” *AJNR. Am. J. Neuroradiol.*, vol. 25, no. 8, pp. 1435–42, Sep. 2004, Accessed: Feb. 05, 2018. [Online]. Available: http://www.ncbi.nlm.nih.gov/pubmed/15466348.

[13] S. K. Karadimas, G. Gatzounis, and M. G. Fehlings, “Pathobiology of cervical spondylotic myelopathy,” *Eur. Spine J.*, vol. 24, no. S2, pp. 132–138, Apr. 2015, doi: 10.1007/s00586-014-3264-4.

[14] S. Asrar and M. Aarts, “TRPM7, the cytoskeleton and neuronal death.,” *Channels (Austin).*, vol. 7, no. 1, pp. 6–16, Jan. 2013, doi: 10.4161/chan.22824.

[15] B. M. Ellingson, D. C. Woodworth, K. Leu, N. Salamon, and L. T. Holly, “Spinal Cord Perfusion MR Imaging Implicates Both Ischemia and Hypoxia in the Pathogenesis of Cervical Spondylosis,” *World Neurosurg.*, vol. 128, pp. e773–e781, Aug. 2019, doi: 10.1016/J.WNEU.2019.04.253.

[16] D. G. Lyons, A. Parpaleix, M. Roche, and S. Charpak, “Mapping oxygen concentration in the awake mouse brain,” *Elife*, vol. 5, no. FEBRUARY2016, Feb. 2016, doi: 10.7554/ELIFE.12024.

[17] J. Mizuno, H. Nakagawa, K. Iwata, and Y. Hashizume, “Pathology of spinal cord lesions caused by ossification of the posterior longitudinal ligament, with special reference to reversibility of the spinal cord lesion,” *Neurol. Res.*, vol. 14, no. 4, pp. 312–314, 1992, doi: 10.1080/01616412.1992.11740075.

[18] B. M. Ellingson, D. C. Woodworth, K. Leu, N. Salamon, and L. T. Holly, “Spinal Cord Perfusion MR Imaging Implicates Both Ischemia and Hypoxia in the Pathogenesis of Cervical Spondylosis,” *World Neurosurg.*, May 2019, doi: 10.1016/j.wneu.2019.04.253.

[19] M. Alshareef *et al.*, “Effect of spinal cord compression on local vascular blood flow and perfusion capacity.,” *PLoS One*, vol. 9, no. 9, p. e108820, 2014, doi: 10.1371/journal.pone.0108820.

[20] J. L. Doppman, “The mechanism of ischemia in anteroposterior compression of the spinal cord,” *Invest. Radiol.*, vol. 10, no. 6, pp. 543–551, 1975, doi: 10.1097/00004424-197511000-00001.

[21] K. V. Timms, “Developing Experimental Models of Non-traumatic Spinal Cord Injury,” 2020.

[22] J. Fedorova, E. Kellerova, · Katarina Bimbova, and J. Pavel, “The

Histopathology of Severe Graded Compression in Lower Thoracic Spinal Cord Segment of Rat, Evaluated at Late Post-injury Phase," vol. 42, pp. 173–193, 2022, doi: 10.1007/s10571-021-01139-7.

[23] S. Lévy, G. Baucher, P.-H. Roche, M. Evin, V. Callot, and P.-J. Arnoux, "Biomechanical comparison of spinal cord compression types occurring in Degenerative Cervical Myelopathy," *Clin. Biomech.*, vol. 81, Jan. 2021, doi: 10.1016/J.CLINBIOMECH.2020.105174.

[24] M. Matsumoto *et al.*, "MRI of cervical intervertebral discs in asymptomatic subjects," *J. Bone Joint Surg. Br.*, vol. 80, no. 1, pp. 19–24, Jan. 1998, doi: 10.1302/0301-620X.80B1.7929.

[25] L. Müller-Jensen, C. J. Ploner, D. Kroneberg, and W. U. Schmidt, "Clinical Presentation and Causes of Non-traumatic Spinal Cord Injury: An Observational Study in Emergency Patients," *Front. Neurol.*, vol. 12, p. 1386, Aug. 2021, doi: 10.3389/FNEUR.2021.701927/BIBTEX.

[26] N. Nishida *et al.*, "Stress analysis of the cervical spinal cord: Impact of the morphology of spinal cord segments on stress," *J. Spinal Cord Med.*, vol. 39, no. 3, pp. 327–334, 2016, doi: 10.1179/2045772315Y.0000000012.

[27] B. N. de Sousa and L. A. Horrocks, "Development of Rat Spinal Cord," *Dev. Neurosci.*, vol. 2, no. 3, pp. 115–121, 1979, doi: 10.1159/000112445.

[28] J. Byrne and N. Dafny, "Neuroscience online: an electronic textbook for the neurosciences. Department of Neurobiology and Anatomy, The University of Texas Medical School at Houston," *Neuroscience*. 2017, Accessed: May 30, 2023. [Online]. Available: https://nba.uth.tmc.edu/neuroscience/m/s2/chapter03.html.

[29] Y. Sun *et al.*, "Establishment of a rat model of chronic thoracolumbar cord compression with a flat plastic screw," *Neural Regen. Res.*, vol. 11, no. 6, pp. 963–970, Jun. 2016, doi: 10.4103/1673-5374.184496.

[30] J. M. Gianino, J. A. Paice, and M. M. York, "Spinal Cord Anatomy," in *Intrathecal Drug Therapy for Spasticity and Pain*, New York, NY: Springer New York, 1996, pp. 3–14.

[31] C. S. Ahuja *et al.*, "Traumatic spinal cord injury," *Nat. Rev. Dis. Prim. 2017 31*, vol. 3, no. 1, pp. 1–21, Apr. 2017, doi: 10.1038/nrdp.2017.18.

[32] B. Rydevik, S. Holm, M. D. Brown, and G. Lundborg, "Diffusion from the cerebrospinal fluid as a nutritional pathway for spinal nerve roots," *Acta Physiol. Scand.*, vol. 138, no. 2, pp. 247–248, 1990, doi: 10.1111/J.1748-1716.1990.TB08843.X.

[33] K. Miyasaka, T. Asano, S. Ushikoshi, K. Hida, and I. Koyanagi, "Vascular anatomy of the spinal cord and classification of spinal arteriovenous malformations.," *Interv. Neuroradiol.*, vol. 6 Suppl 1, no. Suppl 1, pp. 195–8, Nov. 2000, doi: 10.1177/15910199000060S131.

[34] B. Kendall, "Vascular Anatomy of the Spinal Cord. Neurological

Investigations and Clinical Syndromes," *J. Neurol. Neurosurg. Psychiatry*, vol. 51, no. 10, pp. 1372–1372, 1988, doi: 10.1136/jnnp.51.10.1372-b.

[35] E. Hernandez-Gerez, I. N. Fleming, and S. H. Parson, "A role for spinal cord hypoxia in neurodegeneration," *Cell Death and Disease*, vol. 10, no. 11. Nature Publishing Group, pp. 1–8, Nov. 01, 2019, doi: 10.1038/s41419-019-2104-1.

[36] C. H. Tator and I. Koyanagi, "Vascular mechanisms in the pathophysiology of human spinal cord injury," *J. Neurosurg.*, vol. 86, no. 3, pp. 483–492, Mar. 1997, doi: 10.3171/jns.1997.86.3.0483.

[37] N. J. Smith *et al.*, "Spatiotemporal microvascular changes following contusive spinal cord injury," *Front. Neuroanat.*, vol. 17, p. 20, Mar. 2023, doi: 10.3389/FNANA.2023.1152131.

[38] Y. Li *et al.*, "Pericytes impair capillary blood flow and motor function after chronic spinal cord injury," *Nat. Med.*, vol. 23, no. 6, pp. 733–741, May 2017, doi: 10.1038/nm.4331.

[39] S. A. Figley, R. Khosravi, J. M. Legasto, Y.-F. Tseng, and M. G. Fehlings, "Characterization of vascular disruption and blood-spinal cord barrier permeability following traumatic spinal cord injury.," *J. Neurotrauma*, vol. 31, no. 6, pp. 541–52, Mar. 2014, doi: 10.1089/neu.2013.3034.

[40] S. Kobayashi and H. Yoshizawa, "Effect of mechanical compression on the vascular permeability of the dorsal root ganglion," *J. Orthop. Res.*, vol. 20, no. 4, pp. 730–739, Jul. 2002, doi: 10.1016/S0736-0266(01)00170-X.

[41] R. Kurokawa, H. Murata, M. Ogino, K. Ueki, and P. Kim, "Altered Blood Flow Distribution in the Rat Spinal Cord under Chronic Compression," *Spine (Phila. Pa. 1976).*, vol. 36, no. 13, pp. 1006–1009, Jun. 2011, doi: 10.1097/BRS.0b013e3181eaf33d.

[42] S. K. Karadimas *et al.*, "A novel experimental model of cervical spondylotic myelopathy (CSM) to facilitate translational research," *Neurobiol. Dis.*, vol. 54, pp. 43–58, Jun. 2013, doi: 10.1016/j.nbd.2013.02.013.

[43] H.-Q. Long, W.-H. Xie, W.-L. Chen, W.-L. Xie, J.-H. Xu, and Y. Hu, "Value of micro-CT for monitoring spinal microvascular changes after chronic spinal cord compression.," *Int. J. Mol. Sci.*, vol. 15, no. 7, pp. 12061–73, Jul. 2014, doi: 10.3390/ijms150712061.

[44] B. M. Ellingson, N. Salamon, D. C. Woodworth, and L. T. Holly, "Correlation between degree of subvoxel spinal cord compression measured with super-resolution tract density imaging and neurological impairment in cervical spondylotic myelopathy," *J. Neurosurg. Spine*, vol. 22, no. 6, pp. 631–638, Jun. 2015, doi: 10.3171/2014.10.SPINE14222.

[45] K. Kasahara, T. Nakagawa, and T. Kubota, “Neuronal Loss and Expression of Neurotrophic Factors in a Model of Rat Chronic Compressive Spinal Cord Injury,” *Spine (Phila. Pa. 1976).*, vol. 31, no. 18, pp. 2059–2066, Aug. 2006, doi: 10.1097/01.brs.0000231893.21964.f2.

[46] C. Bayer, K. Shi, S. T. Astner, C. A. Maftei, and P. Vaupel, “Acute versus chronic hypoxia: Why a simplified classification is simply not enough,” *International Journal of Radiation Oncology Biology Physics*, vol. 80, no. 4. Elsevier Inc., pp. 965–968, Jul. 15, 2011, doi: 10.1016/j.ijrobp.2011.02.049.

[47] N. L. Martirosyan, J. S. Feuerstein, N. Theodore, D. D. Cavalcanti, R. F. Spetzler, and M. C. Preul, “Blood supply and vascular reactivity of the spinal cord under normal and pathological conditions,” *J. Neurosurg. Spine*, vol. 15, no. 3, pp. 238–251, Sep. 2011, doi: 10.3171/2011.4.SPINE10543.

[48] K. Jellinger, “Circulation disorders of the spinal cord - Symposium organized by the österreichische Arbeitsgemeinschaft für Angiologie, March 4, 1972, Vienna (Austria),” *Acta Neurochir. (Wien).*, vol. 26, no. 4, pp. 327–337, 1972, doi: 10.1007/BF01407076.

[49] B. S. Bhutta, F. Alghoula, and I. Berim, “Hypoxia,” *StatPearls*, Aug. 2022, Accessed: May 12, 2023. [Online]. Available: https://www.ncbi.nlm.nih.gov/books/NBK482316/.

[50] Y. Sun *et al.*, “Establishment of a rat model of chronic thoracolumbar cord compression with a flat plastic screw.,” *Neural Regen. Res.*, vol. 11, no. 6, pp. 963–70, Jun. 2016, doi: 10.4103/1673-5374.184496.

[51] G. David *et al.*, “Traumatic and nontraumatic spinal cord injury: pathological insights from neuroimaging T1-weighted,” doi: 10.1038/s41582-019-0270-5.

[52] Y. Cao *et al.*, “Three-dimensional imaging of microvasculature in the rat spinal cord following injury,” *Nat. Publ. Gr.*, 2015, doi: 10.1038/srep12643.

[53] T. Bhatnagar *et al.*, “Relating Histopathology and Mechanical Strain in Experimental Contusion Spinal Cord Injury in a Rat Model.,” *J. Neurotrauma*, vol. 33, no. 18, pp. 1685–95, Sep. 2016, doi: 10.1089/neu.2015.4200.

[54] H.-Q. Long, W.-H. Xie, W.-L. Chen, W.-L. Xie, J.-H. Xu, and Y. Hu, “Value of Micro-CT for Monitoring Spinal Microvascular Changes after Chronic Spinal Cord Compression,” *Int. J. Mol. Sci.*, vol. 15, no. 7, pp. 12061–12073, Jul. 2014, doi: 10.3390/ijms150712061.

[55] D. Lu and G. S. Kassab, “Role of shear stress and stretch in vascular mechanobiology.,” *J. R. Soc. Interface*, vol. 8, no. 63, pp. 1379–85, Oct. 2011, doi: 10.1098/rsif.2011.0177.

[56] N. Resnick *et al.*, “Fluid shear stress and the vascular endothelium: for

better and for worse," *Prog. Biophys. Mol. Biol.*, vol. 81, no. 3, pp. 177–199, Apr. 2003, doi: 10.1016/S0079-6107(02)00052-4.

[57] Z. Ye *et al.*, "Effects of mechanical force on cytoskeleton structure and calpain-induced apoptosis in rat dorsal root ganglion neurons in vitro.," *PLoS One*, vol. 7, no. 12, p. e52183, 2012, doi: 10.1371/journal.pone.0052183.

[58] X. Cheng, H. Long, W. Chen, J. Xu, X. Wang, and F. Li, "The correlation between hypoxia-inducible factor-1α, matrix metalloproteinase-9 and functional recovery following chronic spinal cord compression," *Brain Res.*, vol. 1718, pp. 75–82, Sep. 2019, doi: 10.1016/J.BRAINRES.2019.04.034.

[59] Y. Li *et al.*, "Pericytes impair capillary blood flow and motor function after chronic spinal cord injury," *Nat. Med.*, vol. 23, no. 6, pp. 733–741, May 2017, doi: 10.1038/nm.4331.

[60] R. L. Benton and S. R. Whittemore, "VEGF165 Therapy Exacerbates Secondary Damage Following Spinal Cord Injury," *Neurochem. Res.*, vol. 28, no. 11, pp. 1693–1703, 2003, doi: 10.1023/A:1026013106016.

[61] H. Ikeda, Y. Ushio, T. Hayakawa, and H. Mogami, "Edema and circulatory disturbance in the spinal cord compressed by epidural neoplasms in rabbits," *J. Neurosurg.*, vol. 52, no. 2, pp. 203–209, Feb. 1980, doi: 10.3171/jns.1980.52.2.0203.

[62] H. Mestre *et al.*, "Flow of cerebrospinal fluid is driven by arterial pulsations and is reduced in hypertension," *Nat. Commun. 2018 91*, vol. 9, no. 1, pp. 1–9, Nov. 2018, doi: 10.1038/s41467-018-07318-3.

[63] L. M. Fahmy, Y. Chen, S. Xuan, E. M. Haacke, J. Hu, and Q. Jiang, "All Central Nervous System Neuro- and Vascular-Communication Channels Are Surrounded With Cerebrospinal Fluid," *Front. Neurol.*, vol. 12, p. 832, Jun. 2021, doi: 10.3389/FNEUR.2021.614636/BIBTEX.

[64] N. Nishida *et al.*, "Compression analysis of the gray and white matter of the spinal cord," *Neural Regen. Res.*, vol. 15, no. 7, p. 1344, Jul. 2020, doi: 10.4103/1673-5374.272604.

[65] H. Baba, Y. Maezawa, S. Imura, N. Kawahara, K. Nakahashi, and K. Tomita, "Quantitative analysis of the spinal cord motoneuron under chronic compression: an experimental observation in the mouse," *J. Neurol.*, vol. 243, no. 2, pp. 109–116, 1996, doi: 10.1007/BF02443999.

[66] C.-H. Chou, J. D. Sinden, P.-O. Couraud, M. Modo, and J. Schneider, "In Vitro Modeling of the Neurovascular Environment by Coculturing Adult Human Brain Endothelial Cells with Human Neural Stem Cells," *PLoS One*, vol. 9, no. 9, p. e106346, Sep. 2014, doi: 10.1371/journal.pone.0106346.

[67] L. Jiang *et al.*, "SRμCT Reveals 3D Microstructural Alterations of the Vascular and Neuronal Network in a Rat Model of Chronic Compressive Thoracic Spinal Cord Injury," vol. 11, no. 3, pp. 1–15,

2020.

[68] D. Martin *et al.*, “Experimental acute traumatic injury of the adult rat spinal cord by a subdural inflatable balloon: Methodology, behavioral analysis, and histopathology,” *J. Neurosci. Res.*, vol. 32, no. 4, pp. 539–550, Aug. 1992, doi: 10.1002/jnr.490320409.

[69] X. Cheng, H. Long, W. Chen, J. Xu, Y. Huang, and F. Li, “Three-dimensional alteration of cervical anterior spinal artery and anterior radicular artery in rat model of chronic spinal cord compression by micro-CT,” *Neurosci. Lett.*, vol. 606, pp. 106–112, Oct. 2015, doi: 10.1016/J.NEULET.2015.08.050.

[70] R. Kurokawa, H. Murata, M. Ogino, K. Ueki, and P. Kim, “Altered blood flow distribution in the rat spinal cord under chronic compression.,” *Spine (Phila. Pa. 1976).*, vol. 36, no. 13, pp. 1006–9, Jun. 2011, doi: 10.1097/BRS.0b013e3181eaf33d.

[71] H.-Q. Long *et al.*, “Is the speed of chronic compression an important factor for chronic spinal cord injury rat model?,” *Neurosci. Lett.*, vol. 545, pp. 75–80, 2013, doi: 10.1016/j.neulet.2013.04.024.

[72] T. Ohashi, T. Morimoto, K. Kawata, T. Yamada, and T. Sakaki, “Correlation Between Spinal Cord Blood Flow and Arterial Diameter Following Acute Spinal Cord Injury in Rats,” *Acta Neurochir*, vol. 138, pp. 322–329, 1996, Accessed: May 22, 2018. [Online]. Available: https://link.springer.com/content/pdf/10.1007%2FBF01411744.pdf.

[73] Z. Z. Khaing *et al.*, “Contrast-enhanced ultrasound to visualize hemodynamic changes after rodent spinal cord injury,” *J. Neurosurg. Spine*, vol. 29, no. 3, pp. 306–313, Sep. 2018, doi: 10.3171/2018.1.SPINE171202.

[74] J. M. Muradov, E. E. Ewan, and T. Hagg, “Dorsal column sensory axons degenerate due to impaired microvascular perfusion after spinal cord injury in rats,” *Exp. Neurol.*, vol. 249, pp. 59–73, 2013, doi: 10.1016/j.expneurol.2013.08.009.

[75] R. T. Dolan, J. S. Butler, J. M. O’Byrne, and A. R. Poynton, “Mechanical and cellular processes driving cervical myelopathy.,” *World J. Orthop.*, vol. 7, no. 1, pp. 20–9, Jan. 2016, doi: 10.5312/wjo.v7.i1.20.

[76] W.-H. Chung *et al.*, “Improved rat spinal cord injury model using spinal cord compression by percutaneous method.,” *J. Vet. Sci.*, vol. 14, no. 3, pp. 329–35, 2013, doi: 10.4142/JVS.2013.14.3.329.

[77] R. Ramsey and J. L. Doppman, “The Effects of Epidural Masses on Spinal Cord Blood Flow,” *https://doi.org/10.1148/107.1.99*, vol. 107, no. 1, pp. 99–103, Apr. 1973, doi: 10.1148/107.1.99.

[78] M. Sharif-Alhoseini *et al.*, “Animal models of spinal cord injury: a systematic review,” *Spinal Cord 2017 558*, vol. 55, no. 8, pp. 714–721, Jan. 2017, doi: 10.1038/sc.2016.187.

[79] Y. Cao *et al.*, “Three-dimensional imaging of microvasculature in the rat spinal cord following injury.,” *Sci. Rep.*, vol. 5, p. 12643, Jul. 2015, doi: 10.1038/srep12643.

[80] J. Xu *et al.*, “Ultrastructural Features of Neurovascular Units in a Rat Model of Chronic Compressive Spinal Cord Injury,” *Front. Neuroanat.*, vol. 11, p. 136, Jan. 2018, doi: 10.3389/fnana.2017.00136.

[81] Y. Shimomura, S. Hukuda, and S. Mizuno, “Experimental Study of Ischemic Damage to the Cervical Spinal Cord,” *J. Neurosurg.*, vol. 28, no. 6, pp. 565–581, Jun. 1968, doi: 10.3171/jns.1968.28.6.0565.

[82] Y. Cao *et al.*, “Three-dimensional imaging of microvasculature in the rat spinal cord following injury.,” *Sci. Rep.*, vol. 5, p. 12643, Jul. 2015, doi: 10.1038/srep12643.

[83] Z. Yu *et al.*, “Spinal Cord Parenchyma Vascular Redistribution Underlies Hemodynamic and Neurophysiological Changes at Dynamic Neck Positions in Cervical Spondylotic Myelopathy,” *Front. Neuroanat.*, vol. 15, p. 92, Nov. 2021, doi: 10.3389/FNANA.2021.729482/BIBTEX.

[84] H. Y, O. T, M. T, H. M, and Y. H, “Real-time direct measurement of spinal cord blood flow at the site of compression: relationship between blood flow recovery and motor deficiency in spinal cord injury,” *Spine (Phila. Pa. 1976).*, vol. 32, no. 18, pp. 1955–1962, Aug. 2007, doi: 10.1097/BRS.0B013E3181316310.

[85] S. Okimatsu *et al.*, “Early decompression promotes motor recovery after cervical spinal cord injury in rats with chronic cervical spinal cord compression,” *Sci. Reports 2022 121*, vol. 12, no. 1, pp. 1–8, Aug. 2022, doi: 10.1038/s41598-022-14723-8.

[86] “Detailed Explanation of the Finite Element Method (FEM).” https://www.comsol.com/multiphysics/finite-element-method (accessed May 29, 2023).

[87] Y.-B. Yan, W. Qi, Z.-X. Wu, T.-X. Qiu, E.-C. Teo, and W. Lei, “Finite Element Study of the Mechanical Response in Spinal Cord during the Thoracolumbar Burst Fracture,” *PLoS One*, vol. 7, no. 9, p. e41397, Sep. 2012, doi: 10.1371/journal.pone.0041397.

[88] R. K. Wilcox, D. J. Allen, R. M. Hall, D. Limb, D. C. Barton, and R. A. Dickson, “A dynamic investigation of the burst fracture process using a combined experimental and finite element approach,” *Eur. Spine J.*, vol. 13, no. 6, pp. 481–488, Oct. 2004, doi: 10.1007/s00586-003-0625-9.

[89] R. J. Oakland, “A biomechanical study of the spinal cord in the burst fracture process.,” 2003.

[90] K. Ichihara, T. Taguchi, I. Sakuramoto, S. Kawano, and S. Kawai, “Mechanism of the spinal cord injury and the cervical spondylotic myelopathy: new approach based on the mechanical features of the spinal cord white and gray matter,” *J. Neurosurg. Spine*, vol. 99, no. 3,

pp. 278–285, Oct. 2003, doi: 10.3171/spi.2003.99.3.0278.

[91] C. J. Sparrey, G. T. Manley, and T. M. Keaveny, “Effects of White, Grey, and Pia Mater Properties on Tissue Level Stresses and Strains in the Compressed Spinal Cord,” *J. Neurotrauma*, vol. 26, no. 4, pp. 585–595, Apr. 2009, doi: 10.1089/neu.2008.0654.

[92] C. M. Russell, A. M. Choo, W. Tetzlaff, T.-E. Chung, and T. R. Oxland, “Maximum Principal Strain Correlates with Spinal Cord Tissue Damage in Contusion and Dislocation Injuries in the Rat Cervical Spine,” *J. Neurotrauma*, vol. 29, no. 8, pp. 1574–1585, May 2012, doi: 10.1089/neu.2011.2225.

[93] V. N. Wijayathunga, A. C. Jones, R. J. Oakland, N. R. Furtado, R. M. Hall, and R. K. Wilcox, “Development of specimen-specific finite element models of human vertebrae for the analysis of vertebroplasty,” *Proc. Inst. Mech. Eng. Part H J. Eng. Med.*, vol. 222, no. 2, pp. 221–228, Feb. 2008, doi: 10.1243/09544119JEIM285.

[94] A. Rohlmann, T. Zander, and G. Bergmann, “Effect of Total Disc Replacement with ProDisc on Intersegmental Rotation of the Lumbar Spine,” *Spine (Phila. Pa. 1976).*, vol. 30, no. 7, pp. 738–743, Accessed: Apr. 23, 2018. [Online]. Available: https://insights.ovid.com/pubmed?pmid=15803074.

[95] C. Persson, J. Summers, and R. M. Hall, “The Importance of Fluid-Structure Interaction in Spinal Trauma Models,” *J. Neurotrauma*, vol. 28, no. 1, pp. 113–125, Jan. 2011, doi: 10.1089/neu.2010.1332.

[96] C. D. Bertram and M. Heil, “A Poroelastic Fluid/Structure-Interaction Model of Cerebrospinal Fluid Dynamics in the Cord With Syringomyelia and Adjacent Subarachnoid-Space Stenosis,” *J. Biomech. Eng.*, vol. 139, no. 1, p. 011001, Nov. 2016, doi: 10.1115/1.4034657.

[97] I. N. Drøsdal, “Porous and Viscous Modeling of Cerebrospinal Fluid Flow in the Spinal Canal Associated with Syringomyelia Det matematisk-naturvitenskapelige fakultet Universitetet i Oslo,” 2011. Accessed: Jul. 31, 2019. [Online]. Available: https://www.duo.uio.no/bitstream/handle/10852/10872/DROSDALthesis.pdf?sequence=3&isAllowed=y.

[98] J. Hu *et al.*, “Nondestructive imaging of the internal microstructure of vessels and nerve fibers in rat spinal cord using phase-contrast synchrotron radiation microtomography,” *J. Synchrotron Radiat.*, vol. 24, no. 2, pp. 482–489, Mar. 2017, doi: 10.1107/S1600577517000121.

[99] P. Xu *et al.*, “Destructive pathological changes in the rat spinal cord due to chronic mechanical compression,” *J. Neurosurg. Spine*, vol. 8, no. 3, pp. 279–285, Mar. 2008, doi: 10.3171/SPI/2008/8/3/279.

[100] E. Bianchetti, M. Mladinic, and A. Nistri, “Mechanisms underlying cell death in ischemia-like damage to the rat spinal cord in vitro.,” *Cell Death Dis.*, vol. 4, no. 7, p. e707, Jul. 2013, doi: 10.1038/cddis.2013.237.

[101] A. Kuzhandaivel, A. Nistri, G. L. Mazzone, and M. Mladinic, “Molecular Mechanisms Underlying Cell Death in Spinal Networks in Relation to Locomotor Activity After Acute Injury in vitro.,” *Front. Cell. Neurosci.*, vol. 5, p. 9, 2011, doi: 10.3389/fncel.2011.00009.

[102] J. Claron *et al.*, “Large-scale functional ultrasound imaging of the spinal cord reveals in-depth spatiotemporal responses of spinal nociceptive circuits in both normal and inflammatory states,” *Pain*, vol. 162, no. 4, pp. 1047–1059, Apr. 2021, doi: 10.1097/j.pain.0000000000002078.

[103] K. B. Ghaghada, K. H. J. Bockhorst, S. Mukundan, A. V. Annapragada, and P. A. Narayana, “High-Resolution Vascular Imaging of the Rat Spine Using Liposomal Blood Pool MR Agent,” *AJNR Am. J. Neuroradiol.*, vol. 28, no. 1, p. 48, Jan. 2007, Accessed: Nov. 30, 2021. [Online]. Available: /pmc/articles/PMC1773015/.

[104] J. Xu *et al.*, “Ultrastructural Features of Neurovascular Units in a Rat Model of Chronic Compressive Spinal Cord Injury,” *Front. Neuroanat.*, vol. 11, p. 136, Jan. 2018, doi: 10.3389/fnana.2017.00136.

[105] J. T. Maikos, Z. Qian, D. Metaxas, and D. I. Shreiber, “Finite Element Analysis of Spinal Cord Injury in the Rat,” *J. Neurotrauma*, vol. 25, pp. 795–816, 2008, doi: 10.1089/neu.2007.0423.

[106] T. M. Jackman, A. M. DelMonaco, and E. F. Morgan, “Accuracy of finite element analyses of CT scans in predictions of vertebral failure patterns under axial compression and anterior flexion,” *J. Biomech.*, vol. 49, no. 2, pp. 267–275, Jan. 2016, doi: 10.1016/j.jbiomech.2015.12.004.

[107] J. T. Maikos, R. A. I. Elias, and D. I. Shreiber, “Mechanical Properties of Dura Mater from the Rat Brain and Spinal Cord,” *J. Neurotrauma*, vol. 25, no. 1, pp. 38–51, Jan. 2008, doi: 10.1089/neu.2007.0348.

[108] R. J. Fiford and L. E. Bilston, “The mechanical properties of rat spinal cord in vitro,” *J. Biomech.*, vol. 38, pp. 1509–1515, 2005, doi: 10.1016/j.jbiomech.2004.07.009.

[109] K. Ichihara, T. Taguchi, Y. Shimada, I. Sakuramoto, S. Kawano, and S. Kawai, “Gray Matter of the Bovine Cervical Spinal Cord is Mechanically More Rigid and Fragile than the White Matter,” *J. Neurotrauma*, vol. 18, no. 3, pp. 361–367, Mar. 2001, doi: 10.1089/08977150151071053.

[110] B. D. Snyder *et al.*, “Noninvasive Prediction of Fracture Risk in Patients with Metastatic Cancer to the Spine.,” *Clin. Cancer Res.*, vol. 15, no. 24, pp. 7676–7683, Dec. 2009, doi: 10.1158/1078-0432.CCR-09-0420.

[111] C. Y. Greaves, M. S. Gadala, and T. R. Oxland, “A Three-Dimensional Finite Element Model of the Cervical Spine with Spinal Cord: An Investigation of Three Injury Mechanisms,” *Ann. Biomed. Eng.*, vol. 36, no. 3, pp. 396–405, Mar. 2008, doi: 10.1007/s10439-008-9440-0.

[112] S. Cheng, E. C. Clarke, and L. E. Bilston, “The effects of

preconditioning strain on measured tissue properties," *J. Biomech.*, vol. 42, pp. 1360–1362, doi: 10.1016/j.jbiomech.2009.03.023.

[113] "Simulating Cerebrospinal Fluid Flow and Spinal Cord Movement Associated with Syringomyelia Fluid Structure Interaction in Idealized Geometries," Accessed: Jan. 12, 2018. [Online]. Available: https://www.duo.uio.no/bitstream/handle/10852/51949/Vegard_Vinje_Thesis.pdf?sequence=1.

[114] N. L. Ramo *et al.*, "Comparison of in vivo and ex vivo viscoelastic behavior of the spinal cord," *Acta Biomater.*, vol. 68, pp. 78–89, Mar. 2018, doi: 10.1016/J.ACTBIO.2017.12.024.

[115] R. Shi and J. Whitebone, "Conduction Deficits and Membrane Disruption of Spinal Cord Axons as a Function of Magnitude and Rate of Strain," *J. Neurophysiol.*, vol. 95, no. 6, pp. 3384–3390, Jun. 2006, doi: 10.1152/jn.00350.2005.

[116] N. Nishida, T. Kanchiku, Y. Kato, Y. Imajo, S. Kawano, and T. Taguchi, "Biomechanical analysis of the spinal cord in brown-séquard syndrome," *Exp. Ther. Med.*, vol. 6, no. 5, pp. 1184–1188, Nov. 2013, doi: 10.3892/etm.2013.1286.

[117] C. J. Sparrey and T. M. Keaveny, "Compression behavior of porcine spinal cord white matter," *J. Biomech.*, vol. 44, no. 6, pp. 1078–1082, Apr. 2011, doi: 10.1016/j.jbiomech.2011.01.035.

[118] I. Vitro, L. E. Bilston, and L. E. Thibaultt, "The Mechanical Properties of the Human Cervical Spinal Cord," *Ann. Biomed. Eng.*, vol. 24, pp. 67–74, 1996, Accessed: Jan. 31, 2018. [Online]. Available: https://link.springer.com/content/pdf/10.1007%2FBF02770996.pdf.

[119] B. Hunter, "Spinal Cord Modelling for Understanding and," 2016.

[120] D. F. Meaney, "Relationship between structural modeling and hyperelastic material behavior: application to CNS white matter," *Biomech. Model. Mechanobiol.*, vol. 1, no. 4, pp. 279–293, Apr. 2003, doi: 10.1007/s10237-002-0020-1.

[121] L. R. Sharkey, "An inverse finite element approach to modeling the rat cervical spinal cord : for use in determining the mechanical properties of the grey and white matter," 2018, doi: 10.14288/1.0363918.

[122] J. T. Maikos and D. I. Shreiber, "Immediate Damage to The Blood-Spinal Cord Barrier Due to Mechanical Trauma," *J. Neurotrauma*, vol. 24, no. 3, pp. 492–507, Mar. 2007, doi: 10.1089/neu.2006.0149.

[123] J. Maikos, R. Elias, Z. Qian, D. Metaxas, and D. Shreiber, "In Vivo Tissue-Level Thresholds for Spinal Cord Injury," in *ASME 2007 Summer Bioengineering Conference*, Jun. 2007, p. 421, doi: 10.1115/SBC2007-176670.

[124] A. Karimi, A. Shojaei, and P. Tehrani, "Mechanical properties of the human spinal cord under the compressive loading," *J. Chem. Neuroanat.*, vol. 86, pp. 15–18, Dec. 2017, doi:

10.1016/J.JCHEMNEU.2017.07.004.

[125] R. W. Ogden, “Large Deformation Isotropic Elasticity - On the Correlation of Theory and Experiment for Incompressible Rubberlike Solids,” *Proc. R. Soc. A Math. Phys. Eng. Sci.*, vol. 326, no. 1567, pp. 565–584, Feb. 1972, doi: 10.1098/rspa.1972.0026.

[126] A. Rycman, S. McLachlin, and D. S. Cronin, “A Hyper-Viscoelastic Continuum-Level Finite Element Model of the Spinal Cord Assessed for Transverse Indentation and Impact Loading,” *Front. Bioeng. Biotechnol.*, vol. 9, p. 684, Aug. 2021, doi: 10.3389/FBIOE.2021.693120/BIBTEX.

[127] C. S. Park and S. J. Payne, “Modelling the effects of cerebral microvasculature morphology on oxygen transport,” *Med. Eng. Phys.*, vol. 38, no. 1, pp. 41–47, Jan. 2016, doi: 10.1016/J.MEDENGPHY.2015.09.004.

[128] M. Q. Zhang *et al.*, “Three-dimensional visualization of rat brain microvasculature following permanent focal ischaemia by synchrotron radiation.,” *Br. J. Radiol.*, vol. 87, no. 1038, p. 20130670, Jun. 2014, doi: 10.1259/bjr.20130670.

[129] P. W. Sweeney, S. Walker-Samuel, and R. J. Shipley, “Insights into cerebral haemodynamics and oxygenation utilising in vivo mural cell imaging and mathematical modelling.,” *Sci. Rep.*, vol. 8, no. 1, p. 1373, Jan. 2018, doi: 10.1038/s41598-017-19086-z.

[130] P. D. Morris *et al.*, “Computational fluid dynamics modelling in cardiovascular medicine,” doi: 10.1136/heartjnl-2015-308044.

[131] G. A. Holzapfel, “Determination of material models for arterial walls from uniaxial extension tests and histological structure,” *J. Theor. Biol.*, vol. 238, no. 2, pp. 290–302, Jan. 2006, doi: 10.1016/J.JTBI.2005.05.006.

[132] C. A. Taylor and J. D. Humphrey, “Open Problems in Computational Vascular Biomechanics: Hemodynamics and Arterial Wall Mechanics.,” *Comput. Methods Appl. Mech. Eng.*, vol. 198, no. 45–46, pp. 3514–3523, Sep. 2009, doi: 10.1016/j.cma.2009.02.004.

[133] J. Y. Moon, D. C. Suh, Y. S. Lee, Y. W. Kim, and J. S. Lee, “Considerations of blood properties, outlet boundary conditions and energy loss approaches in computational fluid dynamics modeling.,” *Neurointervention*, vol. 9, no. 1, pp. 1–8, Feb. 2014, doi: 10.5469/neuroint.2014.9.1.1.

[134] R. J. Shipley, A. F. Smith, P. Sweeney, P. W. Sweeney, A. R. Pries, and T. W. Secomb, “A hybrid discrete-continuum approach for modelling microcirculatory blood flow Realistic numerical image-based modelling of biological tissue substrates View project Transcriptional and Posttranscriptional Regulation View project A hybrid discrete-continuum approach for modelling microcirculatory blood flow,” *Math. Med. Biol. A J. IMA*, vol. 00, pp. 1–18, 2019, doi:

10.1093/imammb/dqz006.

[135] E. Hodneland *et al.*, “A new framework for assessing subject-specific whole brain circulation and perfusion using mri-based measurements and a multiscale continuous flow model,” *PLoS Comput. Biol.*, vol. 15, no. 6, Jun. 2019, doi: 10.1371/journal.pcbi.1007073.

[136] T. I. Józsa, R. M. Padmos, N. Samuels, W. K. El-Bouri, A. G. Hoekstra, and S. J. Payne, “ A porous circulation model of the human brain for in silico clinical trials in ischaemic stroke ,” *Interface Focus*, vol. 11, no. 1, p. 20190127, Feb. 2021, doi: 10.1098/rsfs.2019.0127.

[137] R. Penta and J. Merodio, “Homogenized modeling for vascularized poroelastic materials,” *Meccanica*, vol. 52, no. 14, pp. 3321–3343, 2017, doi: 10.1007/s11012-017-0625-1.

[138] M. Sharan, B. Singh, M. P. Singh, and P. W. Kumar, “Finite-Element Analysis of Oxygen Transport in the Systemic Capillaries,” *IMA J. Math. Appl. Med. Biol.*, vol. 8, pp. 107–123, 1991, Accessed: May 29, 2023. [Online]. Available: https://academic.oup.com/imammb/article/8/2/107/698748.

[139] A. E. Kovtanyuk, A. Y. Chebotarev, N. D. Botkin, V. L. Turova, I. N. Sidorenko, and R. Lampe, “Nonstationary Model of Oxygen Transport in Brain Tissue,” *Comput. Math. Methods Med.*, vol. 2020, 2020, doi: 10.1155/2020/4861654.

[140] T. W. Secomb, R. Hsu, E. Y. H. Park, and M. W. Dewhirst, “Green’s Function Methods for Analysis of Oxygen Delivery to Tissue by Microvascular Networks,” *Ann. Biomed. Eng.*, vol. 32, no. 11, pp. 1519–1529, doi: 10.1114/b:abme.0000049036.08817.44.

[141] C. S. Park and S. J. Payne, “Modelling the effects of cerebral microvasculature morphology on oxygen transport,” *Med. Eng. Phys.*, vol. 38, no. 1, pp. 41–47, Jan. 2016, doi: 10.1016/J.MEDENGPHY.2015.09.004.

[142] A. E. Kovtanyuk, A. Y. Chebotarev, A. A. Dekalchuk, N. D. Botkin, and R. Lampe, “Analysis of a mathematical model of oxygen transport in brain,” pp. 187–191.

[143] A. Devor, L. Ruvinskaya, A. M. Dale, Q. Fang, S. Sakadžić, and D. A. Boas, “Oxygen advection and diffusion in a three-dimensional vascular anatomical network,” *Opt. Express, Vol. 16, Issue 22, pp. 17530-17541*, vol. 16, no. 22, pp. 17530–17541, Oct. 2008, doi: 10.1364/OE.16.017530.

[144] H. J. Kim, K. E. Jansen, and C. A. Taylor, “Incorporating Autoregulatory Mechanisms of the Cardiovascular System in Three-Dimensional Finite Element Models of Arterial Blood Flow,” doi: 10.1007/s10439-010-9992-7.

[145] S. K. Karadimas *et al.*, “A novel experimental model of cervical spondylotic myelopathy (CSM) to facilitate translational research,”

Neurobiol. Dis., vol. 54, pp. 43–58, Jun. 2013, doi: 10.1016/J.NBD.2013.02.013.

[146] K. Ichihara, T. Taguchi, I. Sakuramoto, S. Kawano, and S. Kawai, “Mechanism of the spinal cord injury and the cervical spondylotic myelopathy: new approach based on the mechanical features of the spinal cord white and gray matter,” *J. Neurosurg. Spine*, vol. 99, no. 3, pp. 278–285, Oct. 2003, doi: 10.3171/spi.2003.99.3.0278.

[147] L. E. Bilston, “Finite Element Analysis of Some Cervical Spinal Cord Injury Modes,” 1998.

[148] R. J. Oakland, R. M. Hall, R. K. Wilcox, and D. C. Barton, “The biomechanical response of spinal cord tissue to uniaxial loading,” doi: 10.1243/09544119JEIM135.

[149] L. R. Sass, M. Khani, G. C. Natividad, R. S. Tubbs, O. Baledent, and B. A. Martin, “A 3D subject-specific model of the spinal subarachnoid space with anatomically realistic ventral and dorsal spinal cord nerve rootlets,” *Fluids Barriers CNS*, vol. 14, no. 1, p. 36, Dec. 2017, doi: 10.1186/s12987-017-0085-y.

[150] A. Helgeland, K. A. Mardal, V. Haughton, and B. A. P. Reif, “Numerical simulations of the pulsating flow of cerebrospinal fluid flow in the cervical spinal canal of a Chiari patient,” *J. Biomech.*, vol. 47, no. 5, pp. 1082–1090, Mar. 2014, doi: 10.1016/j.jbiomech.2013.12.023.

[151] J. H. Thomas, “Fluid dynamics of cerebrospinal fluid flow in perivascular spaces,” *J. R. Soc. Interface*, vol. 16, no. 159, p. 20190572, Oct. 2019, doi: 10.1098/rsif.2019.0572.

[152] L. E. Bilston, D. F. Fletcher, A. R. Brodbelt, and M. A. Stoodley, “Arterial Pulsation-driven Cerebrospinal Fluid Flow in the Perivascular Space: A Computational Model,” doi: 10.1080/10255840310001606116.

[153] J. Venton, “A Poroelastic Model of Spinal Cord Cavities The Mechanical Role of Oedema in Syringomyelia,” 2018. Accessed: Jul. 04, 2019. [Online]. Available: https://research.brighton.ac.uk/en/studentTheses/a-poroelastic-model-of-spinal-cord-cavities.

[154] K. Støverud, “Modeling Convection-Enhanced Delivery into Brain Tissue using Information from Magnetic Resonance Imaging.,” Dec. 2009, Accessed: Jul. 31, 2019. [Online]. Available: https://dspace.library.uu.nl/handle/1874/37013.

[155] L. Ray, J. J. Iliff, and J. J. Heys, “Analysis of convective and diffusive transport in the brain interstitium,” *Fluids Barriers CNS*, vol. 16, no. 1, p. 6, Dec. 2019, doi: 10.1186/s12987-019-0126-9.

[156] T. W. Secomb, R. Hsu, N. B. Beamer, and B. M. Coull, “Theoretical simulation of oxygen transport to brain by networks of microvessels: effects of oxygen supply and demand on tissue hypoxia.,”

Microcirculation, vol. 7, no. 4, pp. 237–47, Aug. 2000, Accessed: Nov. 26, 2018. [Online]. Available: http://www.ncbi.nlm.nih.gov/pubmed/10963629.

[157] B. C. Fry, J. Lee, N. P. Smith, and T. W. Secomb, “Estimation of blood flow rates in large microvascular networks.,” *Microcirculation*, vol. 19, no. 6, pp. 530–8, Aug. 2012, doi: 10.1111/j.1549-8719.2012.00184.x.

[158] Y. Sun *et al.*, “Establishment of a rat model of chronic thoracolumbar cord compression with a flat plastic screw.,” *Neural Regen. Res.*, vol. 11, no. 6, pp. 963–70, Jun. 2016, doi: 10.4103/1673-5374.184496.

[159] S. Henmar, E. B. Simonsen, and R. W. Berg, “What are the gray and white matter volumes of the human spinal cord?,” *J. Neurophysiol.*, vol. 124, no. 6, pp. 1792–1797, Dec. 2020, doi: 10.1152/JN.00413.2020/ASSET/IMAGES/LARGE/AJ-NEUR200057F003.JPEG.

[160] A. Da Circulação Medular, A. Campos, M. Amato, N. Antônio, and G. Stolf, “Anatomy of spinal blood supply,” *July-Sept. J Vasc Bras July-Sept*, vol. 14, no. 143, 2015, doi: 10.1590/1677-5449.0004.

[161] M. F. Shamji, D. E. Maziak, F. M. Shamji, R. J. Ginsberg, and R. Pon, “Circulation of the spinal cord: An important consideration for thoracic surgeons,” *Annals of Thoracic Surgery*, vol. 76, no. 1. Elsevier, pp. 315–321, Jul. 01, 2003, doi: 10.1016/S0003-4975(03)00139-5.

[162] S. Zhu, Y. Wang, P. Yin, and Q. Su, “A systematic review of surgical procedures on thoracic myelopathy,” *J. Orthop. Surg. Res.*, vol. 15, no. 1, pp. 1–10, Dec. 2020, doi: 10.1186/S13018-020-02081-Y/TABLES/4.

[163] A. N. Bosmia, E. Hogan, M. Loukas, R. S. Tubbs, and A. A. Cohen-Gadol, “Blood supply to the human spinal cord: Part I. Anatomy and hemodynamics,” *Clin. Anat.*, vol. 28, no. 1, pp. 52–64, Jan. 2015, doi: 10.1002/ca.22281.

[164] G. J. Romane, “The Arterial Blood Supply of the Human Spinal Cord,” 1964. doi: 10.1038/sc.1965.37.

[165] T. Tokioka, “The arterial system of the spinal cord in the rat.,” *Okajimas Folia Anat. Jpn.*, vol. 50, no. 2, pp. 133–82, Aug. 1973, Accessed: Jul. 04, 2019. [Online]. Available: http://www.ncbi.nlm.nih.gov/pubmed/4800588.

[166] M. J. Farrar, J. D. Rubin, D. M. Diago, and C. B. Schaffer, “Characterization of blood flow in the mouse dorsal spinal venous system before and after dorsal spinal vein occlusion,” *J. Cereb. Blood Flow Metab.*, vol. 35, no. 4, pp. 667–675, Mar. 2015, doi: 10.1038/jcbfm.2014.244.

[167] H. Ozawa, T. Matsumoto, T. Ohashi, M. Sato, and S. Kokubun, “Mechanical properties and function of the spinal pia mater,” *J. Neurosurg. Spine*, vol. 1, no. 1, pp. 122–127, Jul. 2004, doi: 10.3171/spi.2004.1.1.0122.

[168] J. Yu, N. Manouchehri, S. Yamamoto, B. K. Kwon, and T. R. Oxland, “Mechanical properties of spinal cord grey matter and white matter in confined compression,” *J. Mech. Behav. Biomed. Mater.*, p. 104044, Aug. 2020, doi: 10.1016/j.jmbbm.2020.104044.

[169] K. H. Støverud, M. Alnæs, H. P. Langtangen, V. Haughton, and K. A. Mardal, “Poro-elastic modeling of Syringomyelia – a systematic study of the effects of pia mater, central canal, median fissure, white and gray matter on pressure wave propagation and fluid movement within the cervical spinal cord,” *http://dx.doi.org/10.1080/10255842.2015.1058927*, vol. 19, no. 6, pp. 686–698, Apr. 2015, doi: 10.1080/10255842.2015.1058927.

[170] T. W. Barber, J. A. Brockway, and L. S. Higgins, “The Density of Tissues in and about the Head,” *Acta Neurol. Scand.*, vol. 46, no. 1, pp. 85–92, Mar. 1970, doi: 10.1111/j.1600-0404.1970.tb05606.x.

[171] M. Heil and C. D. Bertram, “A poroelastic fluid–structure interaction model of syringomyelia,” *J. Fluid Mech.*, vol. 809, pp. 360–389, Dec. 2016, doi: 10.1017/jfm.2016.669.

[172] P. W. Sweeney, S. Walker-Samuel, and R. J. Shipley, “Insights into cerebral haemodynamics and oxygenation utilising in 1 vivo mural cell imaging and mathematical modelling-2 Supplementary Material.” Accessed: Dec. 18, 2018. [Online]. Available: https://static-content.springer.com/esm/art%3A10.1038%2Fs41598-017-19086-z/MediaObjects/41598_2017_19086_MOESM1_ESM.pdf.

[173] M. Heil and C. D. Bertram, “A poroelastic fluid–structure interaction model of syringomyelia,” *J. Fluid Mech.*, vol. 809, pp. 360–389, Dec. 2016, doi: 10.1017/jfm.2016.669.

[174] T. I. Józsa, R. M. Padmos, W. K. El-Bouri, A. G. Hoekstra, and S. J. Payne, “On the Sensitivity Analysis of Porous Finite Element Models for Cerebral Perfusion Estimation,” *Ann. Biomed. Eng.*, vol. 49, no. 12, pp. 3647–3665, 2021, doi: 10.1007/s10439-021-02808-w.

[175] A. N. Cookson *et al.*, “A novel porous mechanical framework for modelling the interaction between coronary perfusion and myocardial mechanics.,” *J. Biomech.*, vol. 45, no. 5, pp. 850–5, Mar. 2012, doi: 10.1016/j.jbiomech.2011.11.026.

[176] Sun and Qiang, “Numerical Simulation of Blood Flow through Permeable Vascular Network Embedded in Tumour Porous Interstitium,” 2011, Accessed: May 22, 2018. [Online]. Available: http://discovery.ucl.ac.uk/1306876/1/1306876.pdf.

[177] C. Debbaut, J. Vierendeels, J. H. Siggers, R. Repetto, D. Monbaliu, and P. Segers, “A 3D porous media liver lobule model: the importance of vascular septa and anisotropic permeability for homogeneous perfusion,” *Comput. Methods Biomech. Biomed. Engin.*, vol. 17, no. 12, pp. 1295–1310, Sep. 2014, doi: 10.1080/10255842.2012.744399.

[178] N. Westerhof, N. Stergiopulos, and M. I. M. Noble, “Viscosity,”

Snapshots of Hemodynamics, pp. 3–8, 2010, doi: 10.1007/978-1-4419-6363-5_1.

[179] The Engineering Toolbox, “Gas Density , Molecular Weight and Density Gas Density , Molecular Weight and Density,” pp. 14–15, 2017, Accessed: Sep. 14, 2020. [Online]. Available: http://www.teknopoli.com/PDF/Gas_Density_Table.pdf.

[180] J. Venton, S. Bouyagoub, P. J. Harris, and G. Phillips, “Deriving Spinal Cord Permeability and Porosity Using Diffusion-Weighted MRI Data,” 2017. doi: 10.1061/9780784480779.180.

[181] E. Syková, J. Svoboda, J. Polák, and A. Chvátal, “Extracellular volume fraction and diffusion characteristics during progressive ischemia and terminal anoxia in the spinal cord of the rat,” *J. Cereb. Blood Flow Metab.*, vol. 14, no. 2, pp. 301–311, Jun. 1994, doi: 10.1038/jcbfm.1994.37.

[182] T. I. Józsa, W. K. El-Bouri, R. M. Padmos, S. J. Payne, and A. G. Hoekstra, “A cerebral circulation model for in silico clinical trials of ischaemic stroke,” *CompBioMed Conf. 2019*, no. iii, pp. 4–7, 2019, Accessed: Mar. 16, 2021. [Online]. Available: www.insist-h2020.eu.

[183] C. Hadjistassou, A. Bejan, and Y. Ventikos, “Cerebral oxygenation and optimal vascular brain organization,” doi: 10.1098/rsif.2015.0245.

[184] Z. Z. Khaing *et al.*, “Contrast-enhanced ultrasound to visualize hemodynamic changes after rodent spinal cord injury,” *J. Neurosurg. Spine*, vol. 29, no. 3, pp. 306–313, Sep. 2018, doi: 10.3171/2018.1.SPINE171202.

[185] A. S. Rivlin and C. H. Tator, “Regional spinal cord blood flow in rats after severe cord trauma,” *J. Neurosurg.*, vol. 49, no. 6, pp. 844–853, Dec. 1978, doi: 10.3171/jns.1978.49.6.0844.

[186] N. Hayashi, B. A. Green, J. Mora, M. González-Carvajal, and R. P. Veraa, “Simultaneous measurement of local blood flow and tissue oxygen in rat spinal cord,” *Neurol. Res.*, vol. 5, no. 4, pp. 49–58, 1983, doi: 10.1080/01616412.1983.11758588.

[187] A. Pichiecchio *et al.*, “Normalization of Spinal Cord Total Cross-Sectional and Gray Matter Areas as Quantified With Radially Sampled Averaged Magnetization Inversion Recovery Acquisitions,” *Front. Neurol.* | *www.frontiersin.org*, vol. 1, p. 637198, 2021, doi: 10.3389/fneur.2021.637198.

[188] E. L. Rolett, A. Azzawi, K. J. Liu, M. N. Yongbi, H. M. Swartz, and J. F. Dunn, “Critical oxygen tension in rat brain: a combined (31)P-NMR and EPR oximetry study,” *Am. J. Physiol. Regul. Integr. Comp. Physiol.*, vol. 279, no. 1, 2000, doi: 10.1152/AJPREGU.2000.279.1.R9.

[189] J. M. Viets-Upchurch and S. S. Bourenane, “Spinal Cord Compression,” *Oncol. Emerg. Med. Princ. Pract. Second Ed.*, pp. 237–245, Feb. 2023, doi: 10.1007/978-3-030-67123-5_18.

[190] M. Oshima, H. Matsuzaki, Y. Tokuhashi, and A. Okawa, “Evaluation of Biomechanical and Histological Features of Vertebrae Following Vertebroplasty Using Hydroxyapatite Blocks,” *Orthopedics*, vol. 33, no. 2, pp. 89–93, Feb. 2010, doi: 10.3928/01477447-20100104-15.

[191] M. Soubeyrand, E. Laemmel, C. Court, A. Dubory, E. Vicaut, and J. Duranteau, “Rat model of spinal cord injury preserving dura mater integrity and allowing measurements of cerebrospinal fluid pressure and spinal cord blood flow.,” *Eur. Spine J.*, vol. 22, no. 8, pp. 1810–9, Aug. 2013, doi: 10.1007/s00586-013-2744-2.

[192] K. Takahashi, H. Ozawa, N. Sakamoto, Y. Minegishi, M. Sato, and E. Itoi, “Influence of intramedullary stress on cervical spondylotic myelopathy,” *Spinal Cord*, vol. 51, pp. 761–764, 2013, doi: 10.1038/sc.2013.94.

[193] K. G. Lyras and J. Lee, “Haemodynamic analysis using multiphase flow dynamics in tubular lesions,” *Comput. Methods Programs Biomed.*, vol. 220, p. 106780, Jun. 2022, doi: 10.1016/J.CMPB.2022.106780.

[194] E. Syková and C. Nicholson, “Diffusion in Brain Extracellular Space,” *Physiol. Rev.*, vol. 88, no. 4, p. 1277, Oct. 2008, doi: 10.1152/PHYSREV.00027.2007.

[195] S. Sakadžić *et al.*, “Two-photon microscopy measurement of cerebral metabolic rate of oxygen using periarteriolar oxygen concentration gradients,” *Neurophotonics*, vol. 3, no. 4, p. 045005, Oct. 2016, doi: 10.1117/1.NPH.3.4.045005.

[196] N. B. Hamilton, D. Attwell, and C. N. Hall, “Pericyte-mediated regulation of capillary diameter: a component of neurovascular coupling in health and disease.,” *Front. Neuroenergetics*, vol. 2, 2010, doi: 10.3389/fnene.2010.00005.

[197] E. A. Winkler, J. D. Sengillo, R. D. Bell, J. Wang, and B. V Zlokovic, “Blood-spinal cord barrier pericyte reductions contribute to increased capillary permeability.,” *J. Cereb. Blood Flow Metab.*, vol. 32, no. 10, pp. 1841–52, Oct. 2012, doi: 10.1038/jcbfm.2012.113.

[198] D. Ferland-McCollough, S. Slater, J. Richard, C. Reni, and G. Mangialardi, “Pericytes, an overlooked player in vascular pathobiology,” *Pharmacol. Ther.*, vol. 171, pp. 30–42, Mar. 2017, doi: 10.1016/J.PHARMTHERA.2016.11.008.

[199] Y. H. Kim, B. Khuyagbaatar, and K. Kim, “Biomechanical effects of spinal cord compression due to ossification of posterior longitudinal ligament and ligamentum flavum: A finite element analysis,” *Med. Eng. Phys.*, vol. 35, no. 9, pp. 1266–1271, Sep. 2013, doi: 10.1016/J.MEDENGPHY.2013.01.006.

[200] E. Onishi, A. Sakamoto, S. Murata, and M. Matsushita, “Risk factors for acute cervical spinal cord injury associated with ossification of the posterior longitudinal ligament,” *Spine (Phila. Pa. 1976).*, vol. 37, no. 8,

pp. 660–666, Apr. 2012, doi: 10.1097/BRS.0B013E31822DA1D5.

[201] B. C. V Campbell *et al.*, “Endovascular Therapy for Ischemic Stroke with Perfusion-Imaging Selection A BS TR AC T,” *n engl j med*, vol. 11, pp. 1009–1027, 2015, doi: 10.1056/NEJMoa1414792.

[202] Y. Kato *et al.*, “Biomechanical study of the effect of degree of static compression of the spinal cord in ossification of the posterior longitudinal ligament: Laboratory investigation,” *J. Neurosurg. Spine*, vol. 12, no. 3, pp. 301–305, Mar. 2010, doi: 10.3171/2009.9.SPINE09314.

[203] H. Yoon, N. won Park, Y. M. Ha, J. Kim, W. J. Moon, and K. Eom, “Diffusion tensor imaging of white and grey matter within the spinal cord of normal Beagle dogs: Sub-regional differences of the various diffusion parameters,” *Vet. J.*, vol. 215, pp. 110–117, Sep. 2016, doi: 10.1016/J.TVJL.2016.03.018.

[204] D. C. Baptiste and M. G. Fehlings, “Pathophysiology of cervical myelopathy,” *Spine J.*, vol. 6, no. 6, pp. S190–S197, Nov. 2006, doi: 10.1016/J.SPINEE.2006.04.024.

[205] R. Kurokawa, H. Murata, M. Ogino, K. Ueki, and P. Kim, “Altered Blood Flow Distribution in the Rat Spinal Cord under Chronic Compression,” *Spine (Phila. Pa. 1976).*, vol. 36, no. 13, pp. 1006–1009, Jun. 2011, doi: 10.1097/BRS.0b013e3181eaf33d.

[206] M. Marsala and T. L. Yaksh, “Transient spinal ischemia in the rat: Characterization of behavioral and histopathological consequences as a function of the duration of aortic occlusion,” *J. Cereb. Blood Flow Metab.*, vol. 14, no. 3, pp. 526–535, 1994, doi: 10.1038/jcbfm.1994.65.

[207] J. Tu, J. Vargas Castillo, A. Das, A. D. Diwan, V. Castillo, and A. Degenerative, “Clinical Medicine Degenerative Cervical Myelopathy: Insights into Its Pathobiology and Molecular Mechanisms,” *J. Clin. Med*, p. 10, 2021, doi: 10.3390/jcm10061214.

[208] P. W. New, R. A. Cripps, and B. Bonne Lee, “Global maps of non-traumatic spinal cord injury epidemiology: Towards a living data repository,” *Spinal Cord*, vol. 52, no. 2. Nature Publishing Group, pp. 97–109, Jan. 15, 2014, doi: 10.1038/sc.2012.165.

[209] I. Vlajić, “Microangiographic observations of morphological vessel changes after experimental spinal cord trauma.,” *Adv. Neurol.*, vol. 20, pp. 451–460, Jan. 1978, Accessed: Dec. 29, 2022. [Online]. Available: https://europepmc.org/article/med/676909.

[210] A. Guha, C. H. Tator, and J. Rochon, “Spinal cord blood flow and systemic blood pressure after experimental spinal cord injury in rats.,” *Stroke*, vol. 20, no. 3, pp. 372–7, Mar. 1989, doi: 10.1161/01.STR.20.3.372.

[211] N. A. Andreollo, E. F. dos Santos, M. R. Araújo, and L. R. Lopes, “Rat’s age versus human’s age: what is the relationship?,” *Arq. Bras.*

Cir. Dig., vol. 25, no. 1, pp. 49–51, 2012, doi: 10.1590/S0102-67202012000100011.

[212] J. Kjell and L. Olson, “Rat models of spinal cord injury: From pathology to potential therapies,” *DMM Dis. Model. Mech.*, vol. 9, no. 10, pp. 1125–1137, Oct. 2016, doi: 10.1242/DMM.025833.

[213] P. Tang *et al.*, “Establishment of a rat model of chronic thoracolumbar cord compression with a flat plastic screw,” vol. 11, no. 6, 2016, doi: 10.4103/1673-5374.184496.

[214] X. Cheng, H. Long, W. Chen, J. Xu, Y. Huang, and F. Li, “Three-dimensional alteration of cervical anterior spinal artery and anterior radicular artery in rat model of chronic spinal cord compression by micro-CT,” *Neurosci. Lett.*, vol. 606, pp. 106–112, Oct. 2015, doi: 10.1016/J.NEULET.2015.08.050.

[215] D. M. Basso, M. S. Beattie, and J. C. Bresnahan, “A Sensitive and Reliable Locomotor Rating Scale for Open Field Testing in Rats,” *J. Neurotrauma*, vol. 12, no. 1, pp. 1–21, Feb. 1995, doi: 10.1089/neu.1995.12.1.

Appendix A

Functional outcome scoring methodology

In vivo studies use the Beattie, Brasso and Bresnahan (BBB) scale to determine functional outcomes [215]. The scoring system is as below (Table 23).

Table 23: Brasso, Beattie and Bresnahan scoring used to assess the severity of neural damage *in vivo*.

	Beattie, Brasso, Bresnahan Scale
0	No observable hindlimb (HL) movement
1	Slight movement of one or two joints, usually thehip and/or knee
2	Extensive movement of one joint or extensive movement of one joint and slight movement of one other joint
3	Extensive movement of two joints
4	Slight movement of all three joints of the HL
5	Slight movement of two joints and extensive movement of the third
6	Extensive movement of two joints and slight movement of the third
7	Extensive movement of all three joints of the HL
8	Sweeping with no weight support or plantar placement of the paw with no weight support
9	Plantar placement of the paw with weight support in stance only (i.e., when stationary) or occasional, frequent, or consistent weight supported dorsal stepping and no plantar stepping
10	Occasional weight supported plantar steps, no forelimb (FL)-HL coordination
11	Frequent to consistent weight supported plantar steps and no FL-HL coordination
12	Frequent to consistent weight supported plantar steps and occasional FL-HL coordination
13	Frequent to consistent weight supported plantar steps and frequent FL-HL coordination
14	Consistent weight supported plantar steps, consistent FL-HL coordination and predominant paw position during locomotion is rotated (internally or externally) when it makes initial contact with the

	surface as well as just before it is lifted off at the end of stance or frequent plantar stepping, consistent FL-HL coordination and occasional dorsal stepping
15	Consistent plantar stepping and consistent FL-HL coordination and no toe clearance or occasional toe clearance during forward limb advancement, predominant paw position is parallel to the body at initial contact
16	Consistent plantar stepping and consistent FL-HL coordination during gait and toe clearance occurs frequently during forward limb advancement, predominant paw position is parallel at initial contact and rotated at lift off
17	Consistent plantar stepping and consistent FL-HL coordination during gait, and toe clearance occurs frequently during forward limb advancement, predominant paw position is parallel at initial contact and lift off
18	Consistent plantar stepping and consistent FL-HL coordination during gait, and toe clearance occurs consistently during forward limb advancement, predominant paw position is parallel at initial contact and lift off
19	Consistent plantar stepping and consistent FL-HL coordination during gait, and toe clearance occurs frequently during forward limb advancement, predominant paw position is parallel at initial contact and lift off and tail is down all or part of the time
20	Consistent plantar stepping and consistent coordinated gait, consistent toe clearance, predominant paw position is parallel at initial contact and lift off, tail consistently up and trunk instability
21	Consistent plantar stepping and coordinated gait, consistent toe clearance, predominant paw position is parallel throughout stance, consistent trunk stability, tail consistently up